MDoF Representation for In-Plane Behaviour of URM Buildings

Non-Linear Time History Analysis

G. Milan

Technische Universiteit Delft

TU Delft

ARUP

MDoF Representation for In-plane Behaviour of URM Buildings

Non-Linear Time History Analysis

by

G. Milan

to obtain the degree of Master of Science
at the Delft University of Technology,
to be defended publicly on Thursday December 21, 2017 at 3:45 PM.

Student number:	4521757	
Project duration:	March 1, 2017 – December 21, 2017	
Thesis committee:	Prof. dr. A. V. Metrikine,	TU Delft, chairman
	Dr. ir. M. A. N. Hendriks,	TU Delft
	Dr. ir. A. Tsouvalas,	TU Delft
	Ir. R. de Vries,	Arup

ARUP

TU Delft

Abstract

In the Groningen province, situated in the northern part of the Netherlands, a large natural gas field was discovered in 1959 and in 1964 the gas extraction started. Due to the gas extraction in the Groningen area, undesired induced earthquakes are generated. The strongest earthquake registered to date was in 2012, 3.6 of the Richter scale. Not being designed and constructed to sustain seismic loading, masonry buildings in the area show higher vulnerability than other more recent structures. In 2013 extensive research on the seismic risk has been initiated in order to assess structure and infrastructure vulnerability to seismic events. Smeared plasticity shell element models have shown to achieve very accurate results in blind predictions of full-scale laboratory tests. However, they are computationally very demanding and hence not suitable for parametric studies and fragility curves development. Alternatively, a computationally efficient lumped plasticity model is proposed, meant to be representative of the in-plane shear and rocking behaviour of URM wall piers. The macro-element model is calibrated with quasi-static tests performed in laboratories at TU Delft and Eucentre. In addition, smeared plasticity numerical simulations are used for the calibration of the energy-based phenomenological parameter in the flag-shaped rule for rocking behaviour. A new hysteretic rule has been developed for modelling the flange effect that characterises slender piers of the Groningen URM buildings. It provides the abstraction for a one-dimensional rate-independent flag-shaped hysteresis with asymmetric backbone. Non-linear time history analyses are performed to assess the response of wall components and to validate the approach against the smeared-plasticity model. Comparable results are achieved in terms of collapse-mechanism prediction, base shear forces, maximum drifts and energy dissipation. Finally, the macro-element is assembled in an equivalent-frame model which represents a prototype house tested quasi-statically at TU Delft. The blind prediction displacement-controlled test shows a 20% capacity overestimation from the lumped plasticity model, proving the necessity of parametric studies for the capacity estimation improvements. NLTH analyses lead to comparable results between the two approaches, in terms of failure mechanism prediction and hysteretic behaviour. The analyses performed with the proposed approach turned out to be faster by two orders of magnitude compared to the shell element models.

Acknowledgements

In this journey, I have met a few people whose contribution and support has been essential.

I would like to express special thanks to Andrei Metrikine, Max Hendriks and Apostolos Tsouvalas for their expert guidance, the insightful comments and the encouragement of critical thinking.

I would like to dedicate my sincere appreciation to Damian Grant and Rein de Vries, for their support and expertise. Their intellectual stimulation towards curiosity research has been vital for the development of this work. I cannot forget the contribution of my Arup colleagues, and the fruitful discussions inside and outside the office.

I would like to thank my friends for their continuous support and thoughtful advices along the journey.

Most of all, special gratitude goes to my family whose unconditional encouragement made this journey possible.

G. Milan
Amsterdam, December 2017

Contents

Nomenclature

Acronyms

I_A	Arias intesity
I_H	Housner spectral intesity
AN	Accelerated-Newton of Krylov-Newton integration method
CaSi	Calcium Silicate material
DoF	degrees-of-freedom
EQ	Earthquake record
GM	Ground motion
M	Caughey or Modal damping model
MDoF	Multi-degree-of-freedom
MN	Modified-Newton integration method
MPP	Massively parallel processing
NLTH	Non-linear time history
NR	Newtow-Raphson integration method
PGA	Peak ground acceleration
PSV	Pseudo-velocity spectrum
RI	Initial-stiffness Rayleigh damping model
RT	Tangent-stiffness Rayleigh damping model
SA	Spectral acceleration
SDoF	Single-degree-of-freedom
URM	Unreinforced masonry

Greek Letters

α	Stiffness proportional damping coefficient, boundary condition factor for wall pier in rocking and toe-crushing modes
β	Mass proportional damping coefficient, Ratio of Forward to Reverse Activation Moment for flag shape model
Δt_c	Critical time-step for explicit integration
μ_c	Coefficient of friction of masonry relative to the mortar joint
ν	Poisson's ratio
ρ	Volumetric mass density
σ	Vertical compression sress caused by gravity loads

ζ	Damping ratio
$\zeta_{eq,h}$	Equivalent hysteretic damping ratio
$\zeta_{eq,v}$	Equivalent viscous damping ratio

Roman Letters

$\ddot{u}_g$	Earthquake acceleration
A_v	Shear area
c	Damping coefficient, speed of sound through the elastic medium
E_m	Masonry elastic modulus
f_c	Masonry compressive strength
f_s	Resisting forces
f_t	Tensile strenght of masonry
f_{v0}	Shear strengh of the masonry under zero compression stress
f_v	Shear strength of the masonry
G_m	Masonry shear modulus
h_{eff}	Effective heigh of the wall pier
I_g	Moment of inertia of the gross section representing un-cracked behaviour
l_c	Critical length for beam and shell element
P_D	Superimposed load at the top of the wall pier
P_w	Self weight of the wall pier
V_r	Rocking pier capacity
V_{bjs}	Bed-joint sliding pier capacity
V_{dt}	Diagonal cracking pier capacity
V_{tc}	Toe-crushing pier capacity
g	Standard acceleration of free fall

Introduction

In the Groningen province, situated in the northern part of the Netherlands, a large natural gas field was discovered in 1959 and in 1964 the gas extraction started. Due to the gas extraction in the Groningen area, undesired induced earthquakes are generated. The strongest earthquake registered to date took place in 2012, with an estimated magnitude of 3.6 in the Richter scale.

Figure 1: Groningen region location plan [1]

Most of the building stock (89 %) in the Groningen area (Figure 1) consists of unreinforced masonry (URM) buildings [42]. Masonry has been used for centuries as construction material, and it has contributed to some of the most iconic structures. With the exception of monumental buildings, which have sometimes been designed on the basis of experiments and the simple theory of structures, masonry buildings have been built on the basis of tradition and experience. In addition, not being designed to sustain seismic loading, the structural vulnerability of Dutch URM buildings is often relevant.

Motivation of the study

In 2013 extensive research on the seismic risk in the Groningen region has been initiated in order to assess structure and infrastructure vulnerability to seismic events. Smeared plasticity shell element models (Figure 2) have shown to achieve very accurate results in blind predictions of full-scale laboratory tests [24].

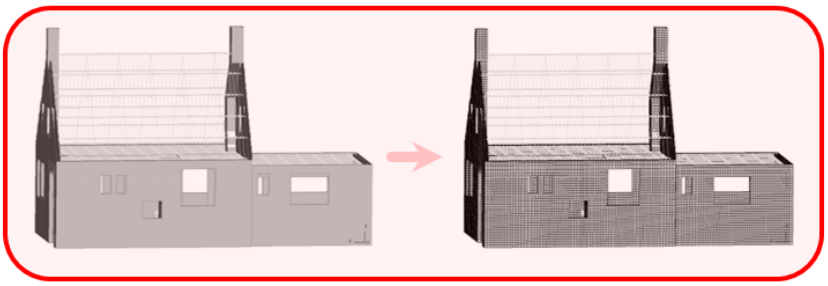

Figure 2: FEM representation of the URM building

However, they turn out to be computationally very demanding and hence not suitable for parametric studies and large-scale risk calculations. The latter are usually carried out through the fragility curves development. It is a statistical tool representing the probability of exceedance of a given structural performance as a function of an engineering demand parameter representing the input seismic hazard (e.g. ground motion due to seismic event). Given the intrinsic randomness and unpredictability of seismic events, the calculations need to be performed using thousands of accelerograms, to cover the record-to-record variability.

To meet this objective, in seismic engineering, the actual multi-degree-of-freedom system (structure) is usually represented by a dynamic single-degree-of-freedom (SDoF) system [36]. The standard conversion approach is based on the modal analysis [19] and leads to the definition of an equivalent single-mass system (Figure 3).

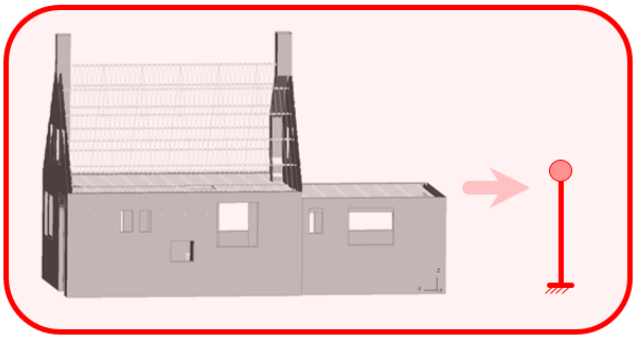

Figure 3: SDoF representation of the URM building

This has the advantage of acting as a reasonably simple and fast method. However, being based on linear response of the structure, the procedure of system identification is not justified in the case of non-linear response, which strongly characterize the dynamic behaviour of URM buildings.

Research objectives

To overcome the limitations described above, it is preferable to explicitly account for the non-linear behaviour of URM structures, and hence, to develop a multi-degree-of-freedom (MDoF) model (e.g. Figure 4). The model is calibrated to capture the in-plane dynamic behaviour of the pier components, core of the structural system of URM buildings.

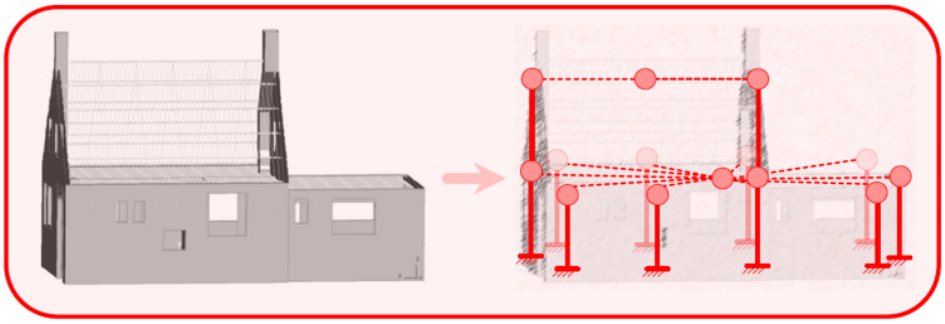

Figure 4: MDoF representation of the URM building

Therefore, in a lumped plasticity fashion, the degrees-of-freedom (DoF) are related to the shear and rocking failure modes of URM walls. In this framework, one is able to assess the global response of the building, in terms of drift, base shear force and energy dissipation, when subjected to an earthquake excitation. This approach leads to a computationally efficient tool, suitable for the aforementioned large-scale risk calculations of the Groningen building stock. Given its simplicity, this approach allows to account also for the variability of the superstructure (and not only of the ground motion). Probabilistic calculations may be carried out in order to evaluate the sensitivity of the dynamic system to varying masonry structural properties.

Strategy

The literature review acts as the starting point for the identification of the most suitable approach to achieve the research objectives. Current knowledge in terms of theoretical and experimental work suggests that at the ultimate limit state, the URM structure is broken down into pier and spandrels elements. Therefore, a macro-element model for the in-plane behaviour of pier elements is formulated, based on analytical formulation, as well as on laboratory tests results and smeared plasticity numerical simulations. Consequently, the approach is validated performing sets of non-linear time history (NLTH) analyses on two wall component typologies, namely slender and squat piers, varying frequency range, duration and intensity of the input. Finally, the macro-element is assembled into an equivalent-frame model representing a prototype house tested quasi-statically in the Macrolab of Delft University of Technology.

Dissertation outline

- The chapter **Induced Seismicity and Dynamic Performance of URM Buildings** outlines a general overview of the Groningen seismicity and the behaviour of URM buildings under the seismic action.

- The chapter **Seismic Resistance Assessment of URM Wall Piers** deals with the analytical calculation procedures to compute the in-plane capacity of structural walls, identifying the typical failure modes that characterize them.

- The chapter **Reduction of degrees-of-freedom** describes the approach for the reduction of the degrees-of-freedom, from the full building to the MDoF system. A lumped plasticity approach is presented along with the hysteretic models, based on the behaviours identified in Chapter 2.

- The chapter **Non-Linear Time History Analysis** deals with the non-linear time history analysis procedure, with particular focus on the damping model for seismic analysis and energy-based calculations.

- The chapter **In-plane Dynamic Test on URM Wall Piers** includes the point cloud NLTH analysis for the in-plane behaviour of rocking and shear driven pier components.

- The chapter **Benchmark Building** describes the assembly of the macro-element in an equivalent frame model representing a prototype house tested quasi-statically in the laboratory.

- The chapter **Conclusions and Recommendations** includes a critical reflection on the proposed methodology and on the numerical simulation results. Further improvements of the model are outlined.

Limitation of the research

The current work has been developed taking into account the following limitations and assumptions:

- Foundation flexibility and non-linear soil response are not considered in the analyses, as well as the interaction between soil and structure. However, the ground motions used in the analyses take into account the Groningen-specific site response .
- The presence of spandrels connecting the masonry piers and openings has not been investigated. Often, Dutch residential URM buildings are characterised by shallow spandrels, weak relatively to adjacent piers, hence are less likely to couple multiple piers and transmit overturning to adjacent piers, increasing axial forces in end piers and potentially changing the sequence of actions.
- Effect of failure of connections between diaphragms and walls is it not explicitly modelled in the analyses.
- The out-of-plane failure of walls it is not taken into account. The proposed approach is for the assessment of the in-plane response of URM structures. The contribution of the walls orthogonal to the in-plane direction however is taken into account as an increase of the in-plane strength (i.e. flange effect).
- The effect of the vertical component of the ground motions is not taken into account in the analyses. However, buildings are primarily designed to carry the vertical gravity loads. Hence, they are likely less vulnerable in the vertical direction (additional information are included in Appendix C).
- The proposed approach is validated against LS-DYNA masonry material model, which has been developed on the basis of benchmark tests carried out to date [24]. Calibration of structural analysis models against experimental behaviour has been limited by the extent to which experimental tests have historically been run to full collapse of specimens and buildings.

1

Induced Seismicity and Dynamic Performance of URM Buildings

In the present chapter, an overview of the induced seismicity of the Groningen region is provided, from the causes of the events to the recent seismicity timeline. Furthermore, a brief description of the dynamic behaviour of URM buildings is presented, highlighting the motivations for the adoption of a lumped plasticity approach.

1.1. Induced seismicity in the Groningen gas field

The Groningen gas field, in the North-East part of the Netherlands, is the largest gas field in western Europe, with the presence of 3000 billion m^3 of gas. The gas field was discovered in 1959 and the extraction started in 1963. Since 1991, seismicity in the Groningen region has been recorded above the gas fields and it is considered to be directly related to the gas extraction. The magnitude of these earthquakes ranged between 0.8 and 3.6 of the Richter scale, with the largest earthquake local magnitude of 3,6 registered on the 16^{th} of August 2012 [25]. Even though the magnitude of the event was fairly limited when compared to other tectonic events, an intensity equal to IV of the Mercalli scale was observed in the region; mostly related to the shallow depth of the event and the soft soil in that area [53]. Thus, damages were caused to the houses in that area. This has led to some studies in which the links between the geology of the field, the reservoir dynamics and the geo-mechanics have been analysed [53], [54].

1.1.1. Causes of the earthquakes

The Groningen subsidence has both shallow and deep causes. Shallow subsidence is caused by compaction of clay, oxidation of shallow peat, and artificially modified groundwater levels. Deep subsidence results from reservoir compaction related to gas production (Figure 1.2). Due to gas depletion, the pressure reduction causes compaction of the reservoir, thus stress variations generate seismicity. The compaction is visible at the surface as subsidence. Close to existing faults, compaction induces shear stress on the fault because of the initial inability of the faults to move. Depending on the sliding friction of the fault and magnitude of the stress change, the faults can slip, thus cause a seismic event [54].

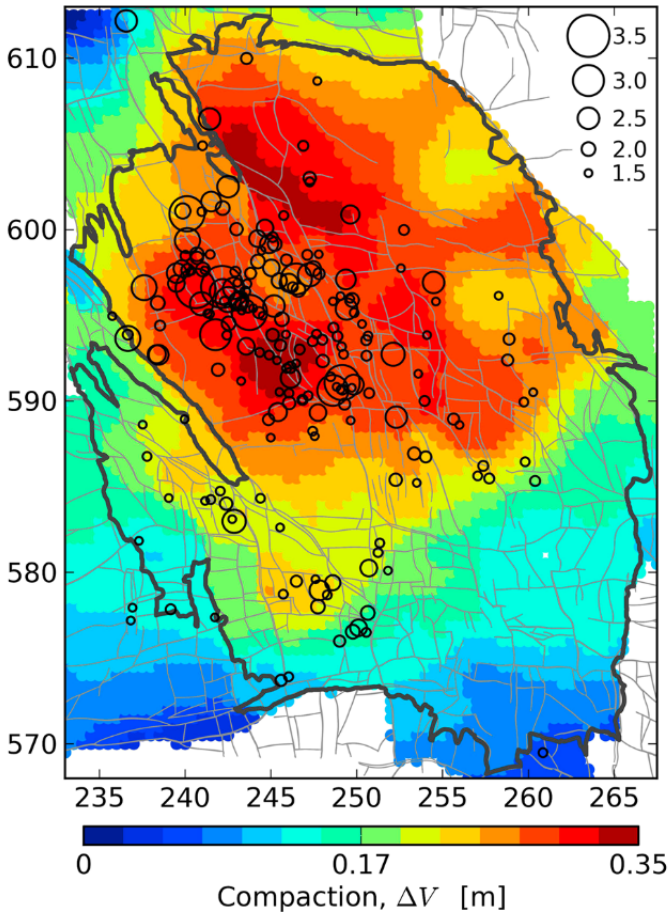

Figure 1.1: Earthquake epicenters for $M_L \geq 1.5$ in relation to the model of reservoir compaction from 1960 to 2012 [9]

The empirical relation proposed by [9] directly links the cumulative reservoir compaction to seismicity, which is indeed highest in the centre of the gas field (Figure 1.1).

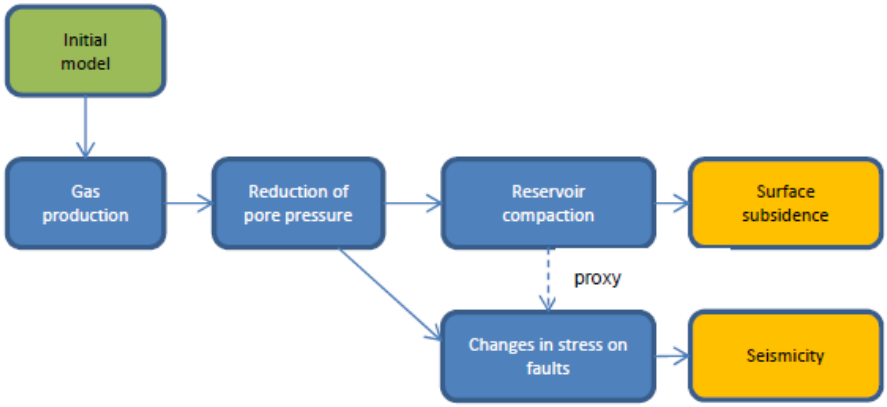

Figure 1.2: Scheme of the relation between gas production and seismicity [54]

1.1.2. Seismicity history

Before any gas extraction, the north of the Netherlands had no record of seismicity, thus the Groningen region has been historically considered tectonically stable. The first induced seismic event had a magnitude M_L of 2.4 and was recorded at Middelstum in 1991. After that date, seismic events have increased over time (Figure 1.3) both in frequency and intensity [10]. Most of the events before 2003 have been of small magnitude ($M_L <= 1.5$). Thereafter an increase of the frequency of larger magnitude events has been observed:

- 2003: first event of magnitude M_L larger than 3.0;
- 2006: an event of magnitude M_L of 3.5 occurred;
- 2012: largest event recorded, with a magnitude M_L of 3.6, near the village of Huizinge (see Appendix C).

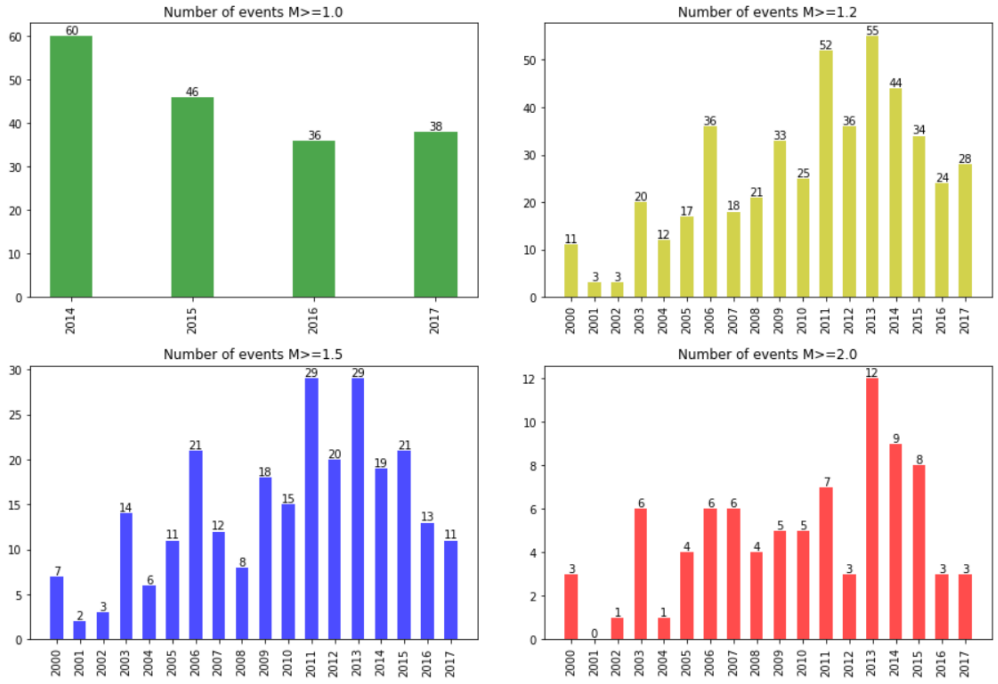

Figure 1.3: Number of earthquakes per year for 4 magnitude classes registered in the Groningen field from 2000 to 2017 [43]

Induced seismicity in the Groningen field seems to be non-stationary and increasing with time [41] and even thought not yet statistically significant, the observations suggest a close link among gas production, compaction and seismicity.

1.2. Dynamic performance of URM buildings

Masonry has been used as a hand craft material of old. With the exception of monumental buildings, which have sometimes been designed on the basis of experiments and the simple theory of structures, masonry buildings have been built on the basis of tradition and experience. Masonry buildings, designed and constructed according to requirements of modern seismic codes, behave adequately. Cases of collapse are rare and were limited to buildings where the requirements of codes (especially those related to the quality of constructions) were only partly met [55].

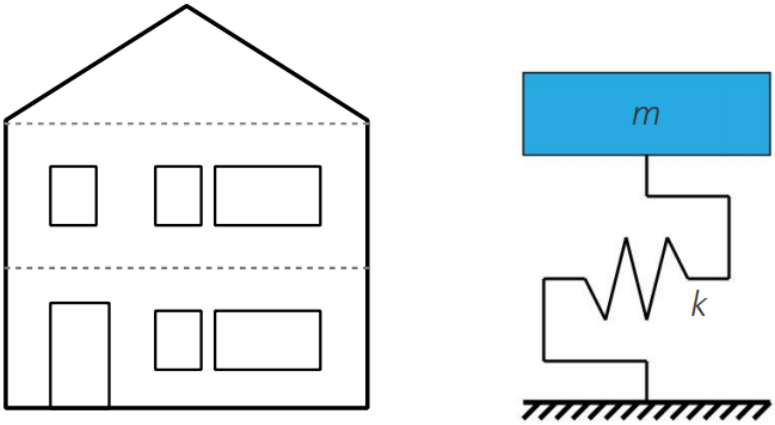

Figure 1.4: SDoF representation of the URM building

During an earthquake event, the ground acceleration $\ddot{u}_g$ generates inertia forces, represented by the right-hand-side of the equation of motion (Equation 1.1), in the building components.

$$m\ddot{u}_{rel} + c\dot{u}_{rel} + ku_{rel} = -m\ddot{u}_g \tag{1.1}$$

where $\ddot{u}_{rel}$, $\ddot{u}_{rel}$ and $\ddot{u}_{rel}$ are respectively acceleration, velocity and displacement of the SDoF (representation of the structural system) relative to the ground. The inertia forces $-m\ddot{u}_g$ must find a path to the ground by transferral to other components via connections. The load path invariably determines the critical components of a structure as insufficient strength in any component of a building results in an unsatisfactory seismic response. For existing buildings, the load path is commonly dictated by the connections between walls and diaphragms, as seen in historical URM buildings where the connection between the out-of-plane loaded walls and the diaphragms are often inadequate such that the out-of-plane loaded wall is the critical component [45].

The load path varies significantly when adequate wall to diaphragm connections are present. When subjected to seismic ground motion, the foundation of a URM building transmits seismic energy to the stiffest components of the URM building, being the in-plane loaded walls. In general, in-plane loaded walls in a URM structure are considered as primary lateral-load resisting components (i.e. in-plane wall mostly contributes to the stiffness k in Figure 1.1), while the main role of the out-of plane loaded walls is their vertical load capacity, and in most cases, their additional lateral shear resistance is considered negligible.

Although the structural typology of masonry buildings varies in different regions, their damage resulting from earthquakes can be classified in an uniform way. The following typical types of damage can be identified by the analysis of the observed earthquake damage patter (Figure 1.5):

- Cracks between walls and floors;
- Cracks at the corners and at wall intersections;
- Out-of-plane collapse of perimetral walls;
- Cracks in spandrel beams and/or perimetral walls;
- Diagonal cracks in structural walls;
- Partial disintegration or collapse of structural walls;
- Partial or complete collapse of the building.

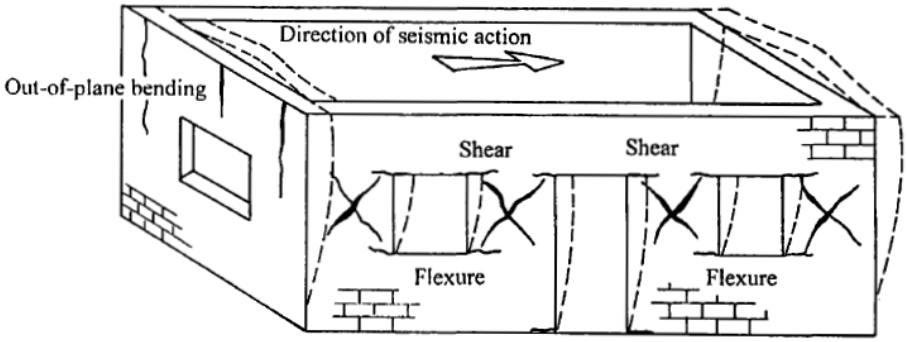

Figure 1.5: Deformation of the building and typical damage to structural walls [55]

The equivalent frame approach [49] [33] referenced in Chapter 3, in fact, lies behind such a damage pattern, which suggests that, at the ultimate limit state, the structural walls are broken down into pier elements and spandrels between openings (Figure 1.6). In addition, the damage pattern indicates that the inelastic deformations are usually lumped at certain locations, while the rest of the structure remains undeformed. For this reason, the concentrated plasticity approach has been chosen in the present work.

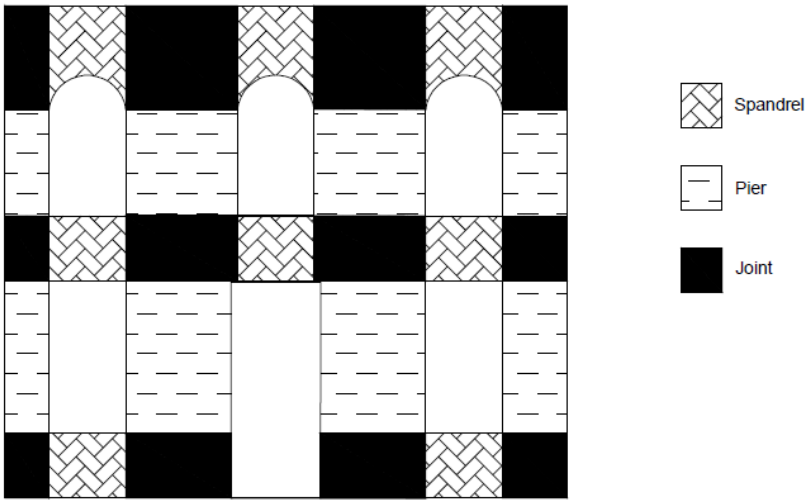

Figure 1.6: Geometry definition for perforated walls [32]

2

Seismic Resistance Assessment of URM Wall Piers

As introduced in the previous chapter, the main lateral resisting system of an URM building relies on the in-plane capacity of the masonry walls; these determine the global dynamic structural behaviour during an earthquake event. In this chapter, an overview of the simplified models for this behaviours is presented, along with the description of the analytical formulation for the mechanics of the failure modes of pier and spandrel elements. Therefore, the literature provides the basis for the calibration of the inelastic springs, basis of the lumped plasticity MDoF approach. As an example, the dynamic representation of a structural wall subjected to lateral loading is presented in the Figure 2.1. The elasto-plastic constitutive law is representative of the failure modes of wall components.

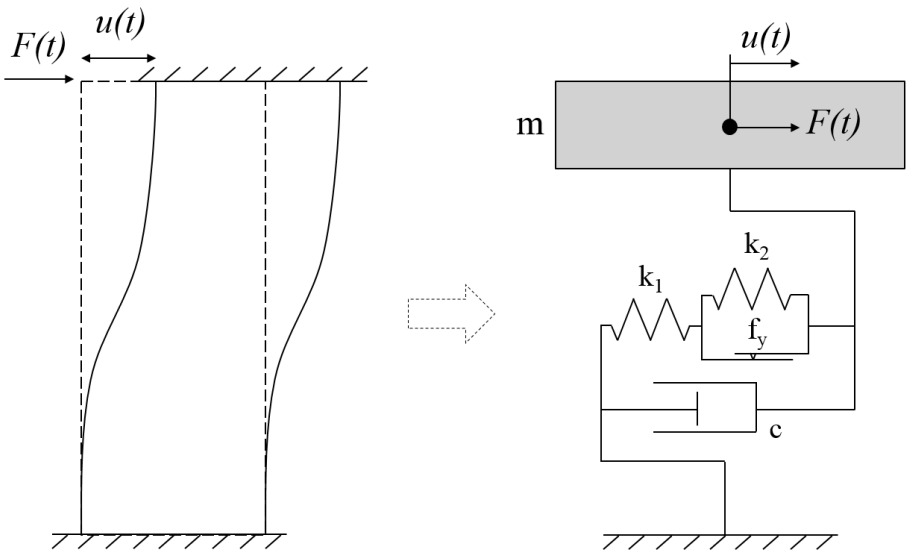

Figure 2.1: Example of the system representation

2.1. In-plane mechanisms

Observations of seismic damage to perforated unreinforced masonry walls, as well as laboratory experimental tests, have shown that masonry piers subjected to in-plane loading fail in one of two responses (shear or flexure), with which different failure modes and crack patterns are associated [32]. These mechanisms are primarily dependent on the wall geometry, their boundary conditions, the magnitude of vertical load, and finally on the characteristics of the brick, mortar and brick-mortar interface.

Regarding the flexural response, one can identify both the rocking and toe-crushing failure modes, respectively Figure 2.2 a and b. If the applied vertical load is low compared with the brick compressive strength, tensile cracks develops at the pier corners along the bed-joints, and the element starts rotating around the compressed toe. For the rocking, the ultimate failure consists in the complete overturning of the element, while for the toe-crushing, a compression failure at the corner bricks occur.

The shear response can be related to the bed-joint sliding and the diagonal cracking, respectively presented in Figure 2.2 (c) and (d). A shear sliding mode occurs when sliding planes form due to the formation of tensile horizontal cracks in the bed-joints, which eliminate any shear strength due to cohesion. Diagonal cracking failure is characterised by diagonal cracks, which can either take a stair stepped route following the path of bed- and head-joints, or can take a straight diagonal line through the brick units.

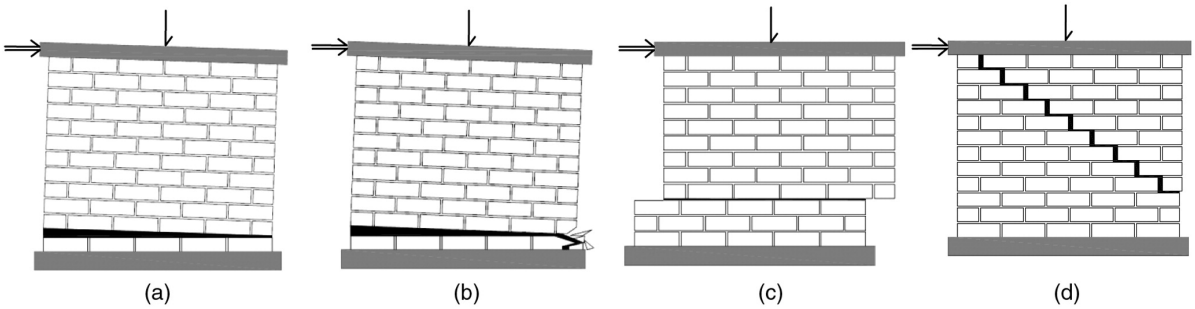

Figure 2.2: In-plane failure modes [47]

Rocking, bed-joint sliding and diagonal cracking with stair stepped path via bed- and head-joints are regarded as deformation-controlled or ductile mechanisms, while toe-crushing and diagonal cracking through the bricks as force-controlled or brittle mechanisms. In general, it is recognised that rocking prevails in slender piers, whereas bed-joint sliding tends to occur only in very squat piers [34]. Diagonal cracking governs over rocking in moderately slender piers where the axial load level is high [56].

2.1.1. Static stiffness estimation

Before introducing the description of the analytical mechanics formulation of each failure mode, the elastic stiffness estimation for URM walls is discussed. Laboratory tests of solid shear walls [3] have shown that the behaviour at low force levels can be depicted using conventional principles of mechanics for homogeneous materials. In such cases, the lateral in-plane stiffness of a solid cantilevered shear wall, k , can be calculated using:

$$k = \frac{1}{\frac{h_{eff}^3}{3E_m I_g} + \frac{h_{eff}}{A_v G_m}} \tag{2.1}$$

where h_{eff} = wall height (see Figure 2.3);
A_v = shear area;
I_g = moment of inertia of the gross section representing un-cracked behaviour;
E_m = masonry elastic modulus;
G_m = masonry shear modulus.

Analogously, the lateral in-plane stiffness of a wall pier between openings with full restraint against rotation at its top and bottom (i.e. fix-fix condition) can be calculated using:

$$k = \frac{1}{\frac{h_{eff}^3}{12E_m I_g} + \frac{h_{eff}}{A_v G_m}} \tag{2.2}$$

One should be aware that that a completely fixed condition is usually not present in actual buildings. This aspect is further discuss in Section 2.4. It is import to notice, that the estimation of the correct initial stiffness of the walls is very important for the Groningen earthquakes. The short duration of events is such that the structure oscillates only few times inelastically in the strong motion part and does not have the cycle content to develop the conspicuous stiffness degradation that characterises tectonic earthquakes.

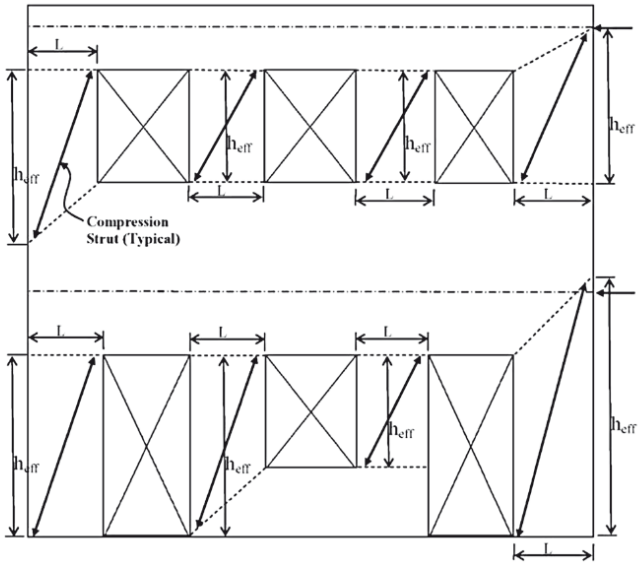

Figure 2.3: URM pier effective heights based on developing diagonal compression struts [39]

2.1.2. Rocking

As mentioned above, in the rocking failure mode, the element starts rotating around the compressed toe due to the gap opening at the bed-joint. Therefore, the strength of such a mechanism is derived from rotational equilibrium considerations (Figure 2.5). According to [4], the lateral strength V_r of wall pier components governed by rocking behaviour shall be calculated as follows:

$$V_r = 0.9(\alpha P_D + 0.5 P_W)\frac{L}{h_{eff}} \tag{2.3}$$

where h_{eff} = wall height;
L = length of wall pier;
P_D = superimposed dead load at the top of the wall pier under consideration;
P_w = self weight of the wall pier;
α = factor equal to 0.5 for fixed-free cantilever wall, or equal to 1.0 for fixed-fixed wall pier;
0.9 = factor to account for the reduced level arm due to deformability at corner location.

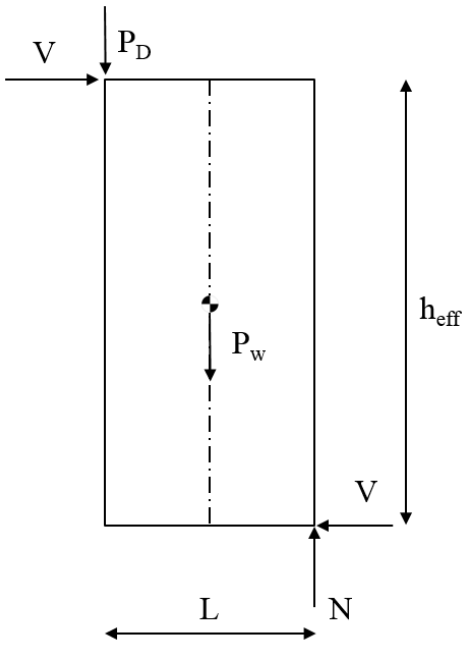

Figure 2.4: Rocking pier variable definitions

During cyclic loading, in a displacement control test, the component starts deforming elastically. Once the lateral actions overcome the vertical forces, the wall starts to tilt around its toes, leading to the so-called gap opening. The gap opening at the wall base limits the seismic force demand by exhibiting a geometric non-linearity similarly to the material non-linearity in conventional reinforced concrete shear walls due to plastic hinge formation. During the unloading, the gap closes until the wall starts moving elastically again in the other direction. Therefore, theoretically, the rocking behaviour can be modelled with the non-linear elastic behaviour presented in the figure below.

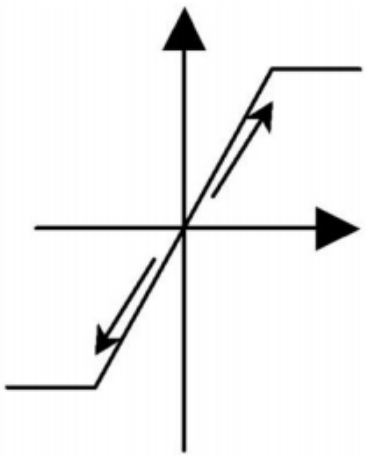

Figure 2.5: Rocking behaviour

2.1.3. Toe-Crushing

The toe-crushing response consists in a rotation around the compressed toe, which ends up with crushing of the bricks at the corner, due to reaching of compression strength of the material. Analogously to the rocking mode case, the lateral strength of a pier component governed by the toe-crushing failure mode can be calculated from rotational equilibrium consideration (Figure 2.6 on the left). The masonry stress distribution in the compression zone is non-linear and is obtained from its uniaxial stress–strain curve shown in Figure 3.7.

Therefore, the actual stress block is replaced by an equivalent rectangular masonry stress block as shown in Figure 2.6 on the right. The equivalent block has the same area and centroid as the actual stress distribution under flexure. Based on these assumption, the toe-crushing capacity can be expressed as follows:

$$V_{tc} = 0.9(\alpha P_D + 0.5 P_W)\frac{L}{h_{eff}}\left(1 - \frac{\sigma}{0.7 f_c}\right) \tag{2.4}$$

where h_{eff}, L and α are the same as given for Equation 2.3;

σ = axial compression stress caused by gravity loads;

f_c = masonry compressive strength;

P_D = superimposed dead load at the top of he wall pier under consideration;

P_w = self weight of the wall pier;

0.7 = factor to account for the equivalent area of the stress block idealization (Figure 2.6 on the right).

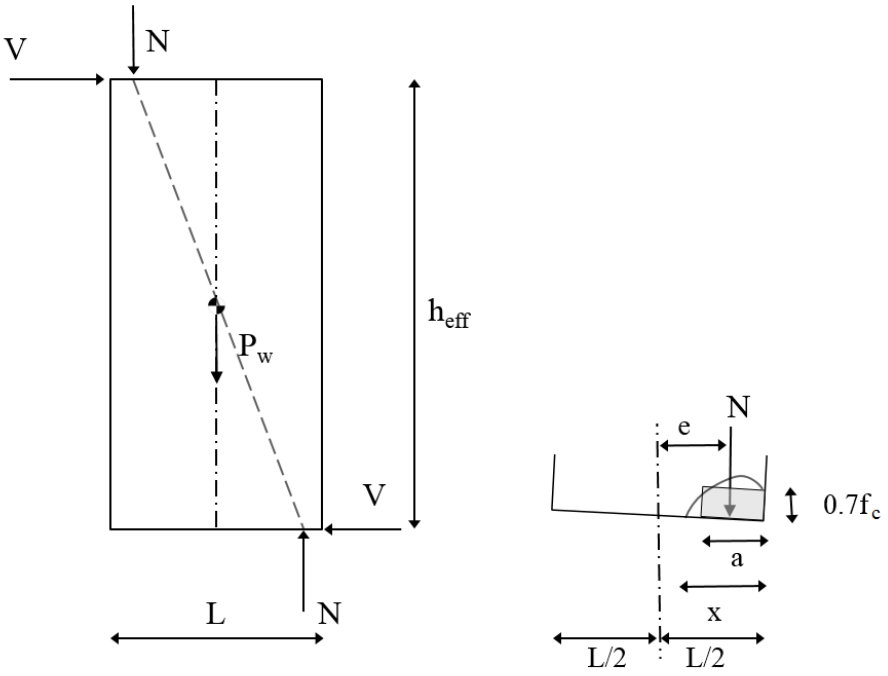

Figure 2.6: Toe-crushing mode variable definitions

Despite being considered separate failure modes, rocking and toe crushing are often intrinsically linked such that they represent a single failure mode. In both cases, they initiate with the tensile cracks along the bed-joints, while the ultimate failure is defined by overturning of the wall and simultaneous crushing of the compressed toe of the wall, respectively.

2.1.4. Bed-Joint Sliding

Bed joint sliding, often referred to as sliding shear, occurs due to the formation of tensile cracks in the bed joints which create potential sliding planes in the pier. In order to physically model the shear failure mechanism, the friction theory is used for the shear strength of the masonry f_v [55]:

$$f_v = f_{v0} + \mu_c \sigma \tag{2.5}$$

where f_{v0} = the shear strength under zero compression stress;
μ_c = shear friction coefficient of masonry relative to the mortar joint;
σ = the compression stress, perpendicular to shear.

The capacity for bed-joint sliding in masonry elements is a function of frictional resistance and bond. The bond component is progressively degraded as cracking occurs until only the frictional components remain. In addition, full-scale test results address the occurrence of flexural cracking at small pier displacements [40], making the bond contribution vanish during the actual sliding. Hence, the contribution to be taken into account for the strength calculation is given by the second part of Equation 2.5, and results in:

$$V_{bjs} = \mu_c P_D \tag{2.6}$$

where P_D = superimposed laod at top of the wall or pier under consideration, and μ_c as definied after Equation 2.5.

During cyclic loading, when the specimen is subjected to a displacement control at its top, it moves laterally elastic up to the yielding point, when the masonry shear strength is reached. Hence, the sliding occurs, and the constant frictional portion of the shear strength regulates the inelastic deformation, with a zero stiffness branch.

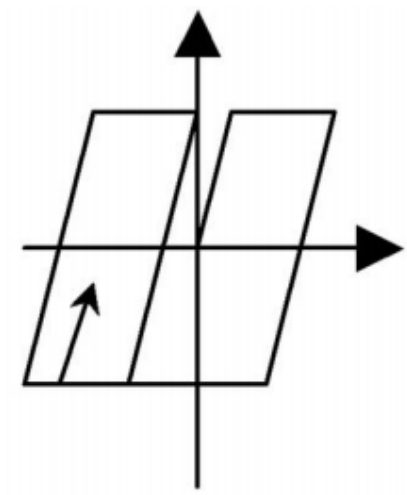

Figure 2.7: Bed-joint sliding behaviour

2.1.5. Diagonal Tension

The derivation of an analytical formulation for the diagonal cracking failure mode relies on the hypothesis that the diagonal cracks are caused by principal tensile stresses due to the stress state under the combination of horizontal and vertical loading [11]. Hence, the principal tensile stress at the point where the two diagonals of the pier intersect, neglecting the horizontal normal stress, is given by:

$$\sigma_n = \sqrt{(1.5\tau)^2 + \left(\frac{\sigma}{2}\right)^2} - \frac{\sigma}{2} \tag{2.7}$$

By setting this expression equals to the tensile strength for the masonry f_t, one is able to come up with the diagonal cracking strength, given by:

$$V_{dt} = \frac{f_t}{1.5} A_n \sqrt{1 + \frac{\sigma}{f_t}} \tag{2.8}$$

It has been proven that the equation is valid from pier aspect ratio $\frac{h}{L}$ larger that 1.5. Corrections to take into account the actual geometry of the pier component has been later introduced [4]:

$$V_{dt} = f_t \beta A_n \sqrt{1 + \frac{\sigma}{f_t}} \tag{2.9}$$

where $\beta = 0.67$ for $\frac{l}{h_{eff}} < 0.67$, $\frac{l}{h_{eff}}$ when $0.67 <= \frac{l}{h_{eff}} <= 1.0$, and 1.0 when $\frac{l}{h_eff} > 1.0$.

Differently from the bed-joint sliding, the through-bricks diagonal cracking entails intensive strength and stiffness degradation when the specimen undergoes repeated loading. The diagonal tension via head- and bed-joints shows instead an hysteretic behaviour similar to the bed-joint sliding [3].

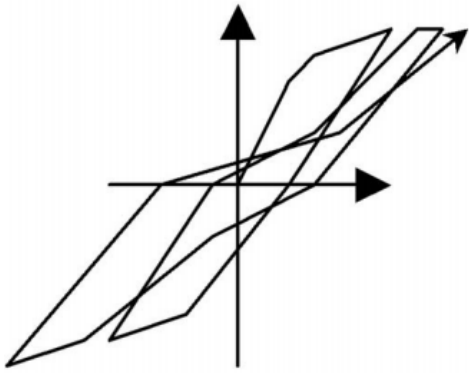

Figure 2.8: Through-brick diagonal tension cracking behaviour

2.2. Displacement capacity

In this section, the displacement capacity for URM walls is discussed. Test results indicate that for URM walls governed by an initial rocking response, drifts of at least 1.5% are sustainable, provided that toe crushing does not control the response at low drifts [35], [40] [3]. Indeed, theoretically being a rigid body motion, the ultimate displacement for such a mechanism is the one corresponding to actual geometrical instability (i.e. the wall is moving with a displacement equal to its length). However, before this, crushing of the masonry at the corner level is likely to occur. Hence, as suggested in [15], the capacity of URM structural wall governed by flexure can be expressed in terms of drift and taken equal to $4/3 \cdot 0.008 \cdot H_0/D$, where D is the in-plane horizontal dimension of the wall (depth), and H_0 is the distance between the section where the flexural capacity is attained and the contra-flexure point.

Regarding URM walls governed by shear, one needs to distinguish the behaviour between diagonal cracking with stair stepped cracks along head-bed-joints, and through-brick diagonal cracking. An ultimate drift equal to 0.53% was found to be extraordinarily uniform for through brick diagonal shear cracking response of URM walls tested in Pavia and Ispra, with a coefficient of variation of 10% on 10 samples with different slenderness ratio and overburden loads [35]. Regarding the cracking via head- and bed- joints, drifts up to 0.75% has been observed in test results. This is because, such a mechanism is regarded as a second form of bed-joint sliding cracking. Regarding pure bed-joint sliding instead, several tests are available out of 1% drift. However, it is preferable to conservatively set the upper-bound to the through brick diagonal tension response limit, since it has been found the diagonal-tension failure mode the most frequent in tests performed on shear dominated walls at EUCentre and TU Delft [3], and it is not straightforward to predict if the inelastic deformation propagates on the mortar only, rather than the bricks. The drift limits adopted for the analyses are summarised in Table 2.1.

Table 2.1: Drift limits for the in-plane actions of URM walls

	Drift limit
Element governed by flexure	$4/3 \cdot 0.008 \cdot H_0/D$
Element governed by shear	0.53%

2.3. Flanged sections

Very often the walls of composite sections in plan, such as "L", "T" and "+" shape sections, can be found in the plan of the building under consideration. Only a limited amount of instructions regarding the modelling of seismic behaviour of flanged section walls can be found in the codes.

Effective flange length According to [13], a limited portion of an intersecting wall can act as a flange to a shear wall, increasing its stiffness and strength. The length of any intersecting wall l_f, which may be considered to act as a flange, is given by the minimum of the following values below (see Figure 2.9):

- $2h_{tot}/10$, where h_{tot} is the overall height of the shear wall;
- Half of the distance between shear walls l_s, when connected by the intersecting walls;
- $6t$, where t is the thickness of the web;
- Half of the storey height h.

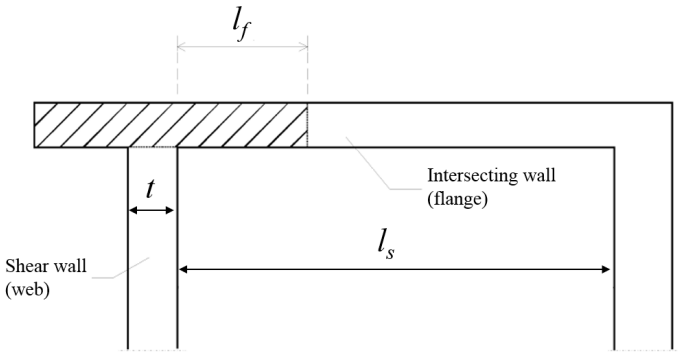

Figure 2.9: Flange widths that can be assumed for shear walls [13]

2.3.1. Stiffness estimation

Regarding the stiffness of flanged walls, the elastic stiffness of the shear walls, including any flanges should be used for the distribution of horizontal forces. As has been found by shaking table tests of URM building prototypes with a predominant shear behaviour, it can be assumed that at ultimate state the wall of composite flanged sections will separate along their vertical joints. This is due to the very different displacement capacity of the out-of-plane components, regards as ductile, and the brittle shear wall. The separated parts of the composite section will resist the seismic loads as individual walls with a simple rectangular cross-section. In the case of slender URM flanged-shaped walls with predominant flexural behaviour, the experiments show that when the flange is in tension, the flexural strength and stiffness are greater that when the flange is in compression [55].

The lateral in-plane stiffness of a wall pier with flanged section between openings with full restraint against rotation at its top and bottom can be calculated using:

$$k = \frac{1}{\frac{h_{eff}^3}{3E_m I_g} + \frac{h_{eff}}{A_v G_m}} \tag{2.10}$$

where h_{eff} = wall height;
A_v = shear area as defined in Figure 2.10;
I_g = moment of inertia of the T-shaped gross section (Figure 2.10);
E_m = masonry elastic modulus;
G_m = masonry shear modulus.

In this framework, the moment of inertia is calculated for the composite section. The shear area is instead calculated by applying the shear coefficient to the rectangular cross section given by area of the web and the flange area where the two walls intersects (see Figure 2.10). This assumption lies behind the fact that the area resisting the shear horizontal seismic force is mostly related to the web, while the contribution of the flange can be neglected.

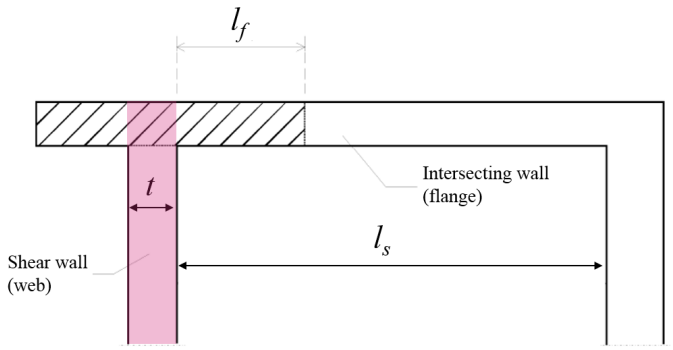

Figure 2.10: Shear area (pink) assumed for the calculation of the in-plane stiffness of flanged sections

Flange participation One is able to estimate the increase of strength given by the flange. In the present framework, a flange is defined as the portion of the out-of-plane wall that participates with the in-plane wall to resist lateral loads. The flanges are classified into three categories:

- Compression flange: the portion of the out-of-lane wall that resists compressive stresses generated by rocking of the adjacent pier;
- Global tension flange: the portion of the out-of-plane wall that is lifted up by global rocking;
- Component tension flange: the portion of the out-of-plane that is lifted up by the local pier rocking, which can occur at both the tension and the compression sides od a building structure.

The tension flanges represent a flange type that is unique to URM structures, and is defined as the portions of out-of-plane walls that are lifted up by the deformation of the in-plane walls, and thus contribute additional weight to the in-plane piers. Hence, component tension flanges are assumed to act primarily as a source of additional weight. They are considered to increase the vertical force in the adjacent pier and not to affect the way overturning or global rocking is resisted. When the in-plane piers are subjected to lateral loads, the tilting of the piers uplift the transverse wall. This increases the bending moment capacity of the active piers by activating the weight of the transverse wall and its axial load. The portion which is assumed to contribute is displayed in Figure 2.11.

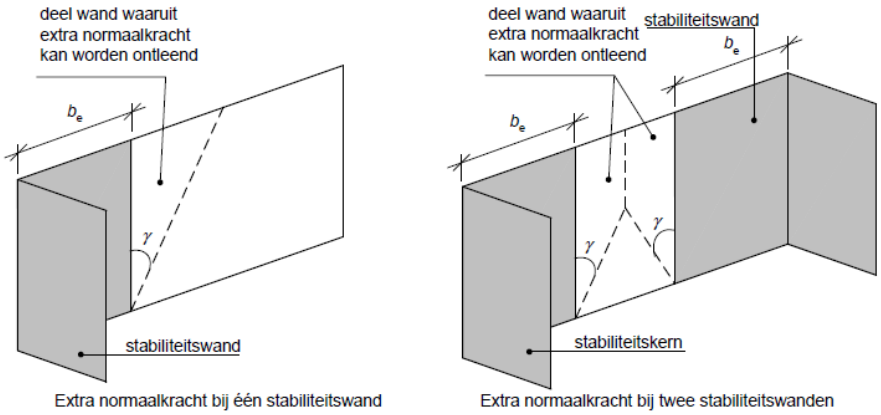

Figure 2.11: Component tension flange [14]

2.3.2. Rocking Strength

It can be seen that in the case of verification for shear, the web (i.e. the part of the wall parallel to seismic action) represents the resisting part of the wall. The contribution of the flange (i.e. the part of the wall orthogonal to seismic motion) can be neglected. However, in case of bending, the contribution of the flange should be taken into account.

The lateral strength of wall pier components (web) an intersecting orthogonal wall (flange) governed by the rocking behaviour, as mentioned above, shall be distinguished in case the component is acting as an active (tension flange) or a passive pier (compression flange). Analogously to the case of rectangular section, the strength can be estimated from rotational equilibrium consideration.

In case of active pier component:

$$V_r = (N_P + N_F + W_F)\frac{l}{h_{eff}} + W_P\frac{l}{2h_{eff}} \tag{2.11}$$

In case of passive pier component:

$$V_r = N_P\frac{l}{h_{eff}} + W_P\frac{l}{2h_{eff}} \tag{2.12}$$

where h_{eff} = web height;
L = length of web;
N_P = superimposed dead load at the top of the web under consideration;
N_F = superimposed dead load at the top of the flange under consideration;
W_P = self weight of the web;
W_F = self weight of the flange.

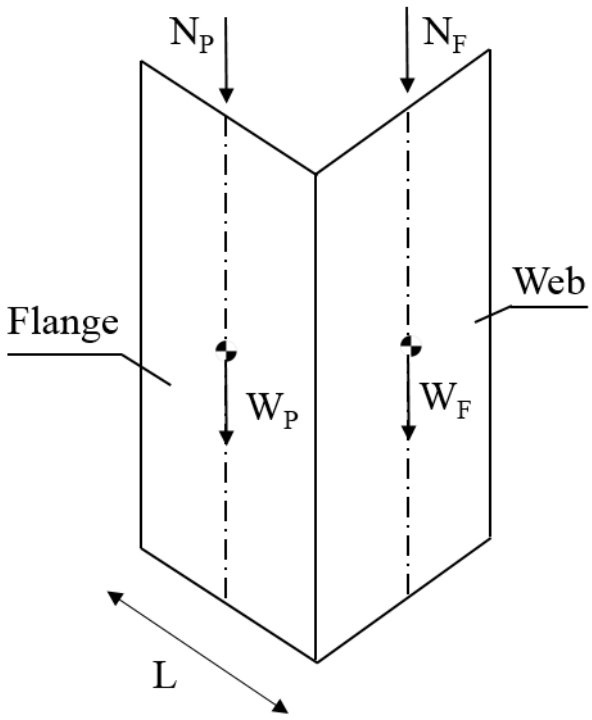

Figure 2.12: Forces acting in a flanged wall

It is important to notice that the formulation proposed here is valid as long as the interlocking between the two orthogonal walls is regarded as strong enough to withstand the load-flow during the earthquake event. Experiments and numerical simulations performed by [50] shows that three possible mechanism can occur (Figure 2.13). Only for case (a), in which the construction tilts, the pier can benefits from the additional weight of the flange.

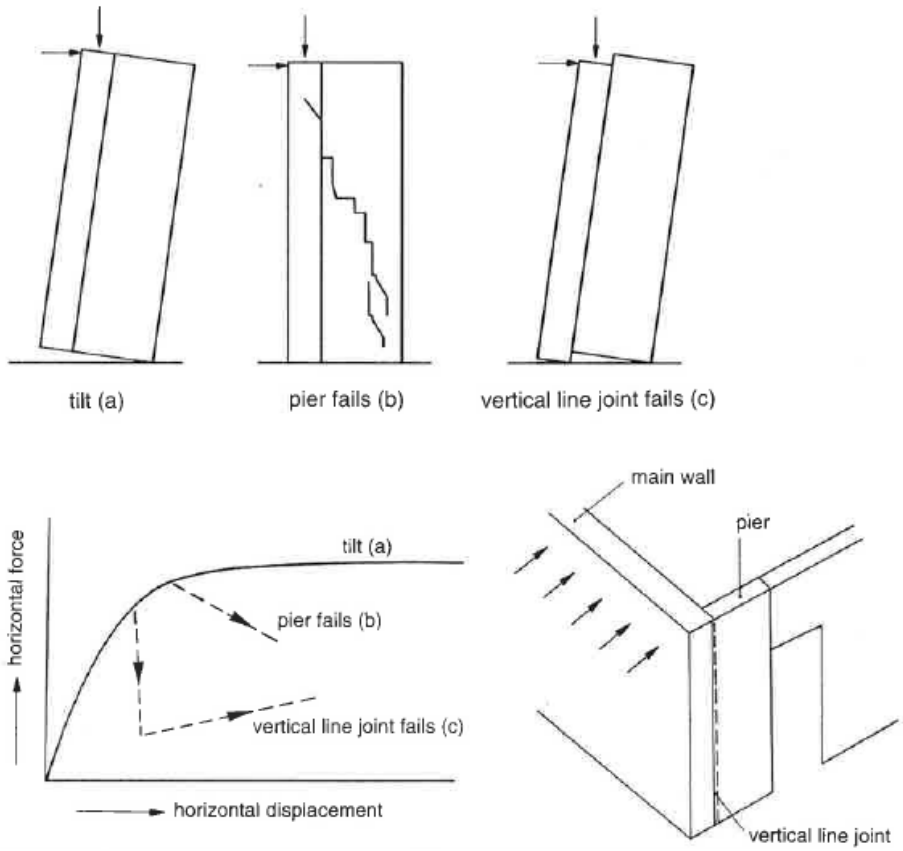

Figure 2.13: Diagram of possible failure mechanisms and accompanying relationship between the horizontal load and horizontal displacement on the top of the main wall:(a) Construction tilts, (b) In-plane pier fails, (c) Interlocking fails. [50]

2.4. Masonry spandrels

Numerical analyses have shown that spandrel beams have a significant influence on the seismic behaviour of URM structures since they influence strongly the stiffness and strength of the structure. However, until today, spandrel elements are often not considered when modelling URM structures because only very limited information on their force-deformation characteristics is available [23]. However, estimates of spandrel strengths, though not confirmed by component tests, can be used to determine if spandrels are likely to be weaker of stronger compared to piers [28].

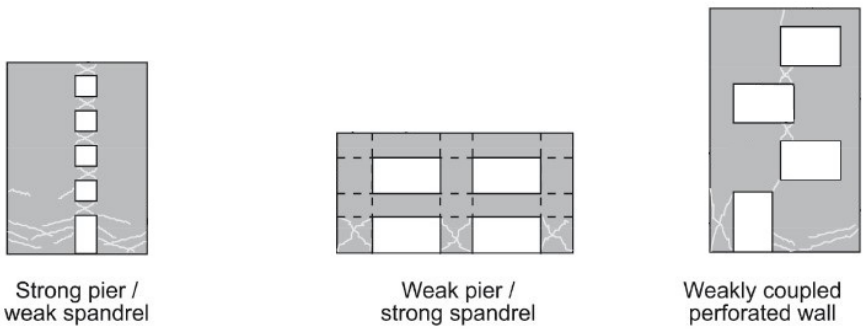

Figure 2.14: Pier/Spandrel Mechanisms

Spandrels that are stronger than piers can couple multiple piers and transmit overturning to adjacent piers, increasing axial forces in end piers and potentially changing the sequence of actions.

Conversely, wall spandrels that are weak relative to adjacent piers may not provide fixity at the tops and bottoms of piers and may result in piers acting as cantilevers. In the following sections indeed, the dynamics behaviour of the pier components is assessed with both cantilever and fix-ended boundary conditions. In such a way, one is able to cover the range of possible configuration of the URM building stock.

2.4.1. Spandrel failure modes

The failure modes of the spandrel can be described by three distinct modes 2.15.

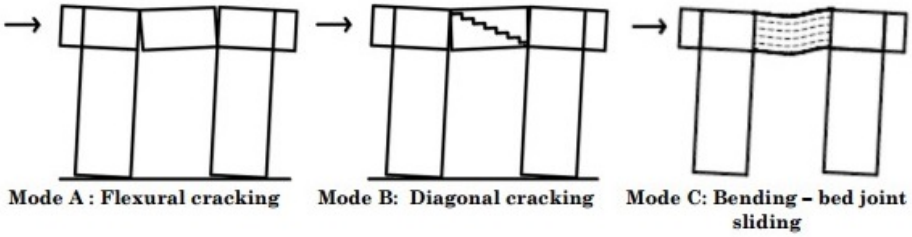

Figure 2.15: Spandrel deforamtion modes [32]

- Mode A is representative of a flexural response where the spandrel panel acts as a rigid block effectively rocking between the two rigid joint panels. Cracking at the spandrel/joint interface was noted as the initial crack location in the average and deep signifying that deformation Mode A occurred first. The initial flexural crack only propagated vertically for the depth of one brick as the bond pattern resulted in a discontinuous vertical mortar joint. This observation is in agreement with proposals for determining the flexural strength of spandrels, which identify the interlocking phenomena as a source of flexural strength. The interlocking originates at the interface between the end section of the spandrel and the joint, due to the contiguous masonry [12].
- Mode B is the most frequently observed failure mode, with stair-stepped diagonal cracking following the mortar joints at increased displacement amplitudes.
- Mode C describes the failure pattern that was observed in substructures which had shallow spandrel depths. This mode is characterised by horizontal cracking that extends over the full length of the spandrel and is evident in multiple courses. This type of failure has not previously been reported as a failure mode for as-built URM spandrels. It has been instead documented after a full-scale test on an URM sub-assembly [5]. Horizontal cracks as failure pattern are reported for spandrel components retrofitted with an inorganic matrix-grid composite.

3

Reduction of Degrees-of-Freedom

In this chapter, the core of the intended approach of the project is presented. The lumped plasticity macro-element model is introduced along with a brief comparison with the smeared plasticity approach. The hysteretic models suitable to capture the masonry failure modes are calibrated using the laboratory tests results and the LS-DYNA numerical simulations.

3.1. SDoF conversion

Traditionally, in seismic engineering, the identification of an approximate structural model, such as equivalent SDoF system, is performed. Often, the capacity curves of a structural system are obtained for the SDoF system, as a way to compare them with the seismic demand, which is in practice defined by elastic response spectra for SDoF systems. The SDoF simplification is usually adopted also for the derivation of analytical fragility curves for buildings subjected to earthquake loading [36].

The standard conversion approach is based on the modal analysis [19] and leads to the definition of an equivalent SDoF, whose mass is computed starting from the modal shape, such that the natural frequency of the lumped system complies with the exact fundamental frequency of the continuous system. This has the advantage of acting as a reasonably simple and fast method, which provides robust results that have been validated in the previous literature, typically frame-structures with mass lumping at floor level [27]. However, the modal analysis is based on linear response of the structure and, hence, does not adjust the conversion to account for non-linear deformed shapes which strongly characterize the dynamic behaviour of masonry buildings.

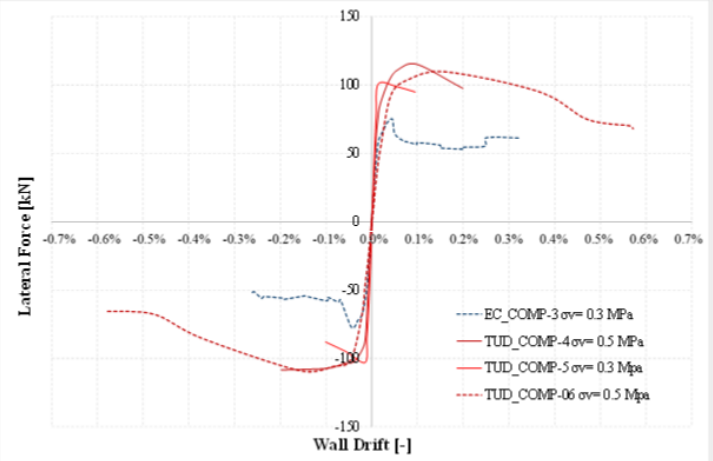

Figure 3.1: In-plane behaviour of URM walls tested in laboratory at EUCENTRE and TU Delft [3]

In literature, few approaches have been proposed for the conversion to an equivalent SDoF system for masonry structures under seismic loading [27] [29] [36]. However, they take into account the non-linear behaviour of the structure when comes to the definition of the structural stiffness (Figure 3.1), but they all assume the structure is moving according to one dominant mode only and that the deformed shape does not change during the earthquake. The typical Dutch residential buildings instead are not characterized by a single dominant mode.

3.2. A lumped plasticity approach

Alternatively, it is favourable to develop a lumped plasticity approach. Indeed, consistent damage observations [32] have identified key failure patterns within perforated in-plane loaded walls, which suggests that perforated wall response due to lateral loading can be explained by delineating the wall into elements, being vertical piers and horizontal spandrels. Damage is typically confined to either the pier or spandrel elements, where shear and flexure failure modes are characteristic of both element types. The underlying hypothesis states that the failure mode of the wall is defined by the failure mode of the individual elements [16].

For such reasons, according to [33][49] [51],the frame modelling strategy is a valuable approach for masonry structures idealization. This in fact consists in subdividing each resistant masonry wall in a set of deformable masonry elements (piers and spandrels), in which the deformations and the non-linear responses are concentrated, and rigid panels that connect the deformable elements (see Figure 3.2).

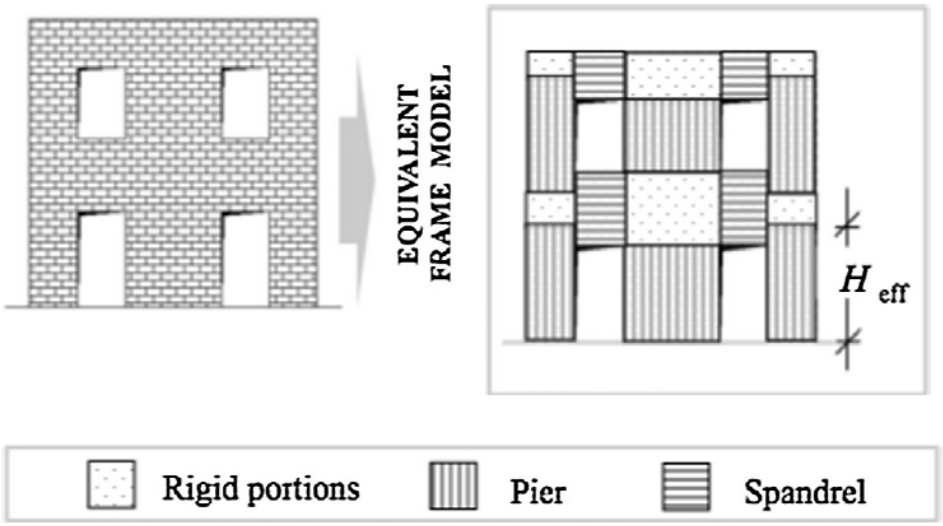

Figure 3.2: URM wall idealization according to simplified and equivalent frame model [33]

The non-linear behaviour of the equivalent frame model is introduced by assigning inelastic discrete hinges. In the lumped plasticity method, the pier elements are modelled with frame elements having elastic properties based on the pier dimensions and assumed material properties. The non-linear behaviour is captured via the localised hinges introduced into the frame element. The hinges only engage into plastic deformation when the yield capacity of the hinge mechanism is reached.

3.3. Smeared plasticity approach

Before the definition of the macro-element framework, in this section an overview of the smeared plasticity masonry model is included. This is essential for the understanding of the calibration and validation exercises reported below. An Arup development version of the LS-DYNA software containing a user defined masonry material model is used. It consists in a smeared crack formulation with crack plane directions pre-defined according to mortar planes (bed joints and head joints). The model has been developed for shell elements, which are particularly suitable for the representation of components with uniform thickness and in-plane extents much greater than their thickness. It is the case of the thin URM walls than characterise the Groningen building stock.

The inelastic stress strain constitutive low is representative of the crack opening, closing and shearing. The opening displacement of cracks is tracked, so that they open and close in a realistic manner under hysteretic loading. Compression can be carried across closed cracks. The shear strength of bonds is the sum of a cohesion component and a friction component. The cohesion and tensile strength of the bonds decay to zero according to a rate independent damage law, while the friction coefficient remains constant. Tensile failure of the bed joints is defined by a tensile strength and an energy release rate as illustrated in Figure 3.3. The same bed-joint tensile response governs in-plane and out-of-plane failure modes.

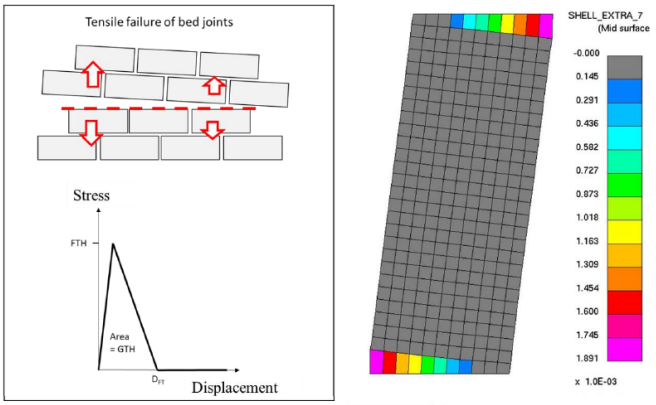

Figure 3.3: Tensile response of bed joints governing the in-plane failure

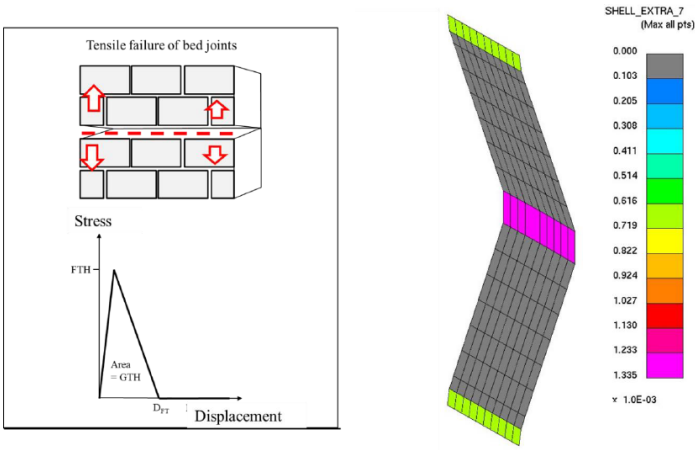

Figure 3.4: Tensile response of bed joints governing the out-of-plane failure

Regarding the bed-joint response (Figure 3.5), the shear strength consists of a friction term and a bond strength term. The bond strength decreases with shear displacement according to an energy release rate, which increases with compressive stress normal to the joint. The input value of energy release rate applies at zero compressive stress. The shear stress is taken as the resultant of in-plane and out-of-plane shear stresses, thus in-plane and out-of-plane sliding are both taken into account.

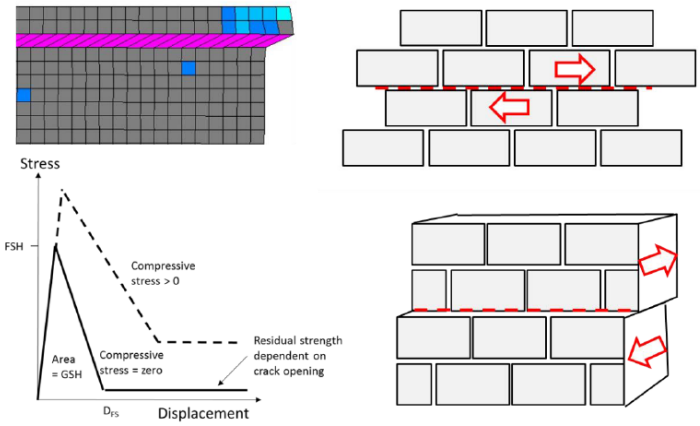

Figure 3.5: Shear response of mortar bed-joints

Finally, the diagonal cracking mode can be captured. However, only the propagation through head- and bed-joints is allowed. Vertical cracks through the bricks are not described by the fracture mechanics law.

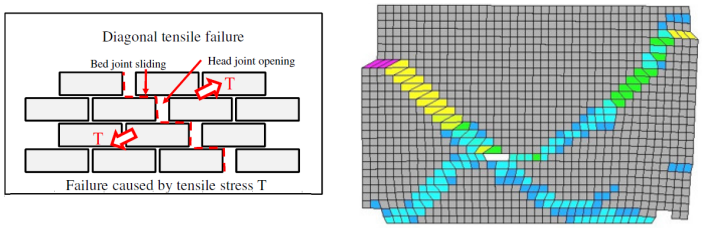

Figure 3.6: Diagonal cracking through head- and bed-joints

Furthermore, the material model is implemented including element erosion techniques based on different criteria:

- in-plane sliding displacement greater than half the brick length;
- out-of-plane sliding displacement greater than half the brick thickness;
- bed-joint opening gap grater to the height of the brick;
- compression strain grater than the ultimate strain in the compression curve (Figure 3.7).

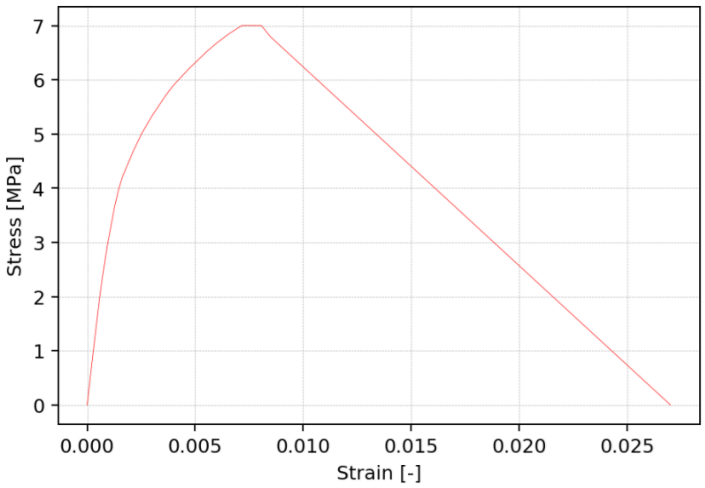

Figure 3.7: Stress-strain compression curve of the masonry material model

3.4. Macro-element

The core of the aforementioned equivalent-frame approach is the so-called macro-element. It is an assembly meant to represent the fundamental in-plane behaviours of masonry piers. In this framework, each behavioural mechanism has an associated hinge, characterised by a non-linear force-displacement (or moment-rotation) curve. The curves are calibrated with the geometrical properties of the pier, masonry material properties and its vertical load. In such a framework, the connections between horizontal members and walls are assumed not to reach failure. In this way, one is sure that the dynamics behaviour is driven by the in-plane behaviour of the wall components. The assembly is built up with two Euler-Bernoulli elastic beams, connected via a translational springs placed at mid-pier height. At the two ends of the assembly, two rotational springs are placed (see Figure 3.8).

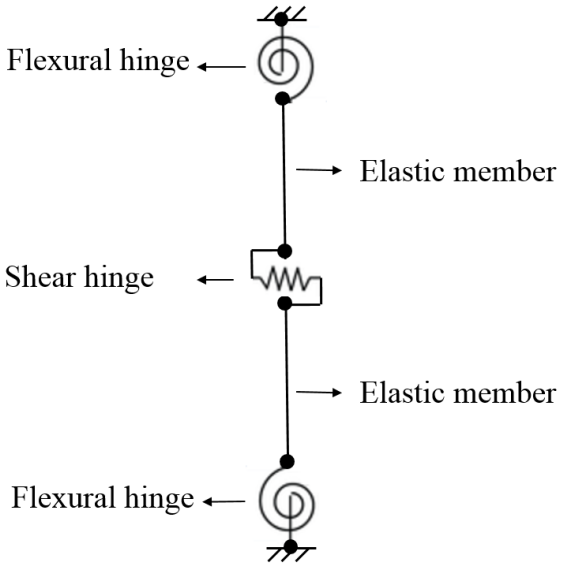

Figure 3.8: Macro-element model for in-plane pier behaviour

3.4.1. Stiffness of zero-length springs

As presented in Chapter 2, the in-plane stiffness of UMR piers is given by the contribution of the flexural and the shear component. The macro-element assembly is modelled by sub-elements connected in series: plastic hinge rotational springs at member ends, translational spring at mid-heigh and two elastic beam-column element. Therefore, the structural properties of the member are a combination of the properties of the sub-elements. Firstly, the stiffness matrix of an Euler-Bernoulli beam element can be written as follow [58]:

$$K = \frac{EI}{l^3}\begin{bmatrix} 12 & 6l & -12 & 6l \\ \dots & 4l^2 & -6l & 2l^2 \\ \dots & \dots & 12 & -6l \\ \dots & \dots & \dots & 4l^2 \end{bmatrix}$$

The stiffness matrix of a zero length spring element is expressed as:

$$K = \begin{bmatrix} \mu & -\mu \\ -\mu & \mu \end{bmatrix}$$

By assembling the two stiffness matrices, it is possible to come up with the global stiffness matrix of the system shown in Figure 3.9. Hence, the in-plane structural stiffness is computed applying a unit displacement at one end-node and enforcing the boundary conditions at the two end-nodes, and solving the system of equations $f = \mathbf{k}u$. This results in the following expression:

$$K^* = \frac{12EI}{l^3}\frac{l\mu}{6EI + l\mu} \tag{3.1}$$

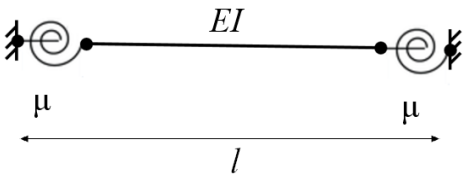

Figure 3.9: Euler-Bernoulli beam with rotational springs

The structural stiffness of pier member K_{mem} can be related to the stiffness of the beam with hinges $K*$ (Equation 3.2) and the stiffness of the translational spring K_s, according to the following equation:

$$K_{mem} = \left(\frac{1}{K^*} + \frac{l}{K_s} \right)^{-1} \tag{3.2}$$

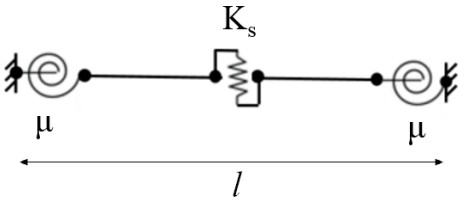

Figure 3.10: Macro-element assembly

In order to define an element representative of the in-plane stiffness expressed by Equation 2.2, evident choices for sub-element stiffnesses appear to be either:

- $EI = \infty$, in which case $K_s = \frac{GA_s}{l}$ and $\mu = \frac{EI}{l}$;
- $\mu = \infty$, in which case $K_s = \frac{GA_s}{l}$.

However, both are not desirable in the context of numerical analysis. The first option, corresponding to an infinite beam stiffness, would force all deformations into the plastic hinges springs which would lead to the following problems:

- The elastic spring stiffness, which has to be defined a priori, would be the same regardless of the moment gradient in the beam element. In reality, the moment gradient may change during the NLTH analysis, which would not be accounted for in this model;
- All damping would have to be assigned to the rotational springs, which causes spurious damping moments at frame joints when one chooses damping formulation based on initial member stiffness.

On the other hand, considering an infinite rotational spring stiffness would cause numerical instability problems related to the integration of the differential equation with time-stepping techniques (e.g. Newton-Raphson). Following the approach presented in [31], in order to avoid the issues related with the second option, and minimize those related with the first, it has been decided to set the stiffness of the shear spring K_s equal to $\frac{GA_s}{l}$, the rotational stiffness $\mu = \frac{2EI}{l}$ and consequently adopt a increased moment of inertia $I_{mod} = 4I$.

3.4.2. Flexural spring calibration

The flexural behaviour of the masonry pier is captured by the rotational springs located at the two ends of the piers. They are meant to represent the rocking failure mode presented in Chapter 2. The choice of lumping the springs at pier ends is dictated by the nature of such a failure mode. As presented in Figure 3.12, the plastic deformation for the rocking mechanism is usually lumped at pier ends, as bed-joint opening occurs or a localized diagonal mode trough both the horizontal and vertical joints. This is indeed observed in the quasi-static tests performed on CaSi specimens (Figure 3.11).

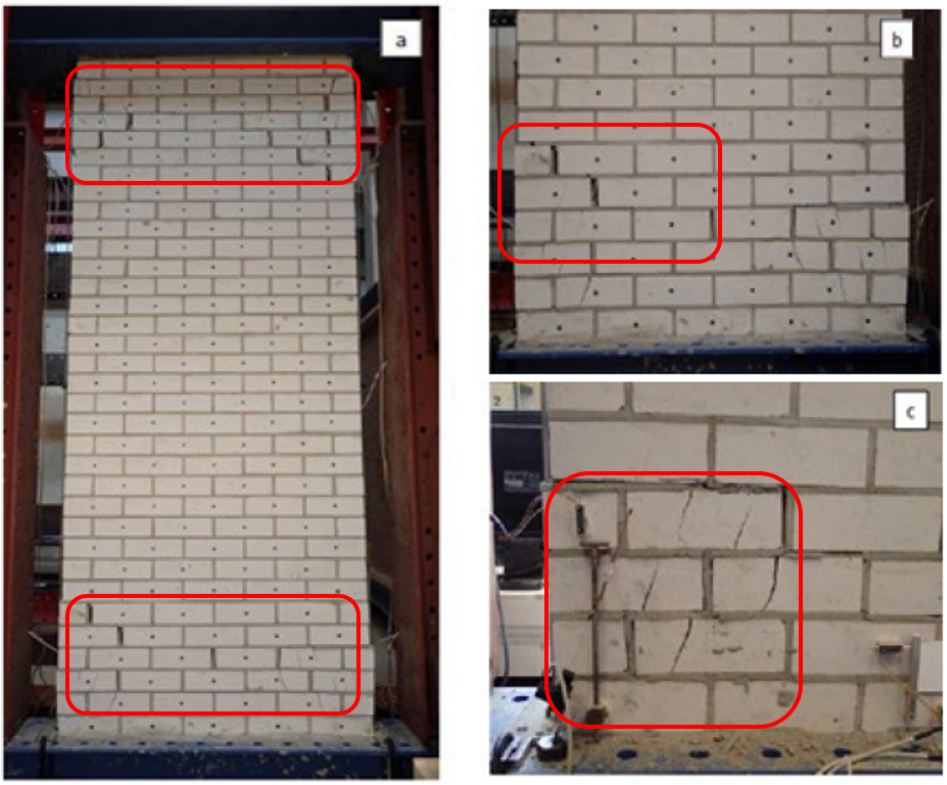

Figure 3.11: Typical rocking-related damage patter observed in CaSi URM piers[3]

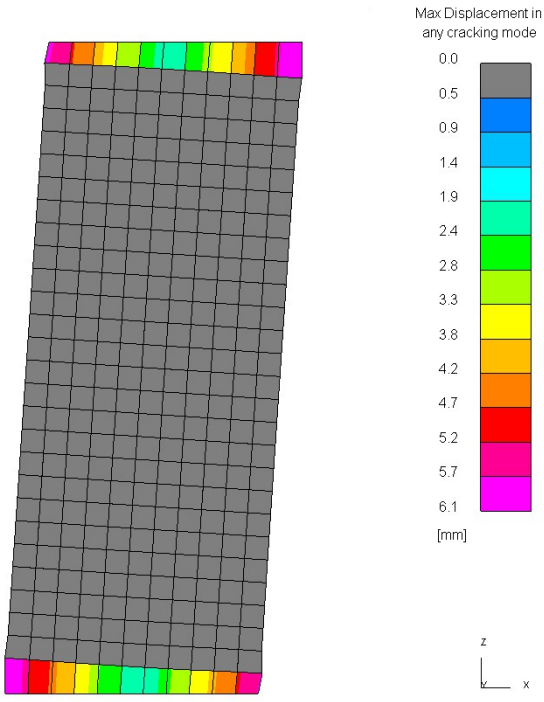

Figure 3.12: Rocking damage plot predicted by a LS-DYNA for quasi-static analysis of a slender pier

As introduced in the previous chapter, during a displacement control test, the component starts deforming elastically. Once the lateral actions overcome the vertical forces, the wall starts to tilt around its toes, leading to the so-called gap opening. During the unloading, the gap closes until the wall starts moving elasti-

cally again in the other direction.

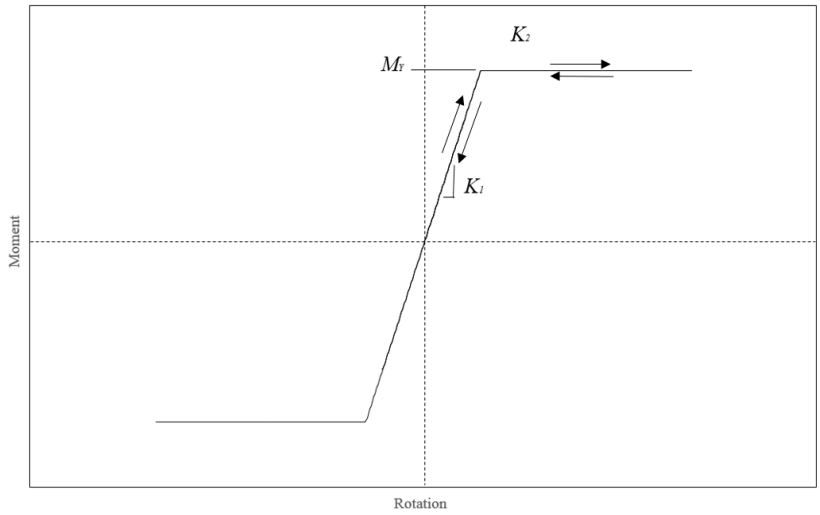

Figure 3.13: Idealized rocking behaviour with a non-linear elastic moment-rotation relationship

During the gap opening and closing, low-dissipative mechanisms occurs. It is the effect of the sliding along the head- and bed-joints, that can be noticed in Figure 3.11, and the non-linear behaviour at the corners around which the component tilts. Therefore, during the un-loading the specimen does not follow exactly the loading curve, but produces narrow loops before re-centering around the un-deformation position.

For the rotational springs, the OpenSees self-centering hysteretic models [37] is adopted. It provides the abstraction for a one-dimensional rate-independent flag-shaped hysteresis (Figure 3.14). A similar force-displacement behaviour is observed in the laboratory component testing [3], and described by [38] and [35].

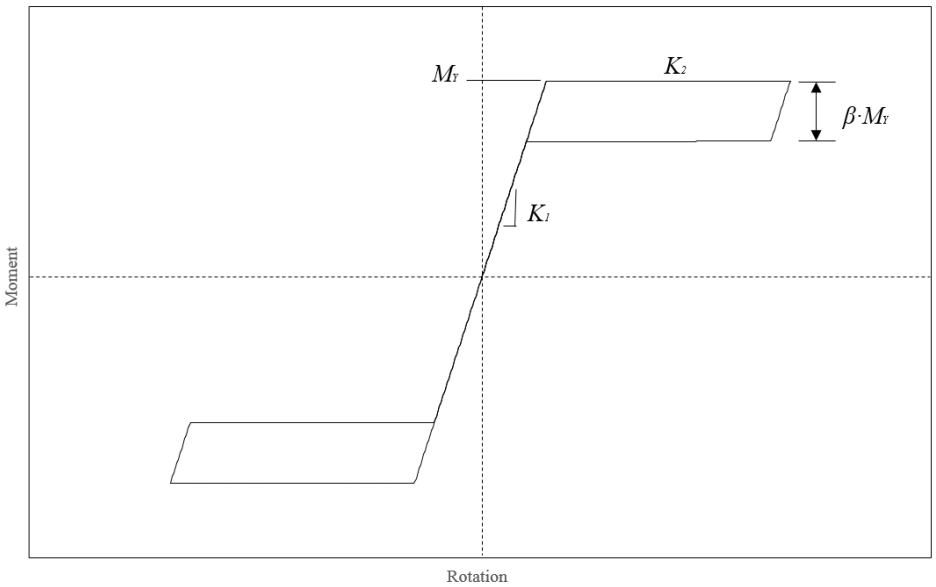

Figure 3.14: Parameter definition of the flag-shape hysteretic model for rotational springs

M_y	Activation Moment
K_1	Initial Stiffness
K_2	Post-Activation Stiffness
β	Ratio of Forward to Reverse Activation Moment

The yielding moment is calculated with the capacity expression given in Section 2.1.2. The initial elastic tangent is to be computed based on the formulation given in Section 3.4.1. Particular attention is required for the parameter β. It controls the size of dissipative loops in the model, and it is meant to capture the energy dissipation at the two specimen ends. Being phenomenological rather than based on mechanics principles, a multi-objective genetic algorithm [18] is adopted for the estimation the β parameter. By seeking for the closest fit to the LS-DYNA force-displacement curves, one is able to come up with the optimal sets of parameters which is representative of the dissipative rocking behaviour of CaSi URM wall components. In this case, the set of parameters is reduced only to one, namely the β parameter, since the backbone curve relies on the mechanics principle presented in Chapter 2. In the figure below, the results of the optimization algorithm is presented. In particular, for each quasi-static test performed with LS-DYNA on wall resembling specimens tested at EUCentre and TU Delft, the parameter is plotted, as a way to come up with an average value representative of the CaSi wall components. This value is later adopted for the dynamic tests.

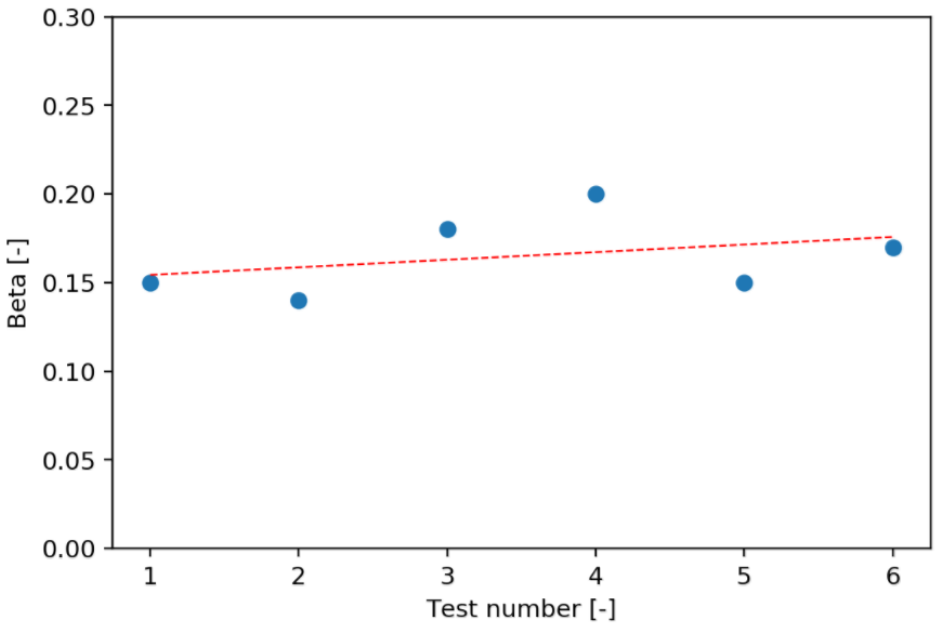

Figure 3.15: β parameter of the optimization algorithm

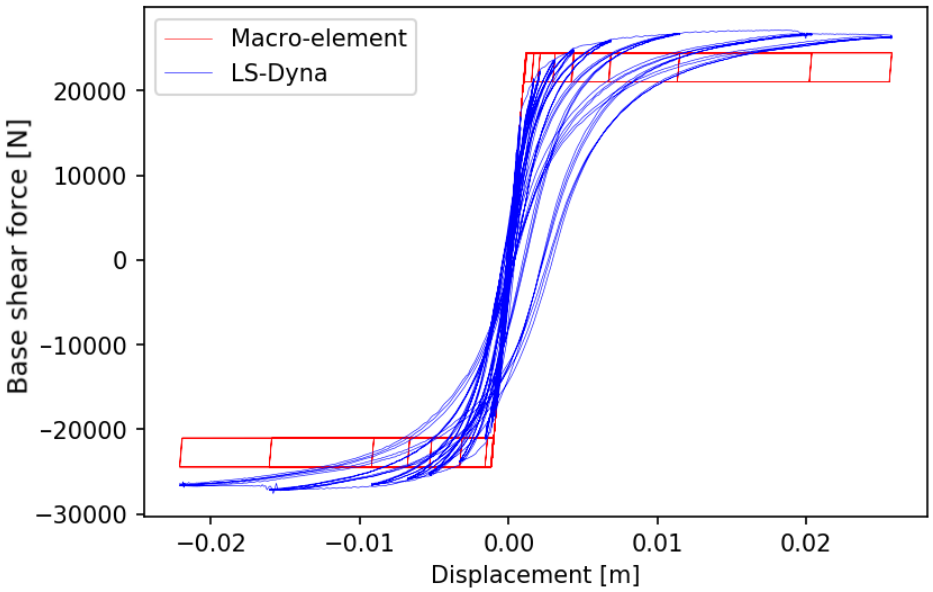

Figure 3.16: Hysteresis curve comparison for a rocking pier component - LS-DYNA and macro-element

Table 3.1: Summary table: comparison LS-Dyna and Macro-element results on a slender pier component

Test	Predominant failure	Initial Stiffness [kN/m]	Peak Strength [kN]	Dissipated Energy [N·m]
Macro-element	Rocking	32.1	25	1320
LS-DYNA	Rocking	29.7	28	1370

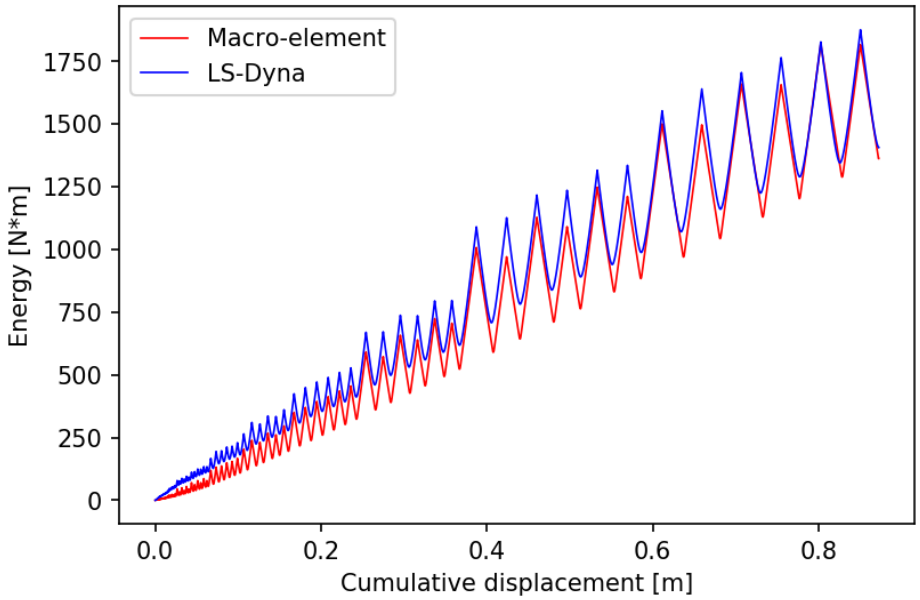

Figure 3.17: Internal energy comparison - LS-DYNA vs macro-element

In is important to notice the different rocking behaviour observed in the laboratory tests, compared to the smeared plasticity numerical simulation.

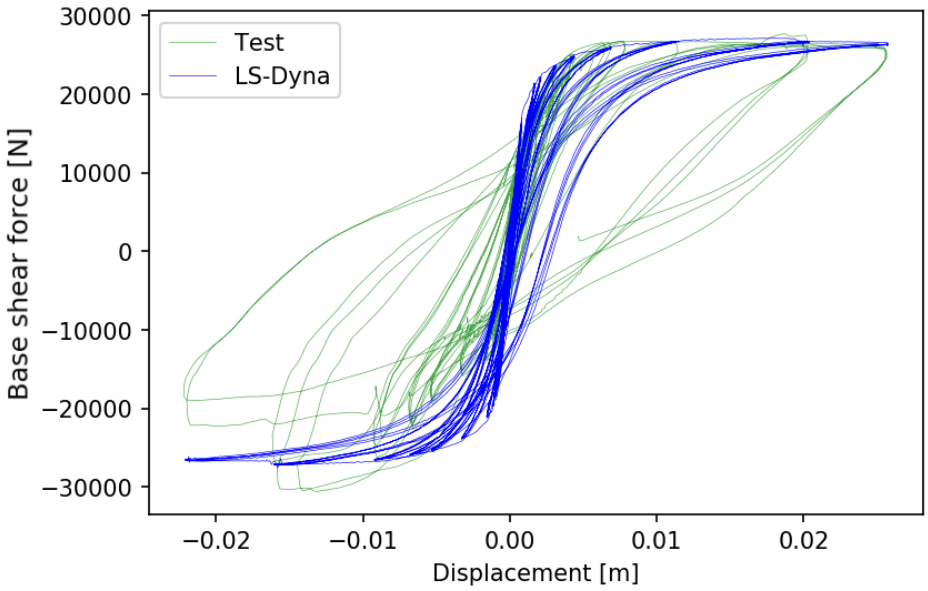

Figure 3.18: Force-displacement curve comparison for specimen failing with rocking mechanism - Test vs LS-DYNA

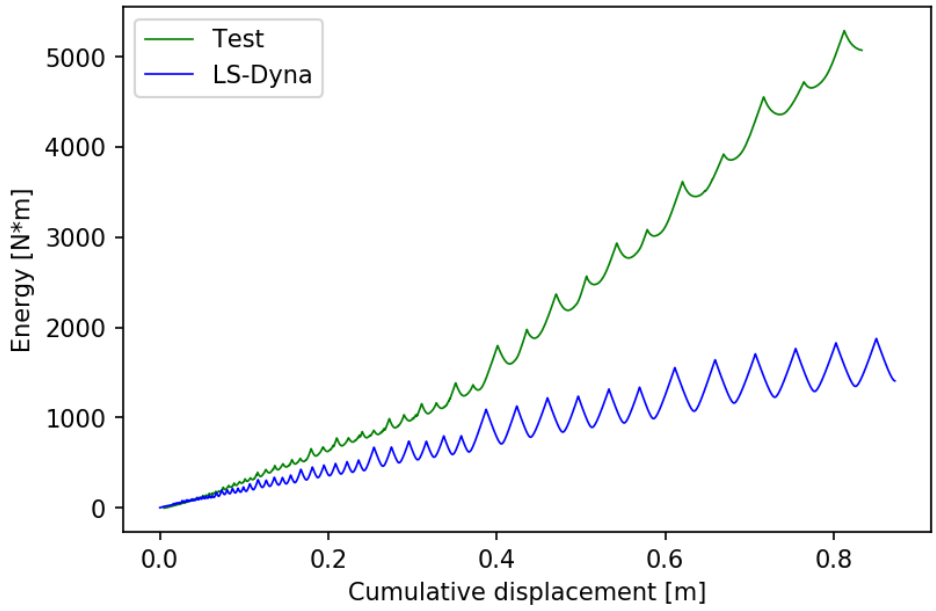

Figure 3.19: Internal energy comparison - Test vs LS-DYNA

The backbone parameters are in good agreement, whilst the energy dissipation predicted by LS-DYNA is always lower compared to the test results.

Table 3.2: Summary table: comparison LS-DYNA and Lab test results on a slender pier component

Test	Predominant failure	Initial Stiffness [kN/m]	Peak Strength [kN]	Dissipated Energy [N·m]
Lab	Rocking	25.8	30	5020
LS-Dyna	Rocking	29.7	28	1370

This is related to the masonry behaviour in compression. First, during the tilting, around the toes the stress state varies from compression to zero value (tension is not allowed as the mortar bed-joint opens).

During the un-loading and reloading, in the LS-DYNA material model, the curve follows the same path, while compression tests on URM wallets shows the presence of dissipative loop originated during the un-loading re-loading behaviour. In this regard, the numerical simulation is on the conservative side.

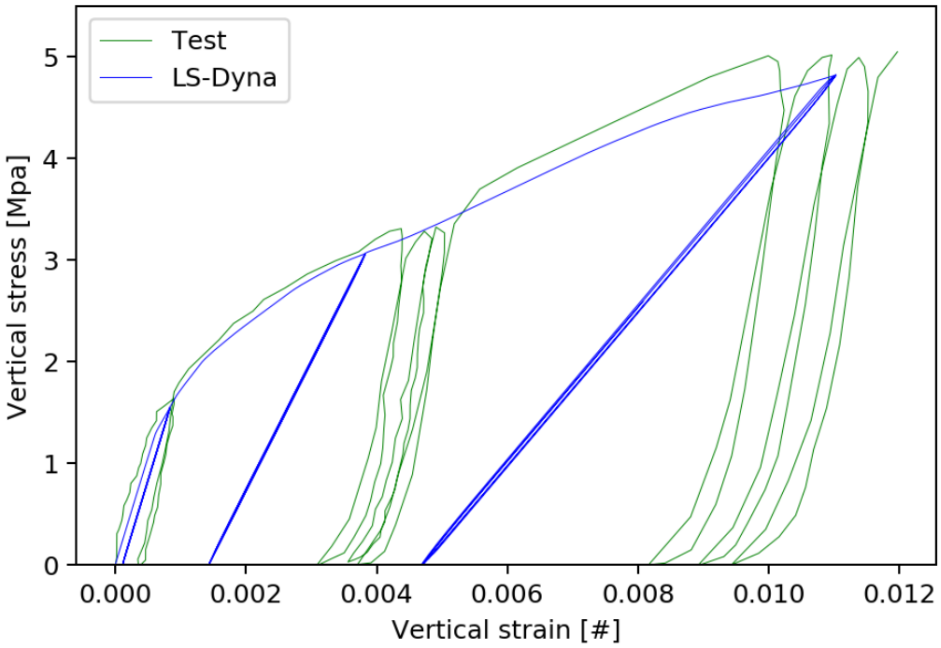

Figure 3.20: Compression test of URM masonry wallets - stress-strain comparison between LS-DYNA and the laboratory test [3]

Flange effect As described in Section 2.3, in case there is full interlocking with the orthogonal transversal wall, the in-plane web can benefits from the additional weight of the flange (see appendix E). In fact, for equilibrium considerations, if the flange is in tension, its weigh acts as a stabilizing force for the system. This has been observed also from quasi-static tests performed with LS-DYNA, comparing slender wall with and without flanged section (Figure 3.22).

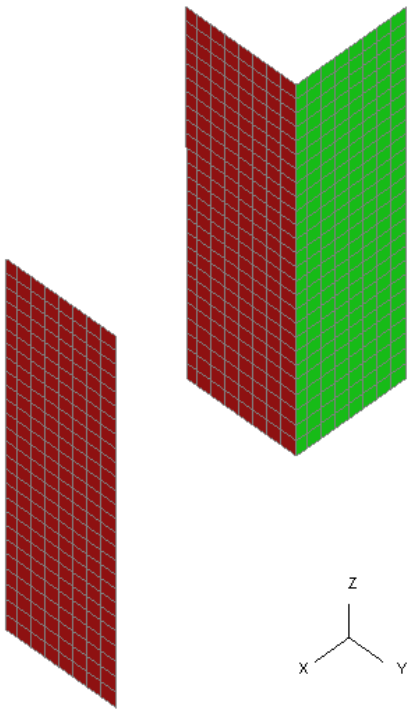

Figure 3.21: Geometry definition for the flange effect study on a slender component

The force displacement curves for the two specimens are compared to assess the contribution of the flange effect.

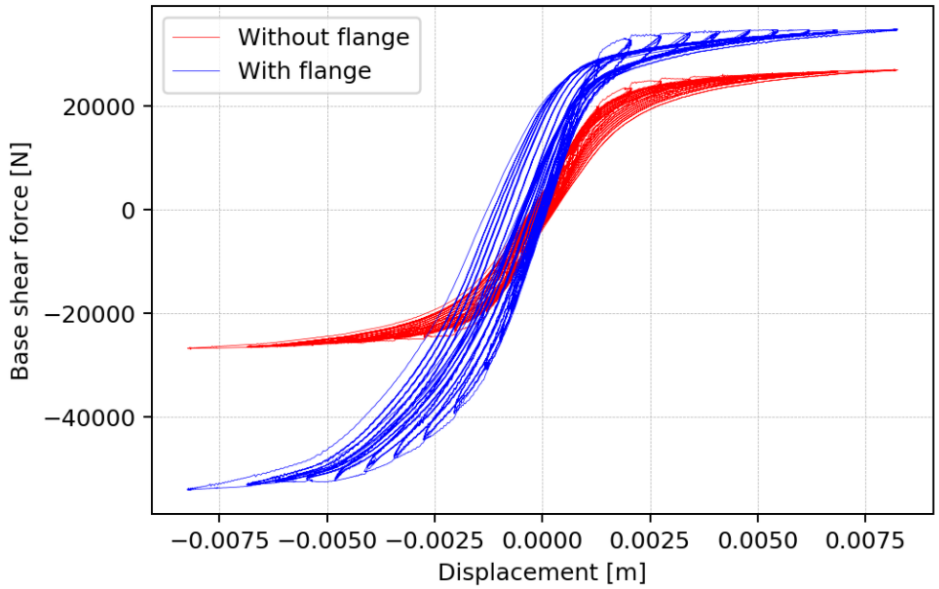

Figure 3.22: Hysteretic curves comparison for a slender wall component: rectangular and flanged section

One may notice that the presence of the orthogonal wall leads to an asymmetric backbone in the two directions, with significantly different yielding forces. This behaviour is described analytically in the previous chapter. A new flag-shape material model has been developed (C++) and included in the OpenSees source code. It relies on the same mechanics of the flag-shape model presented in Figure 3.14, but offers the possibility to define a different activation moment for positive and negative rotations.

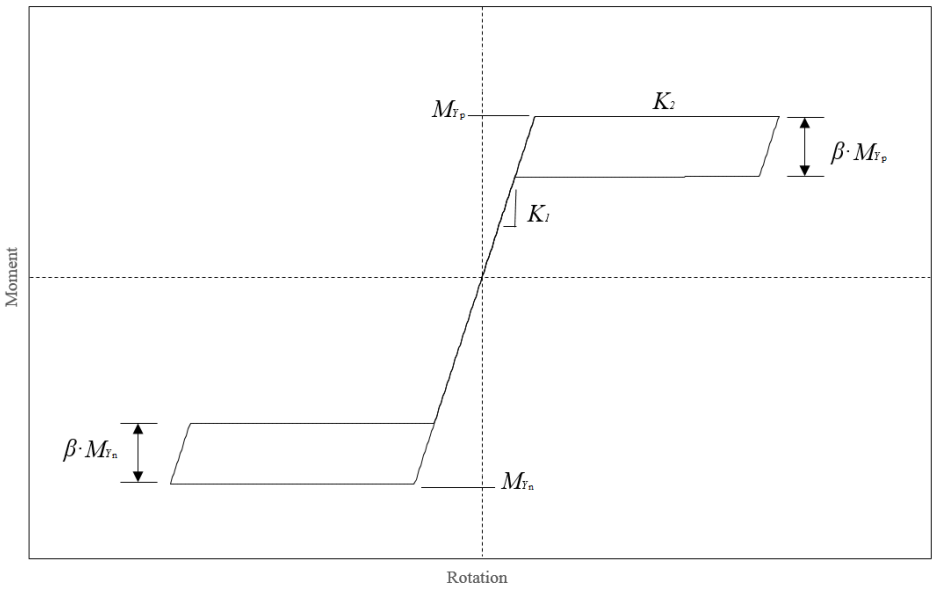

Figure 3.23: Parameter definition of the modified flag-shaped model for flange effect

M_{yp}	Activation Moment in the positive direction
M_{yn}	Activation Moment in the negative direction
K_1	Initial Stiffness
K_2	Post-Activation Stiffness
β	Ratio of Forward to Reverse Activation Moment

3.4.3. Shear spring calibration

The inelastic shear behaviour of URM walls is modelled via the translational spring located at of half of the pier heigh. This is meant to be representative of the in-plane shear failure modes, namely, bed-joint-sliding and diagonal tension presented in Chapter 2. The choice of lumping the shear spring at half heigh is dictated by the nature of the failure modes observed during the testing campaign at TU Delft and EUCentre (Figure 3.24). As presented in Figure 3.25, the plastic deformation for such mechanisms is usually lumped around half of the pier height, rather than the two ends, like in the case of the flexural behaviour.

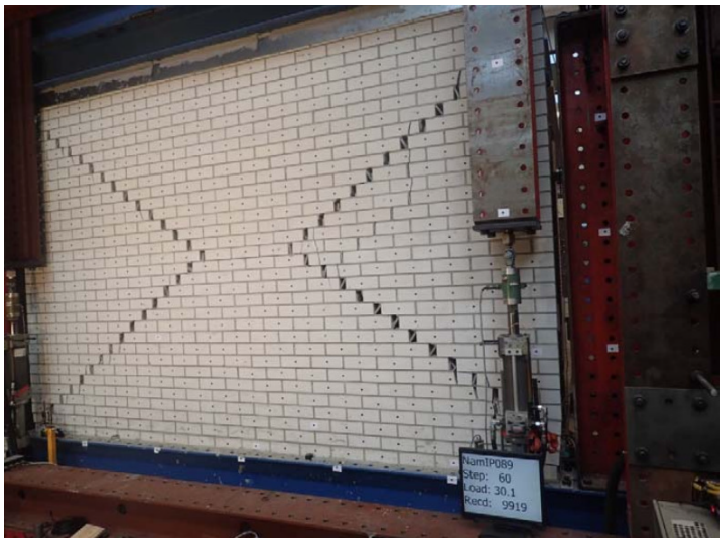

Figure 3.24: Diagonal tension: damage plot observed in the laboratory components test[3]

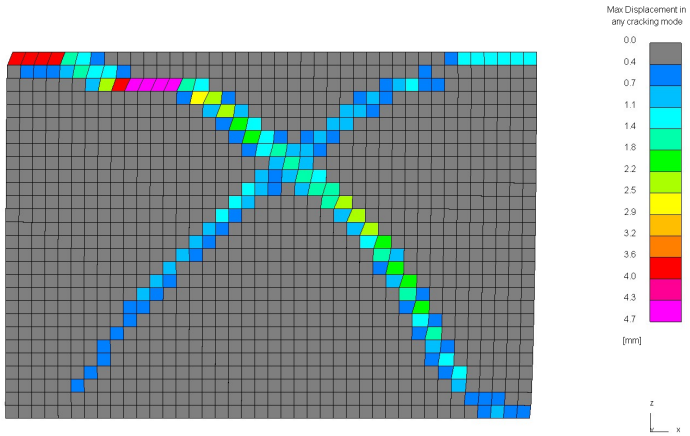

Figure 3.25: Diagonal tension: damage plot at end of analysis with LS-DYNA [3]

For the shear spring, an OpenSees bilinear model is adopted [37]. The hysteretic behaviour is characterised by parallel loading and un-loading behaviour and smooth transition between initial and post-yielding stiffness.

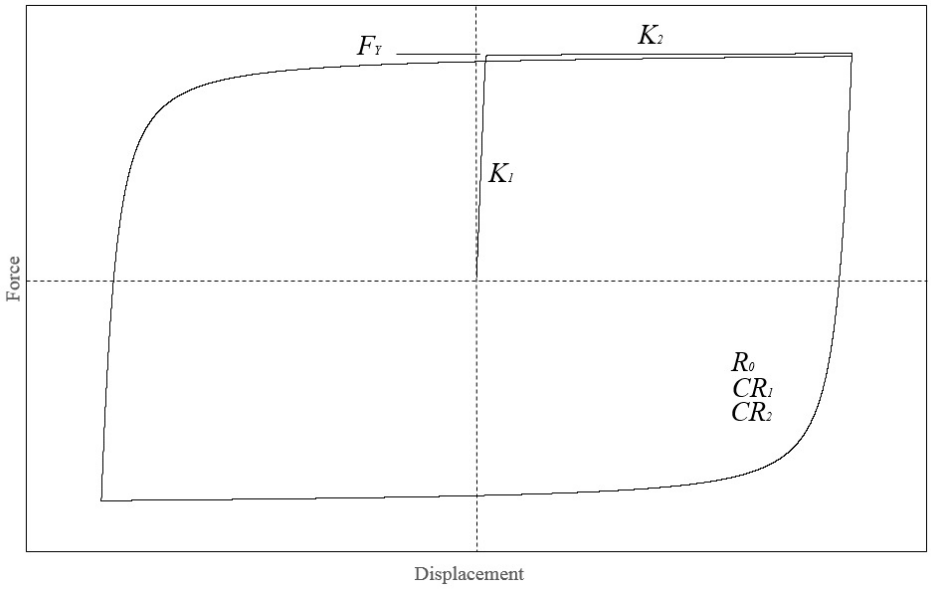

Figure 3.26: Elasto-plastic material model adopted for the shear springs

F_y	Yield strength
K_1	Initial elastic tangent
K_2	Ratio between post-yield tangent and initial elastic tangent
R_0, CR_1, CR_2	Parameters to control the transition from elastic to plastic branch

The mechanics of such a model resembles the behaviour observed during the laboratory component testing [3], (Figure 3.27), and the LS-DYNA simulations results (Figure 3.25). For the shear spring yielding force, the smaller between the value calculated according to the bed-joint-sliding and the diagonal cracking formulation is used. The initial elastic tangent is to be computed based on the formulation given in Section 3.4.1.

In the figures below, a comparison between the laboratory test and the developed macro-element is presented. It is a quasi-static test of a squat wall component. The results are compared in terms of force-displacement curves and internal energy history.

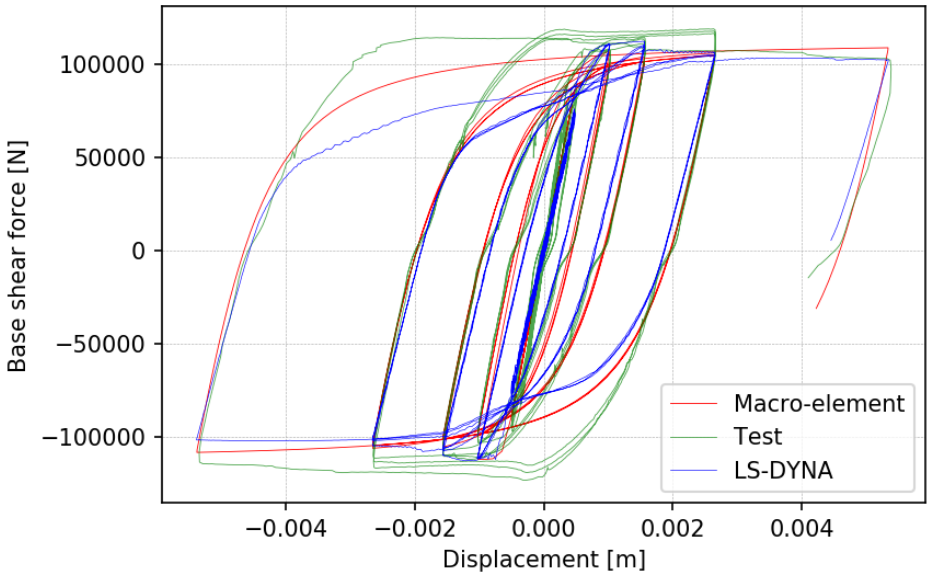

Figure 3.27: Lab force displacement curve for specimen failing in shear [3]

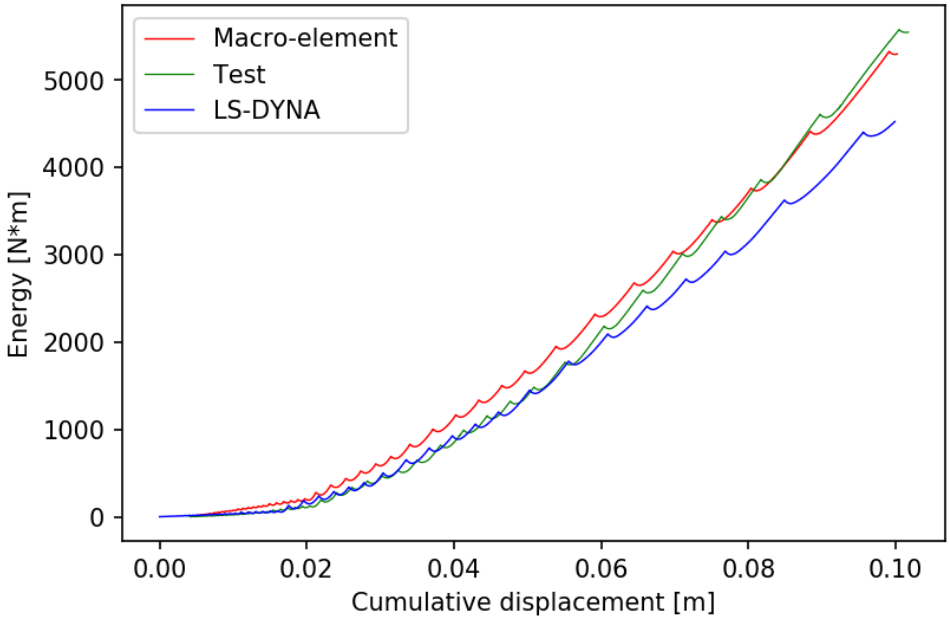

Figure 3.28: Internal energy comparison - LS-DYNA, macro-element and laboratory tests

Table 3.3: Summary table: comparison Lab Test and Macro-element results on a squat pier component

Test	Predominant failure	Initial Stiffness [kN/m]	Peak Strength [kN]	Dissipated Energy [N·m]
Macro-element	Diagonal cracks	219	102	5240
Lab	Diagonal cracks	223	119	5320
LS-DYNA	Diagonal cracks	223	119	5320

One should notice the initial stiffness and peak strength are in good agreement, as well as the energy dissipation. In general, the macro-element seems to provide results on the conservative side, with less than 10% discrepancy from the test.

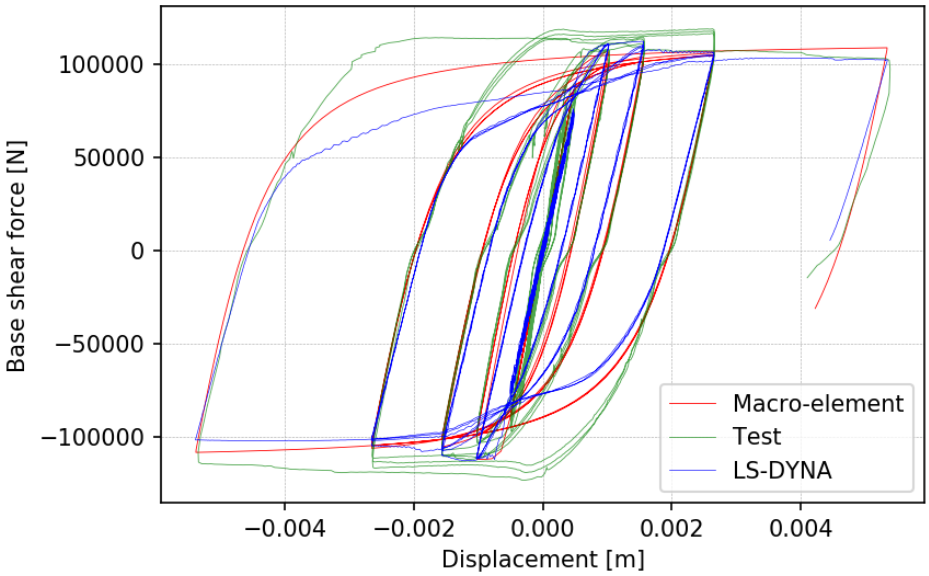

Figure 3.29: Hysteretic curve comparison - LS-DYNA vs Laboratory test

Flange effect Analogously to what discussed to the flexural springs, the effect of a potential orthogonal wall attached to the in-plane flange is analysed.

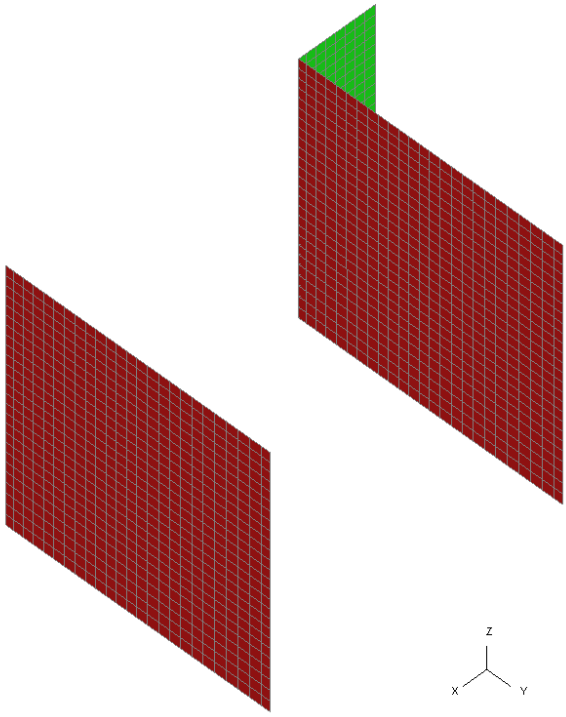

Figure 3.30: Geometry definition for the flange effect study on a squat component

The force displacement curves are in agreement to the literature studies. For shear dominated building, the presence of the flange does not significantly affect the response of the web. The mechanics of sliding or diagonal cracking modes is such that no uplift can occur. Indeed, they act as purely translational motions, and the additional weight of the flange is not included (see deformed shape in Appendix E). Therefore, it is suggest to conservatively neglect the contribution of the orthogonal wall and describe a symmetric backbone for the shear spring constitutive law.

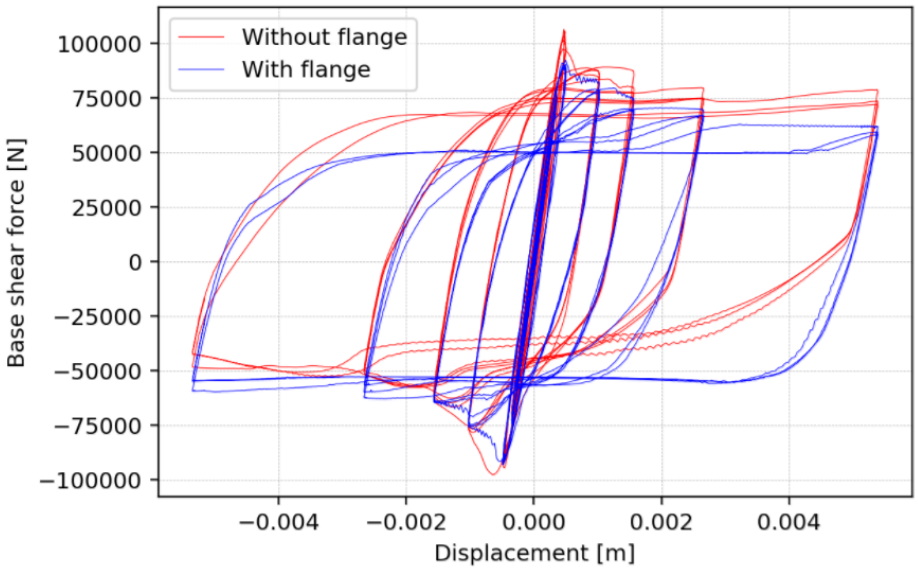

Figure 3.31: Hysteretic curves comparison for a squat wall component: rectangular and flanged section

3.4.4. Mass distribution

The distribution of mass within an URM building differs from the distribution in a typical reinforced concrete frame building as the majority of the mass is within the walls themselves. Therefore a lumped mass model where the mass is only lumped at the diaphragm level does not accurately portray the distribution of mass within the wall [32]. Hence, a key part in the definition of the macro-element is the mass distribution along the heigh of the element. Rotational inertia is neglected and the pier mass is distributed along the 4 nodes, contributing in the in-plane translational inertia of the component (Figure 3.32). This choice has been validated by performing eigenvalue analyses for a squat pier model with cantilever condition. In particular, the modal analysis has been performed with the software LS-Dyna and GSA, on the wall modelled with 2D shell elements. Furthermore, the eigenvalue analysis has been performed for a Timoshenko beam model and finally, the proposed macro-element. The fundamental period for each of the above system is reported in Table 3.4.

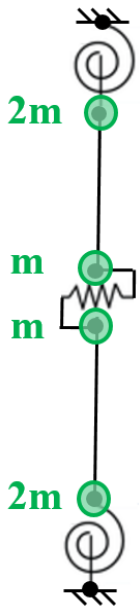

Figure 3.32: Macro-element mass distribution

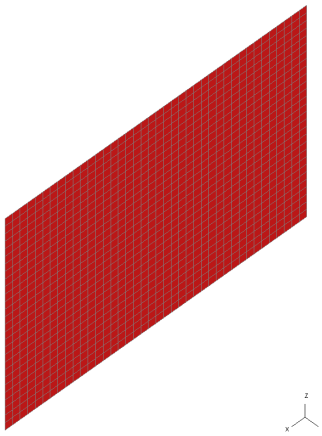

Figure 3.33: Squat pier with cantilever boundary conditions

Table 3.4: Eigenvalue analysis results for different pier modelling approaches for a squat pier with cantilever condition

System	First Natural Period [s]
2D shell wall (LS-DYNA)	0,01695
2D shell wall (GSA)	0,01664
Timoshenko beam	0,01683
Macro-Element	0,01721

The same approach has been followed for a slender pier with fix-fix condition (Table 3.5).

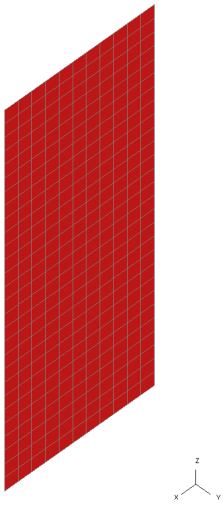

Figure 3.34: Slender pier with fix-fix boundary conditions

Table 3.5: Eigenvalue analysis results for different pier modelling approaches for a slender pier with fix-fix condition

System	First Natural Period [s]
2D shell wall (LS-DYNA)	0,09321
2D shell wall (GSA)	0,09313
Timoshenko beam	0,09311
Macro-Element	0,09421

4

Non-Linear Time History Analysis

In this chapter, the NLTH procedure for the evaluation of the transient response of inelastic systems is described. Particular attention is given on the the integrator type for the smeared plasticity and the macro-element model. The NLTH analyses are performed using the platform OpenSees (Open System for Earthquake Engineering Simulation), developed at the University of California, Berkeley and the Pacific Earthquake Engineering Research Center [37]. Benchmark results are produced by the software LS-DYNA with the Arup-developed masonry material model. Finally, an insight on the viscous damping modelling and the hysteretic damping is presented.

4.1. Numerical evaluation fo the dynamic response

The evaluation of the dynamic response of elastic system due to an external excitation is traditionally based on modal analysis. The general solution is composed of the sum of the homogeneous solution and a particular solution. It is therefore necessary to first solve the homogeneous system, assuming a synchronic harmonic motion for the free vibration. Analogously, the particular solutions is also assumed to be a summation of eigenvectors, each of which is multiplied with an unknown time function. In mathematical terminology, it is thus assumed that also in the case of forced vibration the response can be expanded in eigenvectors each weighed with an unknown time function. Hence, by means of the orthogonality condition of the mass and stiffness matrices, the system is decoupled into set of inhomogeneous differential equations. The uncoupling of the modal equation however, is not possible if the system has non-classical damping or it responds into non-linear range. This is the case in URM structures, which deform inelastically already at low intensity excitations (see Figure 3.1). Hence, for such systems, coupled equations of motions in nodal coordinates need to be solved by numerical methods. The time scale is divided into a series of time steps of constant duration.

The equation of motion is then evaluated at a selected time instant. If it is the current time t_i, the integration method is said to be explicit. If the time t_{i+1} at the end of the time step is used, the method is known as implicit.

For an inelastic SDoF system subjected to an earthquake excitation the general equation of motion to be solved numerically is:

$$m\ddot{u} + c\dot{u} + f_s = -m\ddot{u}_g \tag{4.1}$$

where m = mass of the system;
c = damping coefficient;
$f_s = f\big(u, sgn(\dot{u})\big)$, the resisting force;
$\ddot{u}_g$ = earthquake acceleration.

The system is subjected to the generic initial conditions:

$$u_0 = u(0) \quad \text{and} \quad \dot{u}_0 = \dot{u}(0) \tag{4.2}$$

The time-dependent applied excitation $\ddot{u}_g$ is discretized into a serie of values $\ddot{u}_{g_i} = \ddot{u}_g(t_i)$, and the time interval, assumed to be constant, can be expressed as:

$$\Delta t_i = t_{i+1} - t_i \tag{4.3}$$

Therefore, the response is determined at the discrete time instants t_i; the values of the displacement, velocity and acceleration of the system, assumed to be know, satisfy Equation 4.1 at time t_i:

$$m\ddot{u}_i + c\dot{u}_i + (f_s)_i = -m(\ddot{u}_g)_i \tag{4.4}$$

where $(f_s)_i$ is the resisting force at time t_i, which depends on the prior history of displacement (e.g. rate-independent plasticity) and/or velocity (e.g. rate-dependent plasticity) for inelastic systems. Numerical procedures allow the estimation of the response quantities $\ddot{u}_{i+1}$, $\dot{u}_{i+1}$, u_{i+1} at the time $i+1$ that satisfy Equation 4.1 at time t_{i+1}:

$$m\ddot{u}_{i+1} + c\dot{u}_{i+1} + (f_s)_{i+1} = -m(\ddot{u}_g)_{i+1} \tag{4.5}$$

However, stepping form time i to time $i+1$ is not an exact procedure. Many approximate procedures are possible that are implemented numerically. In the present work, it has been chosen to adopt a method based on assumed variation of acceleration: the Newmark's method.

It is based on the following equations:

$$\dot{u}_{i+1} = \dot{u}_i + [(1-\gamma)\Delta t]\ddot{u}_i + (\gamma\Delta t)\ddot{u}_{i+1} \tag{4.6}$$

$$u_{i+1} = u_i + \Delta t\dot{u}_i + [(0.5-\beta)(\Delta t)^2]\ddot{u}_i + [\beta(\Delta t)^2]\ddot{u}_{i+1} \tag{4.7}$$

These two equations, combined with the equilibrium Equation 4.5 at the end of the time step, provide the basis for computing $\ddot{u}_{i+1}$, $\dot{u}_{i+1}$, u_{i+1} at time t_{i+1} for the known $\ddot{u}_i$, $\dot{u}_i$, u_i at time t_i. Iteration is required to implement these computations because the unknown appears in the right side of Equation 4.1.

In this framework, the equation of motion can be written in its incremental form:

$$m\Delta\ddot{u}_i + c\Delta\dot{u}_i + (\Delta(f_s))_i = -m(\delta\ddot{u}_g)_i \tag{4.8}$$

In Newmark's methods the solution at time t_{i+1} is determined from Equation 4.8, which is equivalent to the use of the equilibrium condition (Equation 4.5) at time t_{i+1}. Such methods are called implicit methods. The generic formulation is given by:

$$G(Y(t_i), Y(t_{i+1})) = 0 \tag{4.9}$$

With the LS-DYNA software, an explicit solver is instead used: the state of the current time t_i is enough to compute the state of the next time step t_{i+1} is used. Hence, the state t_{i+1} can efficiently be calculated, since the stress at state t_i is known, and therefore, the nodal acceleration can be derived and used to compute the next stress state. The generic formulation can be expressed as:

$$Y(t_{i+1}) = F(Y(t_i)) \tag{4.10}$$

However, in order to avoid numerical drifting during the explicit integration, the time steps must be sufficiently small. In a finite element framework, in order to ensure the stability of the solution, this is translated into the inequality condition $\Delta t \leq \Delta t_c$, where Δt_c is the so-called critical time step. Δt_c can be estimated with the Courant condition, which states that the time step must be smaller than the time it takes for a stress wave to travel through an element, and it is limited by the speed of sound. For a beam element, the Courant condition is expressed as:

$$\Delta t_c \leq \min\left\{ l_c\sqrt{\frac{\rho}{E}}, \frac{0.5l_c}{c\sqrt{3I\left[\frac{3}{12I+Al_c^2} + \frac{1}{Al_c^2}\right]}} \right\} \tag{4.11}$$

For a shell element:

$$\Delta t_c \leq l_c \sqrt{\frac{\rho}{E}} \leq \frac{l_c}{\sqrt{\frac{E}{\rho(1-\nu^2)}}} \tag{4.12}$$

where Δt_c = critical time-step;

l_c = critical lengh for beam and shell element;

ρ = volumetric mass density;

E = Young's modulus;

$c = \sqrt{\frac{\rho}{E}}$ = speed of sound through the elastic medium;

I = moment of inertia;

A = cross-sectional area;

ν = Poisson's ratio.

In equation 4.11, the first terms is related to the axial pressure, while the second to the bending vibrations.

For large complex models, a relatively small element can govern the critical time step. In fact, for a relatively fine mesh, necessary to ensure the smear cracking pattern, the critical step could be of the order of 10^{-6}, leading to a computational time of several hours for short duration input signals.

Instead, the equation of motion for the proposed macro-element is solved numerical with an implicit time-stepping integration and can be expressed in relative coordinates as:

$$\mathbf{M\ddot{u} + C\dot{u} + f_s = -M\ddot{u}_g} \tag{4.13}$$

where $\mathbf{M}$ is the mass matrix, $\mathbf{u}$ the DoF vector, $\mathbf{C}$ the damping matrix ,$\mathbf{f_s}$ the resisting force matrix and $\mathbf{\ddot{u}_g}$ the excitation vector.

In particular, the $\mathbf{f_s}$ depends of the displacement history according to the rate-independent hysteretic rules described in Section 3.4. Below, the initial stiffness contribution to the $\mathbf{f_s}$ matrix is shown. It is denoted as $\mathbf{K_{in}}$, initial stiffness matrix. The vector of the DoF is presented as well, for the fix ended boundary condition. The mass matrix formulation follows the distribution presented in Section 3.4.4. The damping matrix formulation is instead given in the next section.

$$\mathbf{K_{in}} = \begin{bmatrix} 4\frac{EI}{l}+\mu & -6\frac{EI}{l^2} & 2\frac{EI}{l} & 0 & 0 & 0 \\ -6\frac{EI}{l^2} & 12\frac{EI}{l^3}+K_s & -6\frac{EI}{l^2} & -K_s & 0 & 0 \\ 2\frac{EI}{l} & -6\frac{EI}{l^2} & 8\frac{EI}{l} & 6\frac{EI}{l^2} & -6\frac{EI}{l^2} & 2\frac{EI}{l} \\ 0 & -K_s & 6\frac{EI}{l^2} & 12\frac{EI}{l^3}+K_s & -12\frac{EI}{l^3} & 6\frac{EI}{l^2} \\ 0 & 0 & -6\frac{EI}{l^2} & -12\frac{EI}{l^3} & 12\frac{EI}{l^3} & -6\frac{EI}{l^2} \\ 0 & 0 & 2\frac{EI}{l} & 6\frac{EI}{l^3} & -6\frac{EI}{l^3} & \mu+4\frac{EI}{l} \end{bmatrix}$$

Accelerated-Newton (AN) methods strike a compromise between the Newton-Raphson (NR) and Modified-Newton (MN) methods. Generally, the compromise is to hold the stiffness matrix constant during iteration, but to use selected information from previous iterations to accelerate convergence of the MN method. Its performance in the non-linear analysis of structures is comparable to NR, requiring only a few more iterations to converge while taking less computational time than both NR and MN. The Krylov subspace based algorithm developed by Carlson and Miller (1998) accelerates the convergence of the MN iteration. The acceleration brings the rate of convergence close to that of NR at a lower computational expense.

Table 4.1: Dynamic analysis parameters

	Type
Analysis	Transient
Algorithm	Krylov-Newton [52]
Integrator	Newmark: $\beta = 0.5$ $\gamma = 0.25$
Convergence criterion	NormDispIncr: tol= 1.0E-5 iter= 800

The chosen values of β and γ for the Newmark's method corresponds to the assumption of constant average acceleration during the time-step (Figure 4.1).

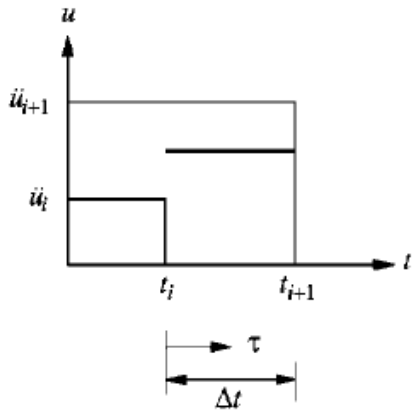

Figure 4.1: Average acceleration method [19]

4.2. Damping in NLTH analysis for earthquake excitation

In this section, the damping matrix **C** assembly is discussed along with the contribution of the hysteretic damping. In the dynamic response of inelastic systems, one may identify two sources of damping:

- Intrinsic viscous damping
- Hysteretic damping

The fraction of critical damping for a non-linear system is given by an expression of the following form:

$$\zeta_{eq} = \zeta_{eq,v} + \zeta_{eq,h} \tag{4.14}$$

where $\zeta_{eq,v}$ and $\zeta_{eq,h}$ represent energy dissipation resulting from viscous and inelastic hysteresis respectively.

Hysteretic damping is generated via the non-linear response of various materials which create hysteresis loops and dissipate energy. Intrinsic viscous damping is used to cover the other sources of damping that are not considered in the model, such as energy dissipation generated from friction and damage to non-structural components.

For linear analyses (e.g. response spectrum analysis) it is common practice to use a standard viscous damping ratio, as way to indirectly cover the contribution coming from the non-linearities of the materials.

One of the major benefits of NLTH analyses relies on the possibility of explicitly consider the material damping, so that the viscous component can be reduce to low values of $\zeta_{eq,v}$.

4.2.1. Rayleigh damping

One way to formulate the viscous damping matrix **C** is to follow the Rayleigh damping modelling approach. In this method, the damping matrix can be specified as a sum of mass and stiffness proportional terms, with two constants to be specified in terms of desired modal damping ratios. Rayleigh damping involves two components: the mass proportional component, which provides energy dissipation inversely proportional to frequency; and the stiffness-proportional component, which increases linearly with frequency.

$$\mathbf{C} = \alpha\mathbf{M} \qquad \text{and} \qquad \mathbf{C} = \beta\mathbf{K} \tag{4.15}$$

In both of the expressions, the matrix **C** is diagonal by virtue of the modal orthogonality property of the matrices **M** and **K**; therefore the Rayleigh damping formulation leads to a classical damping matrix.

Adding the two components leads to a U-shaped curve in the frequency domain, with a relatively uniform plateau in vicinity of the minimum (Figure 4.2).

$$\mathbf{c} = \alpha\mathbf{m} + \beta\mathbf{k} \tag{4.16}$$

The coefficients α and β can be determined from specified damping ratios ζ_i and ζ_j for the ith and jth modes respectively, according to the following relations:

$$\alpha = \frac{2\omega_1\omega_2(\zeta_1\omega_2 - \zeta_2\omega_1)}{\omega_2^2 - \omega_1^2} \qquad \beta = \frac{2(\zeta_2\omega_2 - \zeta_1\omega_1)}{\omega_2^2 - \omega_1^2} \tag{4.17}$$

Assuming $\omega_2 > \omega_1$, the numerator determines the sign of α and β, leading to three possible combinations:

(A) $\alpha > 0$ and $\beta > 0$ if $\frac{\omega_1}{\omega_2} < \frac{\zeta_2}{\zeta_1} < \frac{\omega_2}{\omega_1}$

(B) $\alpha > 0$ and $\beta \leq 0$ if $\frac{\zeta_2}{\zeta_1} \leq \frac{\omega_1}{\omega_2}$

(C) $\alpha \leq 0$ and $\beta > 0$ if $\frac{\zeta_2}{\zeta_1} \geq \frac{\omega_2}{\omega_1}$

If the coefficient are known, the damping ratio ζ_i for any other principal mode can be expressed as:

$$\zeta_i = \frac{\alpha}{2\omega_i} + \frac{\beta}{2}\omega_i \tag{4.18}$$

In the figure below, the relation is illustrated for the three cases.

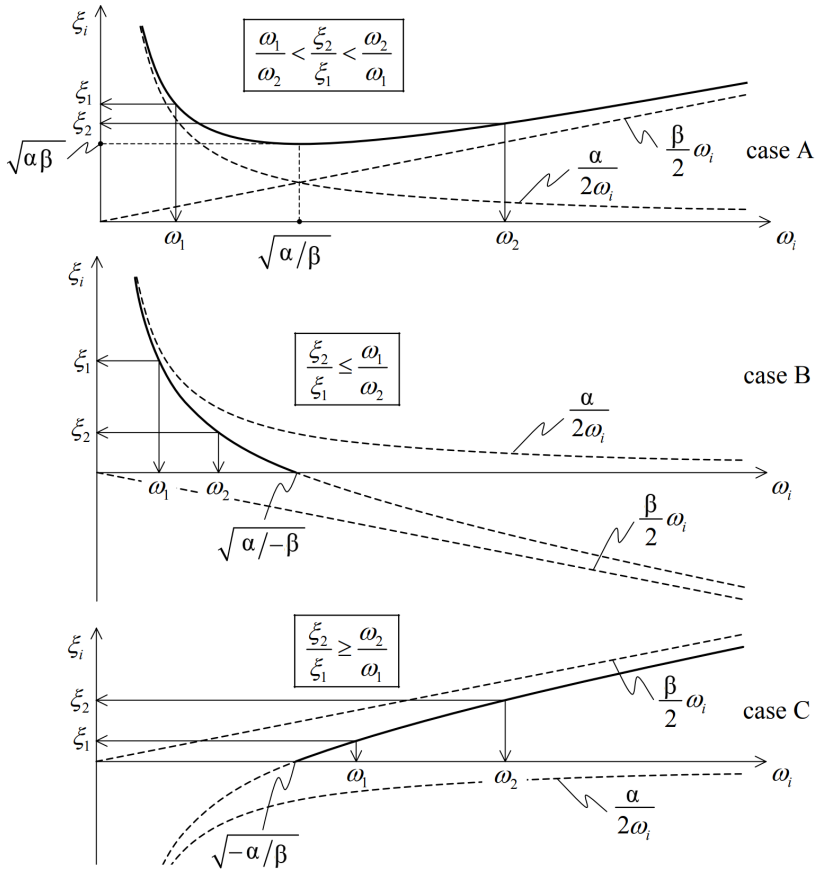

Figure 4.2: Variation of modal damping rations with natural frequency [19]

In case A, all values of ζ_i are positive. In case B, the damping ratio ζ_i becomes negative for natural frequencies $\omega_i > \sqrt{\alpha/-\beta}$, which is unacceptable on physical ground. In case C, the damping ratio ζ_i becomes negative for natural frequencies $\omega_i < \sqrt{-\alpha/\beta}$, which is unacceptable on physical ground.

However, based on experimental data [19], it is reasonable to assume that same damping ratio for the two modes, leading to the following relations:

$$\alpha = \zeta \frac{2\omega_i \omega_j}{\omega_i + \omega_j} \qquad \beta = \zeta \frac{2}{\omega_i + \omega_j} \tag{4.19}$$

In such case, for any combination of natural frequencies, the damping ratio ζ_i given by equation 4.18 is positive. However, for natural frequencies $\omega_1 < \omega < \omega_2$, ζ_i is lower than the specified ζ. For natural frequencies $\omega > \omega_2$ and $\omega < \omega_1$, the damping ratio is higher than the specified ζ.

The stiffness proportional part of Rayleigh corresponds physically to linear viscous dampers that interconnect the degrees of freedom of a structure. In a non-linear analysis where the non-linearity is of the softening type, limits on the restoring forces are imposed by various mechanics such as yielding, cracking, sliding and buckling. If the initial linear stiffness matrix is employed to construct the stiffness-proportional damping terms, then the damping forces in a softening element can reach unrealistically high values compared to element restoring forces. However, since the initial stiffness of the structure is used in forming the motion equation, the calculated damping is overestimated. The linearity assumption on the damping forces means they are always proportional to the velocities, no matter how large they become [6].

Therefore, the Rayleigh damping model, which is pervasive in non-linear response history analysis of building, is shown to develop 'spurious' damping forces and lead to inaccurate response results with lumped plasticity models [20]. Replacing the stiffness-proportional part of Rayleigh damping by the tangent stiffness matrix is shown to improve response results. In such case, the damping matrix can be formulated as follows:

$$\mathbf{c} = \alpha \mathbf{m} + \beta \mathbf{k_t} \tag{4.20}$$

where $\mathbf{k_t}$ is the tangent stiffness matrix, and is updated at each time step during the numerical integration of the equation of motion (e.g. Equation 4.8). However, this model is not recommended because it lacks a physical basis and has conceptual implications that are troubling: hysteresis in damping force-velocity relationship and negative damping at large displacements. Furthermore, the model conflicts with the constant-damping model that has been the basis for fundamental concepts and accumulated experience about the inelastic response of structures.

4.2.2. Caughey damping

An alternative method is available for assembling the damping matrix associated with any given set of modal damping ratios [21]. This is shown to eliminate the 'spurious' forces and it is the recommended damping model for NLTH analysis [20]. Assuming that the damping matrix $\mathbf{c}$ is built up such that the eigenvectors possess the characteristic of orthogonality with respect to it, the modal damping matrix $\mathbf{C}$ is forced to be a diagonal matrix. Hence, the modal diagonal matrix of generalized damping coefficients is given by pre- and post-multiplying the damping matrix by the mode-shape matrix:

$$\mathbf{C} = \Phi^T \mathbf{c} \Phi = 2 \begin{bmatrix} \zeta_1 \omega_1 M_1 & 0 & 0 & \cdots \\ 0 & \zeta_2 \omega_2 M_2 & 0 & \cdots \\ 0 & 0 & \zeta_3 \omega_3 M_3 & \vdots \\ \vdots & \vdots & \vdots & \vdots \end{bmatrix} \tag{4.21}$$

One may notice that the damping matrix $\mathbf{c}$ can be obtained by pre- and post-multiplying modal damping matrix $\mathbf{C}$ by the inverse of the transposed mode-shape matrix and the inverse of the mode-shape matrix, respectively, resulting in the following equality:

$$[\Phi^T]^{-1} \mathbf{C} \Phi^T = [\Phi^T]^{-1} \Phi^T \mathbf{c} \Phi \Phi^{-1} = \mathbf{c} \tag{4.22}$$

However, inverting the mode-shape matrix requires a large computational effort. Hence, making use of the orthogonality property of the mode shapes relatively to the mass matrix, one may obtain:

$$\mathbf{M} = \Phi^T \mathbf{m} \Phi \tag{4.23}$$

$$\mathbf{I} = \mathbf{M}^{-1}\mathbf{M} = [\mathbf{M}^{-1}\Phi^T\mathbf{m}]\Phi = \Phi^{-1}\Phi \tag{4.24}$$

From Equation 4.24, it is evident that:

$$[\Phi^T]^{-1} = \mathbf{m}\Phi\mathbf{M}^{-1} \tag{4.25}$$

Substituting the last expression into Equation 4.22, one may obtain:

$$\mathbf{c} = [\mathbf{m}\Phi\mathbf{M}^{-1}]\mathbf{C}[\mathbf{M}^{-1}\Phi^T\mathbf{m}] \tag{4.26}$$

Since matrix **C** is diagonal and contains elements $C_n = 2\zeta_n\omega_n M_n$, the elements of the diagonal matrix **c** can be obtained from the product of the three central diagonal matrices, resulting into:

$$d_n = \frac{2\zeta_n\omega_n}{M_n} \tag{4.27}$$

In such way, the Equation 4.22 may be written as:

$$\mathbf{c} = \mathbf{m}\Phi\mathbf{d}\Phi^T\mathbf{m} \tag{4.28}$$

where **d** is the diagonal matrix containing the elements d_n. In this framework, each modal damping ratio provides an independent contribution to the damping matrix:

$$\mathbf{c}_n = \mathbf{m}\Phi_n d_n \Phi_n^T\mathbf{m} \tag{4.29}$$

Therefore, the total damping matrix is obtained by the sum of the modal contributions:

$$\mathbf{c} = \sum_{n=1}^{N}\mathbf{c}_n = \mathbf{m}\Big[\sum_{n=1}^{N}\Phi_n\mathbf{d}_n\Phi_n^T\Big]\mathbf{m} \tag{4.30}$$

The nth term in this summation is the contribution of the nth mode with its damping ratio ζ_n to the damping matrix **c**; if it is not included, the resulting **c** implies zero damping ration in the nth mode.

In the figure below, a comparison between the three damping models described above is presented. It is the time history drift of the top node of the macro-element subjected to a low intensity acceleration signal.

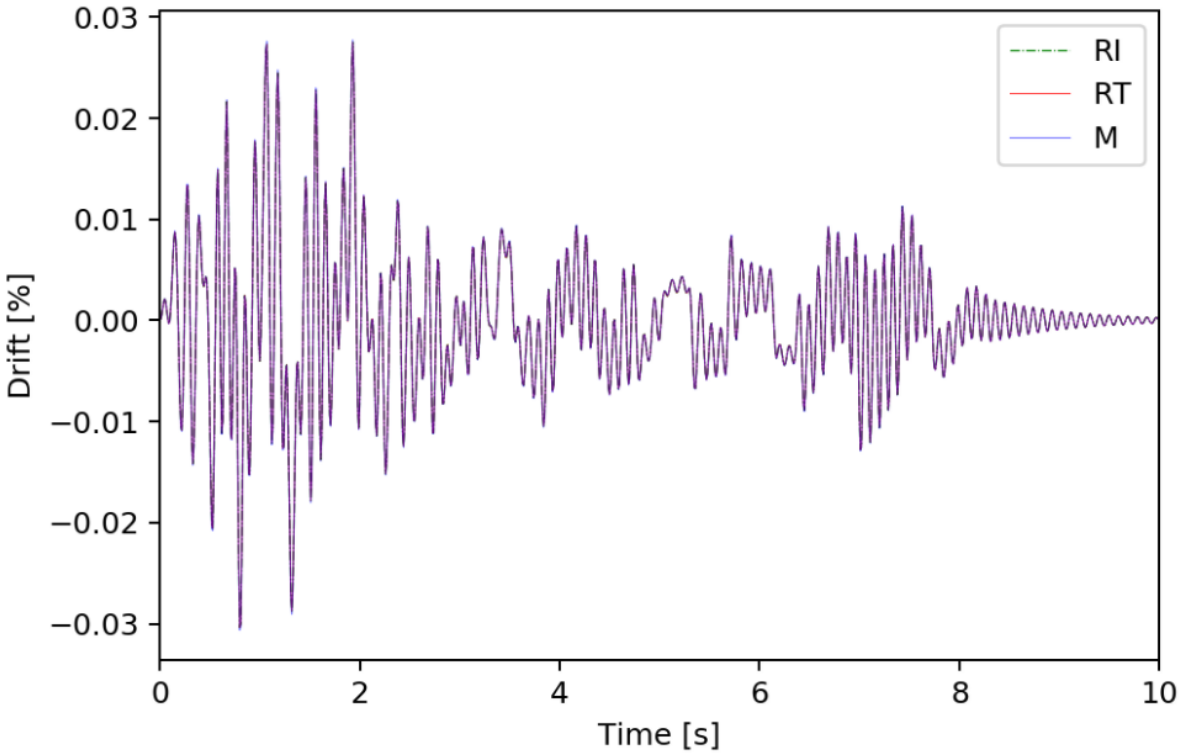

Figure 4.3: Drift history comparison with damping matrix formulated with the initial stiffness Rayleigh model (RI), tangent stiffness Rayleigh model (RT) and the Caughey or modal damping model (M) - Linear response

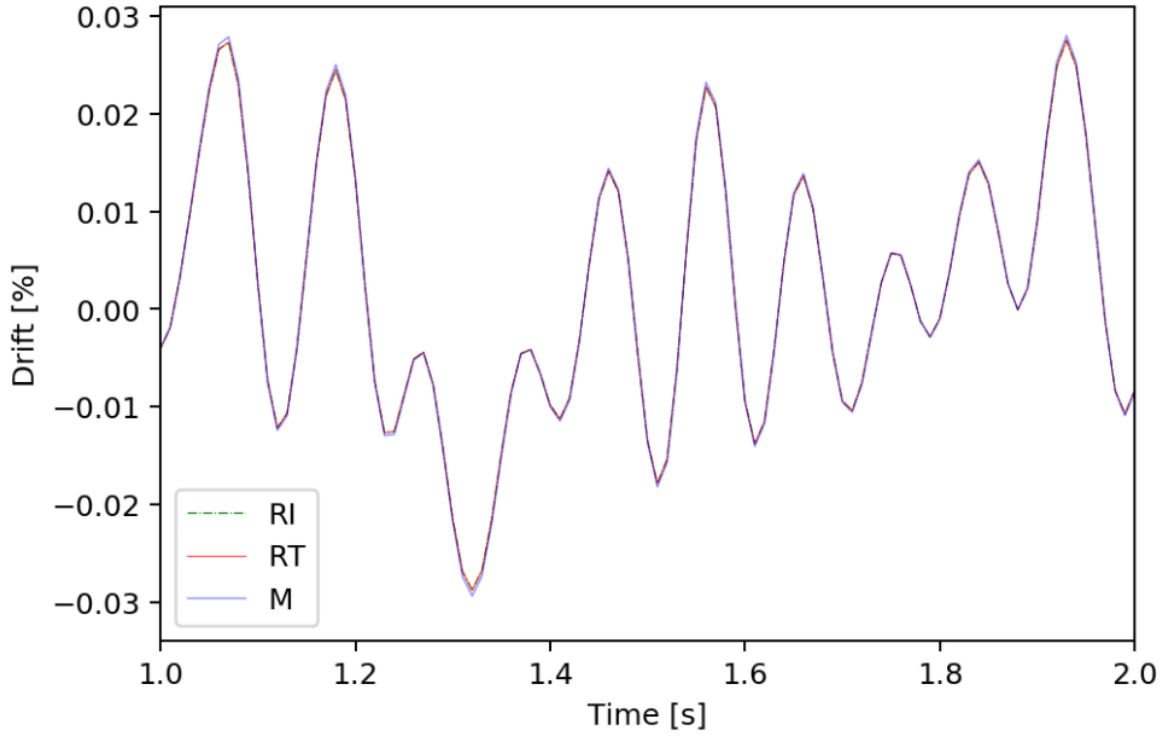

Figure 4.4: Peak drift comparison in the linear range

The differences in the three damping models have essentially no effect on the structural responses to a scaled-down version of a GM record, as presented in Figure 4.3 and 4.4. The peak displacements are unaf-

fected by the damping model if the structure does not yield.

The high-intensity record drives the system into the inelastic range, and its response is influenced by the choice of the damping model.

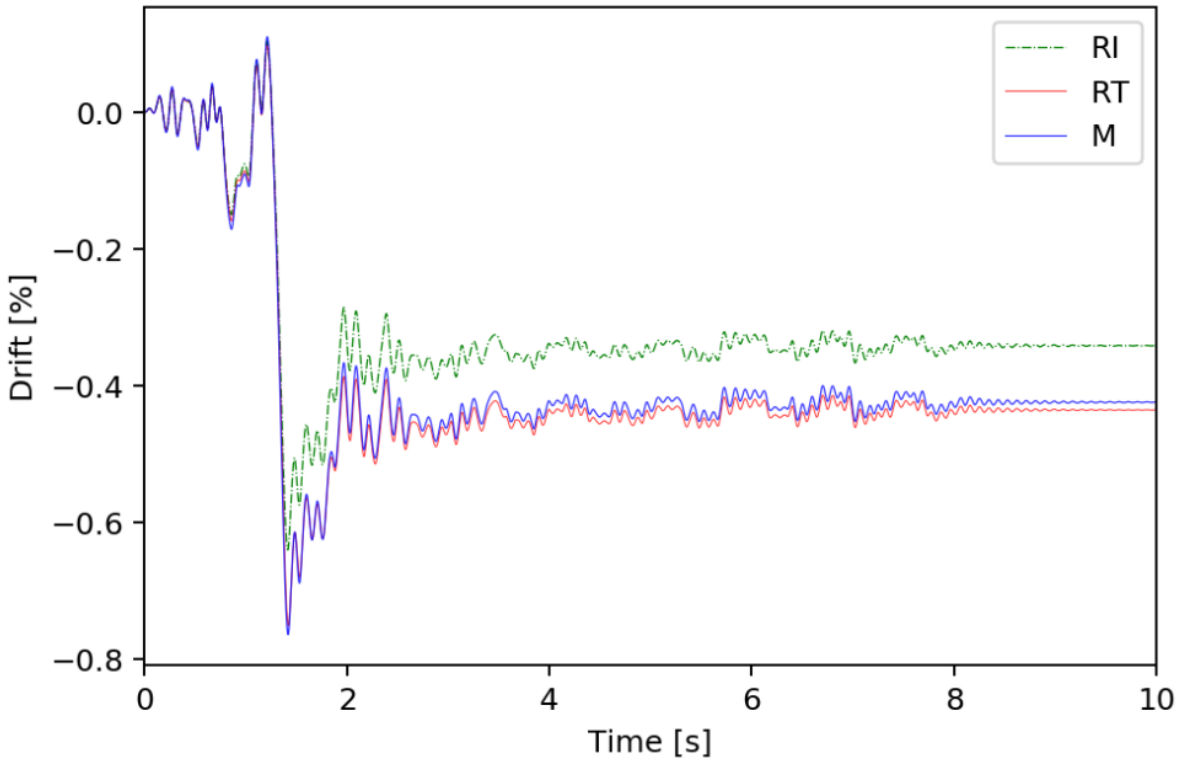

Figure 4.5: Initial vs tangent-stiffness proportional damping in the shear response

This is evident from Figure 4.5. The RI model leads to the least conservative results. As mentioned above, at yielding, the damping forces are unrealistically high and this results into a smaller peak displacement and consequently a smaller residual drift in the system. This outcome is in agreement also with the study on SDoF inelastic systems presented in [30]. The RT model leads to results that display the right trends. However, for the reasons described above, the Caughey damping model is favourable approach for NLTH of URM structures.

4.2.3. Harmonic vibrations

A benchmark study is carried out as way to assess if the smeared plasticity model and the macro-element model exhibit a comparable equivalent damping ratio. The viscous damping and the hysteretic damping contributions are compared. Firstly, $\zeta_{eq,v}$ can be estimated by from the damped-vibration response for the system undergoing freely decaying vibration as presented in Figure 4.6).

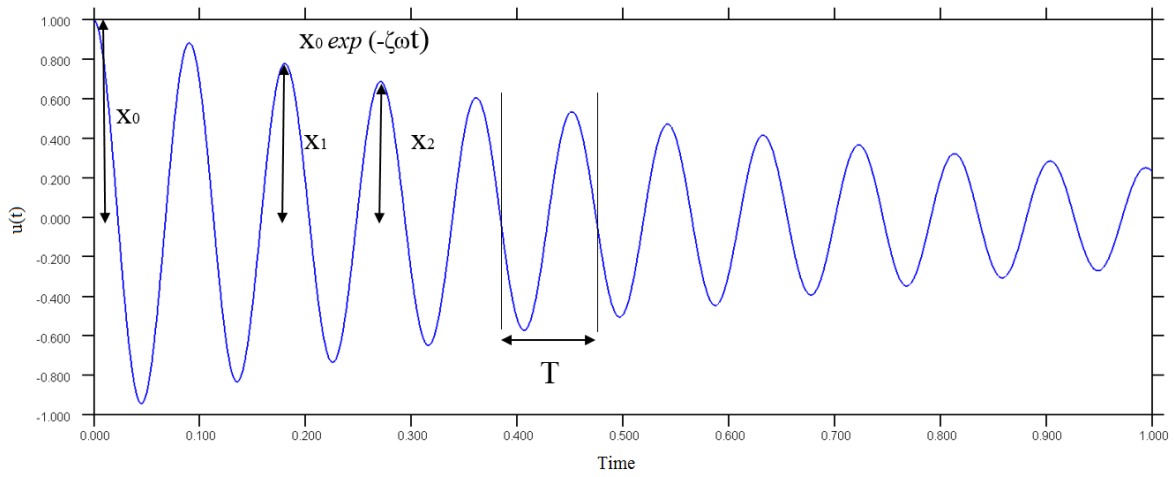

Figure 4.6: Damped-vibration curve for a visco-elastic system undergoing freely decaying vibration

By measuring δ, the natural logarithm of the ratio of two successive amplitudes of damped free oscillations, one may determine the decay constant related to the viscous damping ratio for the system.

$$\zeta_{eq,v} = \frac{\delta}{\sqrt{(2\pi)^2 + \delta^2}} \qquad \delta = \ln\left(\frac{x_1}{x_2}\right) \tag{4.31}$$

Both the shell element model and the macro-element are in good agreement, with approximately 2% viscous damping ratio in the linear range of vibrations.

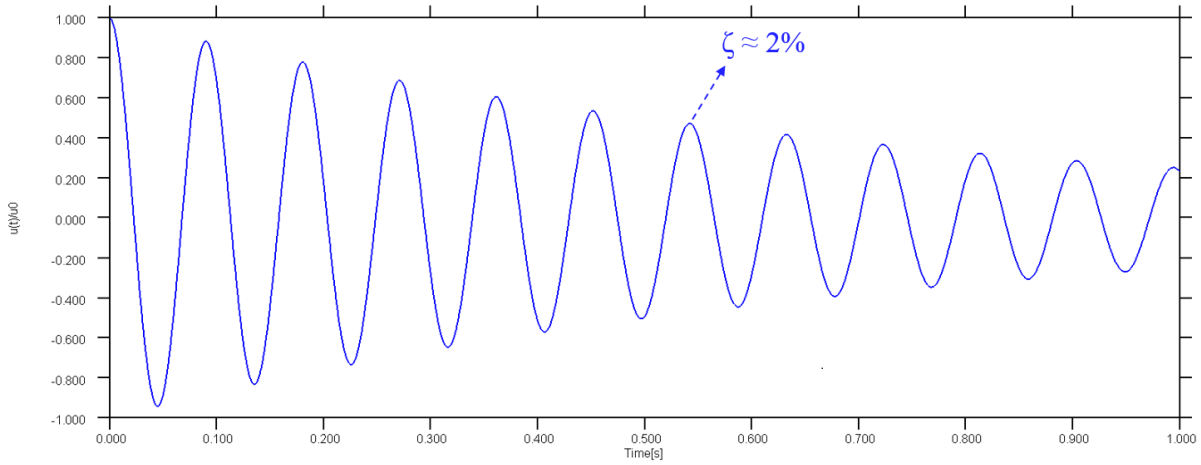

Figure 4.7: Normalised response for the macro-element model undergoing freely decaying vibration

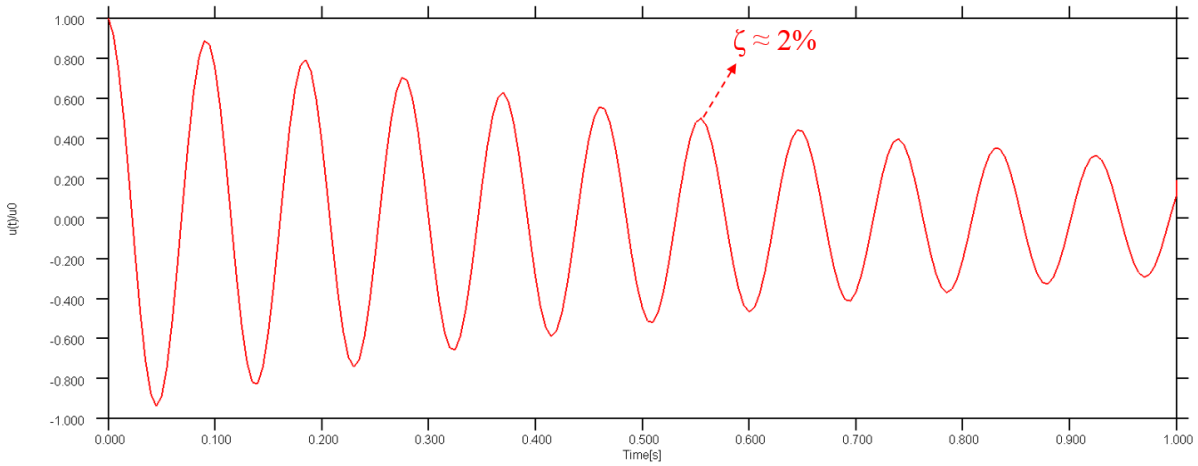

Figure 4.8: Normalised response for the shell element model undergoing freely decaying vibration

4.2.4. Energy dissipation

In addition, the hysteretic equivalent portion of damping is compared for the two systems. In order to understand its contribution, the equation of motion for a damped SDoF system subjected to an earthquake record is given:

$$m\ddot{u} + c\dot{u} + f_s = -m\ddot{u}_g \tag{4.32}$$

where $\ddot{u}_g$ is the ground acceleration and u, $\dot{u}$, $\ddot{u}$ are the relative displacement, velocity and acceleration, respectively, with respect to the ground. The absorbed energy is evaluated according to the energy balance equation, derived from integrating over time the equation of motion, representing the equilibrium of forces, multiplied by the instantaneous displacement $du = \dot{u}d\tau$:

$$\int_0^t m\ddot{u}\dot{u}d\tau + \int_0^t c\dot{u}\dot{u}d\tau + \int_0^t f_s\dot{u}d\tau = -\int_0^t m\ddot{u}_g\dot{u}d\tau \tag{4.33}$$

The first term depicts the relative kinetic energy of the system, as measured with respect to the ground, representing energy temporarily stored in the kinematics of the system. The second is the damping energy dissipated by viscous damping, and the third is termed the absorbed energy, consisting of the irrecoverable hysteretic energy and the recoverable strain energy. The right-hand-side term is the relative input energy imparted by the ground motion to the system, as measured relative to the ground, excluding any rigid body translation.

The hysteretic energy, absorbed by a structural system during a seismic event that is strong enough to induce a certain amount of non-linearity to the system, has been recognized by several researchers as a potentially useful seismic performance indicator [7]. In the absorbed energy history $E(t)$, the parameter t may be the real time or an ordering parameter (pseudo-time) for quasi-static analyses. $E(t)$ is defined starting from the force and displacement histories recorded during the laboratory test, $F(t)$ and $\delta(t)$ respectively, as:

$$E(t) = \int_0^{\delta(t)} F(\delta(t))d\delta = \int_0^t F(\tau)\frac{d\delta}{d\tau}d\tau \tag{4.34}$$

In general, stable hysteretic loops with large energy dissipation capacity at a member level are thought to guarantee a better deformation performance of the system, implying that there is a good correlation between the dissipated hysteretic energy and the inelastic deformation demands. This notion is often linked to quasi-static cyclic test results, where it seems apparent that between two systems with similar strength, tested under the same cyclic loading protocol, the one with the higher energy absorption (i.e. larger hysteresis loops) should exhibit superior performance.

The absorbed energy is linked to the equivalent inelastic damping ratio, also know as loss factor, and it is defined as [19]:

$$\zeta_{eq,h} = \frac{1}{4\pi}\frac{E_D}{E_{s_0}} \tag{4.35}$$

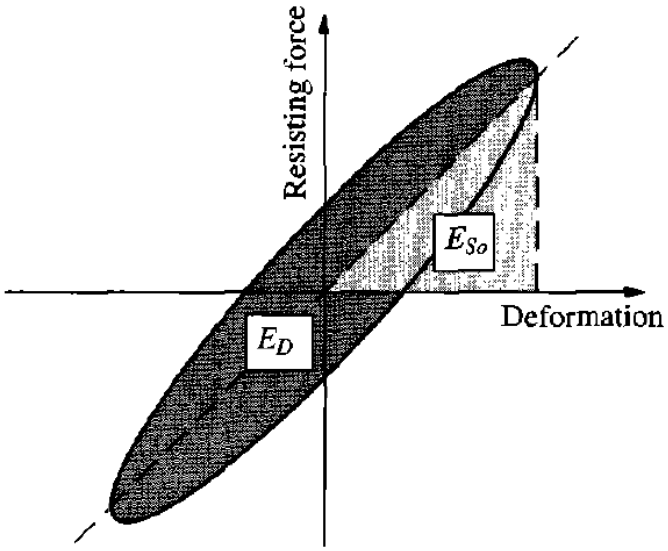

Figure 4.9: Definition of energy loss E_D in a cycle and maximum strain energy E_{s_0} [19]

The $\zeta_{eq,h}$ for the two tests presented in Section 3.4.2 and 3.4.3 is hence computed, as way to evaluate the matching between the modelling approaches, as well as to estimate the amount of hysteretic damping provided by the shear and the rocking behaviour of URM components.

In the figures below, the force-displacement curves of the squat pier component are presented both for laboratory test and the macro-element analysis. The reference cycle for the damping ratio estimation is included in red. The third cycle after the system moves into the inelastic range is adopted, as suggested in [44]. It is likely to be representative of the full inelastic behaviour, since in the considered tests no damage is observed. In addition, no damage parameters are included in the hysteretic law proposed for the macro-element. However, in case of damage-based constitutive rules, it is expected to observe an evolution of the hysteretic damping ratio under cyclic loading.

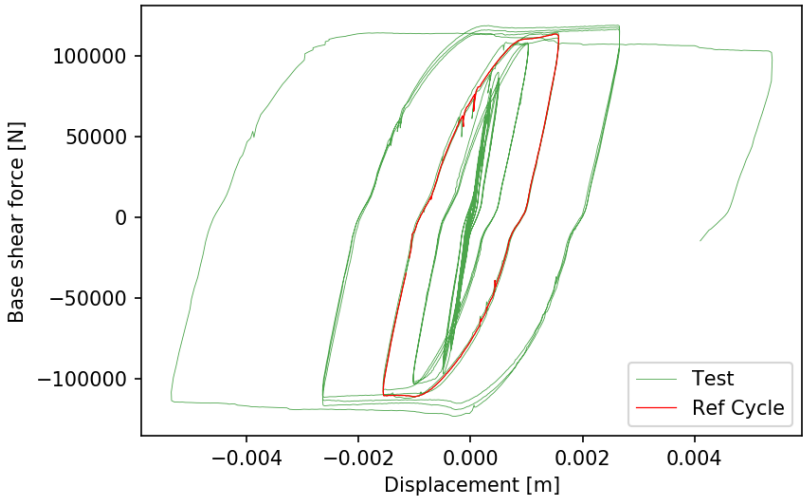

Figure 4.10: Reference cycle for energy loss calculation

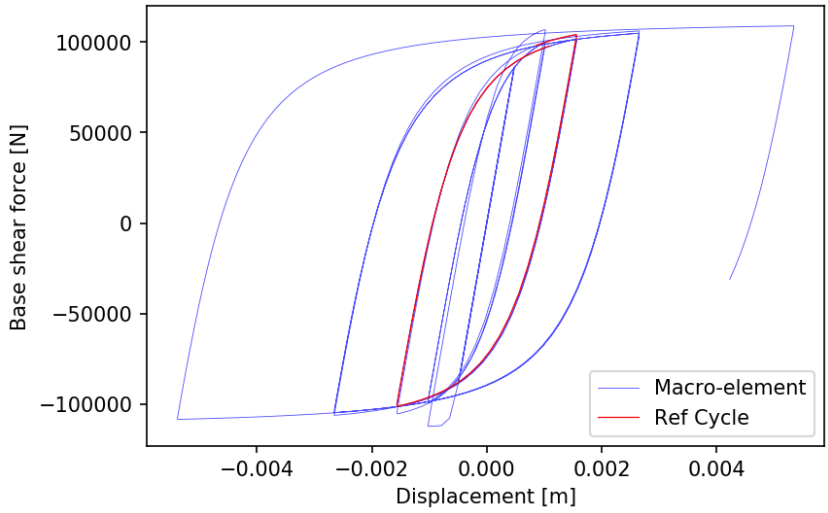

Figure 4.11: Reference cycle for energy loss calculation

Table 4.2: Equivalent hysteretic damping ratio comparison for the squat component

System	$\zeta_{eq,h}$ [%]
Laboratory test	30.4
Macro-element	32.5

It can be noticed that the shear hysteretic model matches well the lab test results, resulting in only 6% difference for the Laboratory. Indeed, the energy dissipated by the system presented in Figure 3.28 shows a good match. It is important to highlight also that the shear mechanisms are quite dissipative, involving large sliding along mortar bed-joints.

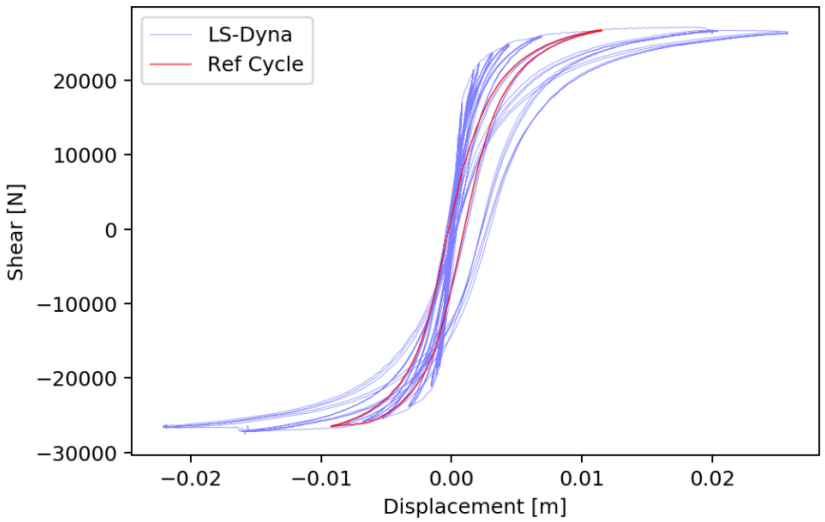

Figure 4.12: Reference cycle for energy loss calculation

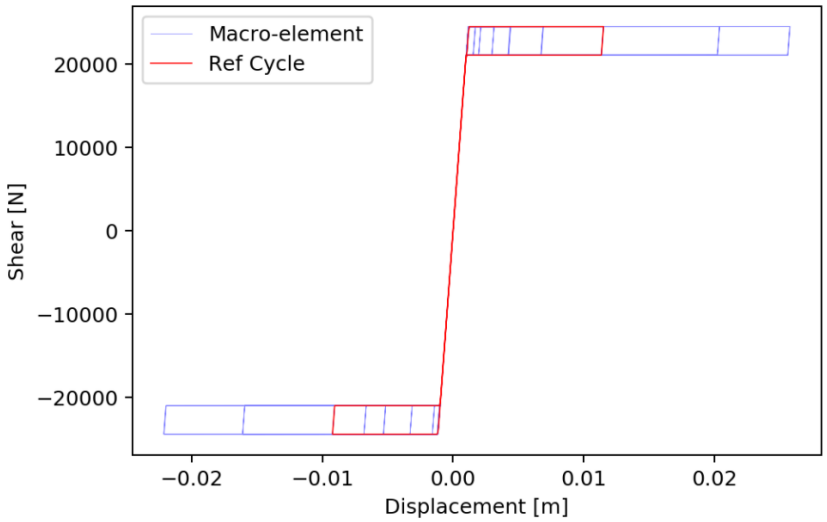

Figure 4.13: Reference cycle for energy loss calculation

Table 4.3: Equivalent hysteretic damping ratio comparison for a slender component

System	$\zeta_{eq,h}$ [%]
LS-DYNA	3.5
Macro-element	3.7

It can be noticed that the rocking hysteretic model matches well the laboratory test results, resulting in only 5% difference. Indeed, the energy dissipated by the system presented in Figure 3.17 shows a good match. It is important to highlight also that the rocking mechanism, theoretically consisting in a rigid body motion, is unable to dissipate energy. The behaviour could be modelled with the non-linear elastic presented in Figure 4.14 [46].

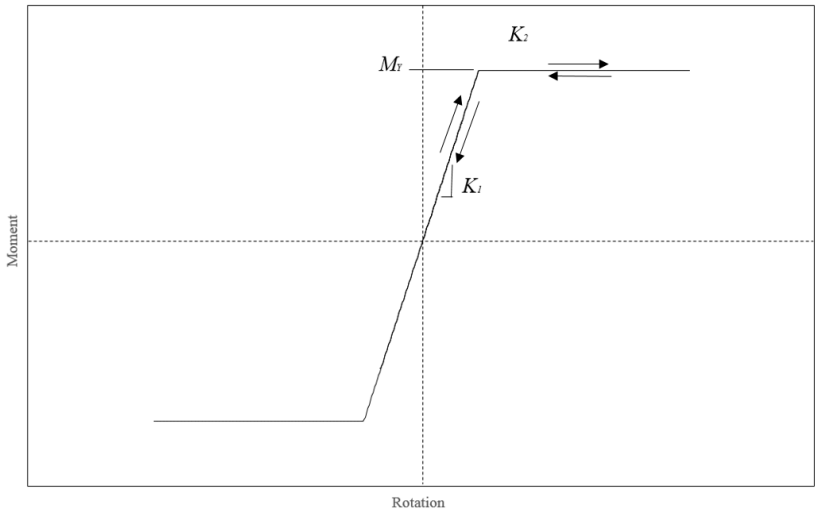

Figure 4.14: Non-linear elastic model idealization for rocking motion of walls.

5

In-plane Dynamic Test on URM Wall Piers

In this chapter, the proposed lumped plasticity macro-element approach is validated against two dynamics test performed with the software LS-DYNA: a slender URM wall component with fix-fix boundary condition, and a squat URM wall component with cantilever boundary condition. The results are compared in terms of displacement history, base shear force history and computational cost. A point cloud analysis is performed to assess the response with different input signals. The specimen geometries are the same as the laboratory component tests presented in Chapter 3. Analogously, the overburden mass is selected to induce a compression state comparable to laboratory component tests. In the table below, the calcium silicate (CaSi) masonry material properties adopted for the analyses are presented.

Table 5.1: Masonry material properties: Calcium Silicate post-1960

	Measured Properties
Young's Modulus	3.5E3 MPa
Compressive strength	7.0 MPa
Poisson's ratio	0.2
Bed-joint shear strength	0.25 MPa
Diagonal-tension strength	0.1 MPa
Bed-joint friction coefficient	0.45

5.1. In-plane dynamic test of a fix-fix slender wall

A NLTH analysis is performed on a slender masonry wall with fix-fix condition. The two systems are subjected to the same earthquake acceleration history at the bottom nodes of the system, Earthquake Record 0 (Figure B.1 in Appendix B). Seismometer-related effects may be observed in the post-peak part of the earthquake record, due to the electronic recording procedure. This phenomenon is assumed not to affect the time-history response of the systems since corresponds to the low intensity range of input accelerations.

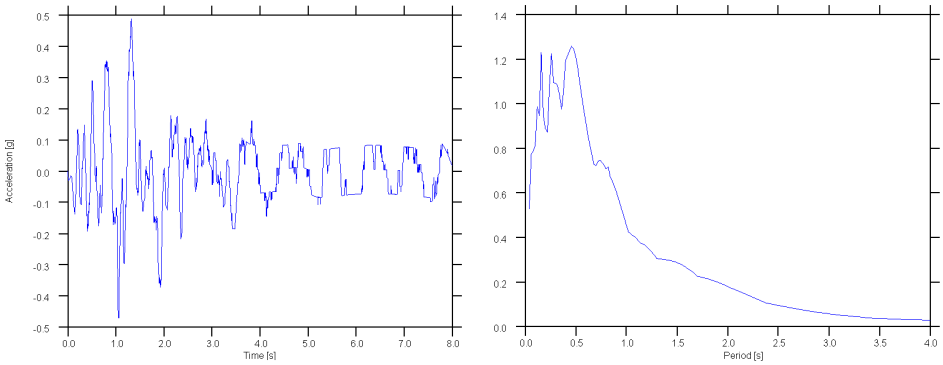

Figure 5.1: Input record and 5%-damping response spectrum

The geometry of the system is described in Table 5.2. An overburden mass is placed at the top nodes, to simulate the inertia coming from an eventual upper floor.

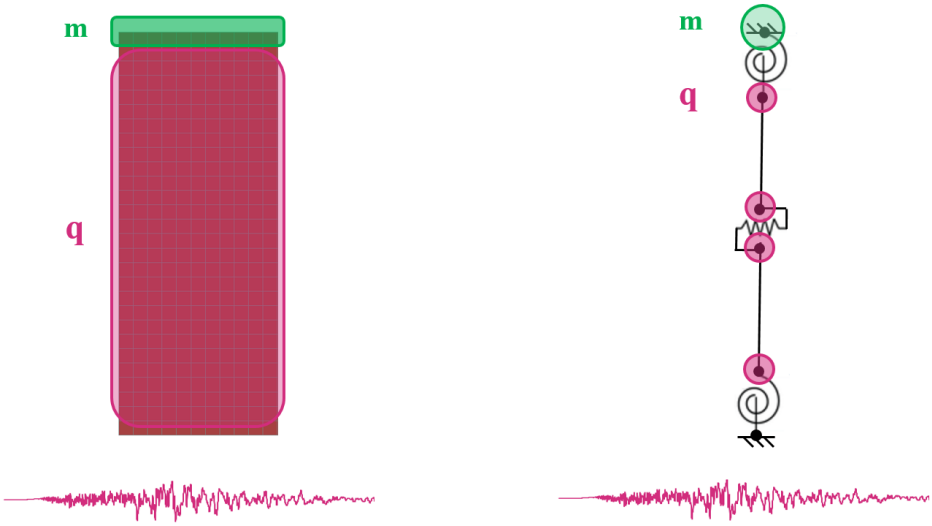

Figure 5.2: In-plane dynamic test of a slender wall

Table 5.2: Geometry of the system

	Dimension
Thickness	0.1 m
Height	2.7 m
Length	1.1 m
Boundary condition	Fix-Fix
Overburden mass	3 ton
Natural frequency	68.1 rad/s

The earthquake record was scaled with a factor corresponding to a PGA level of $0.5g$ in order to induce the development of the rocking mechanism.

5.1.1. Results

The outcomes in terms of failure mechanism, displacement and base shear force history are compared for the two modelling approaches. In particular, the same failure mechanism is predicted by both: it is a flexural mechanism which entails rocking of the system and gap opening at the two ends of the wall. The crack width predicted by LS-DYNA is up to 2.3 mm. In the case of the macro-element, only the non-linearity of the rotational springs is activated, while the shear spring remains in the linear range of deformation.

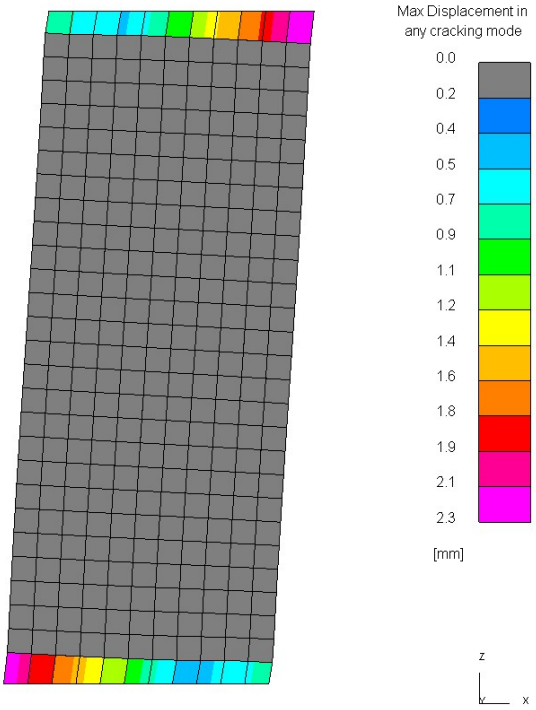

Figure 5.3: Failure mechanism - LS-DYNA - Slender component

The displacement history comparison is presented in Figure 5.4. One may notice that the period of vibration of the two system is fairly close both in the linear and non-linear range. The absolute peak displacement is not similar. One may notice that the shell element model starts deforming inelastically earlier than the macro-element model. Around 1 second in the time-history response, the period of LS-DYNA is twice as the macro-element one, which is still in the liner range. This is likely to be related to the sharp change between the elastic and post-yielding branch of the lumped plasticity model. The LS-DYNA model instead smoothly moves into the non-linear range. This is reflected in the internal energy history described in Section 5.3.1 (Figure 3.17). Furthermore, such a difference leads to a small shifting in the time-history response between the two models. The relative displacement between the positive and the negative peaks is similar, proving that effecting mass in the large non-liner range is comparable. Zero residual displacement at the end of the analyses is predicted by the two systems. This is related to the self-centering nature of rocking systems. Unless large displacements (P-Delta effect) lead to the complete wall overturning, the self and overburden weight of the wall brings it in it un-deformed position.

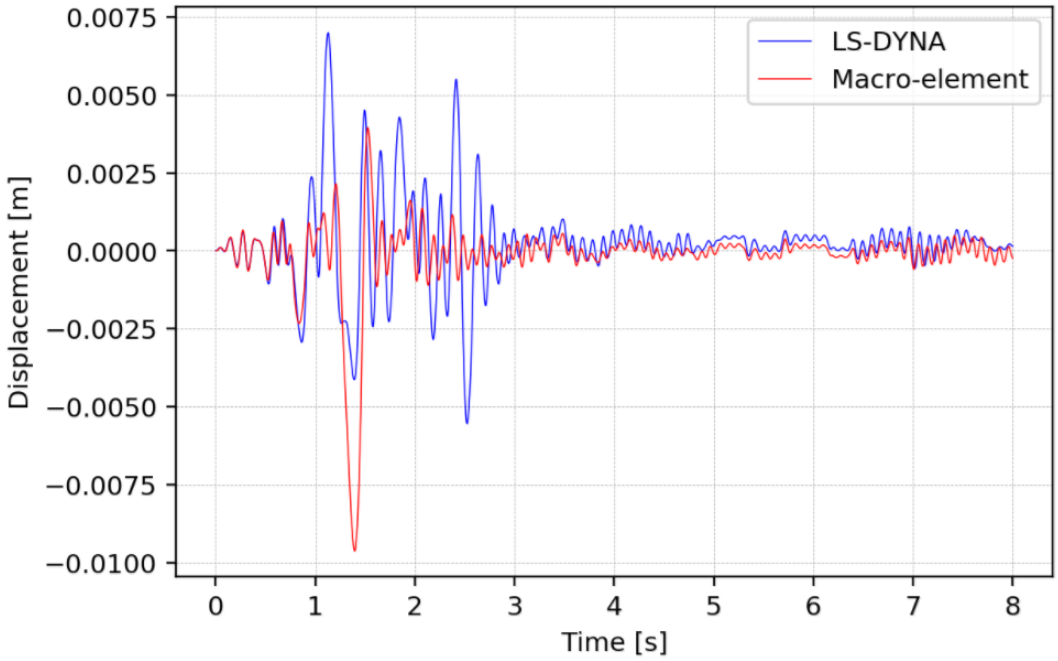

Figure 5.4: Displacement history comparison - Slender component

The base shear history plot shows a good agreement between the two approaches, both in the linear and non-linear range. The capacity of the pier component is around 12 kN.

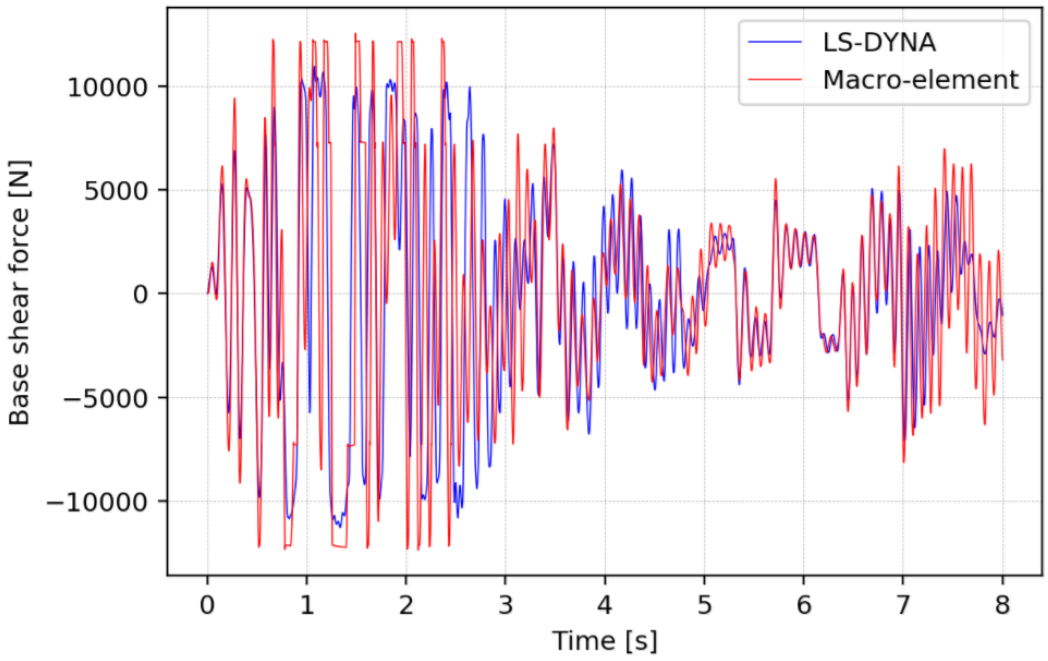

Figure 5.5: Base shear force history - Slender component

5.2. In-plane dynamic test of a cantilever squat wall

A time history analysis is performed on a squat CaSI URM wall, modelled with shell elements and with the macro-element approach. The geometry of the system is described in Table 5.3. Also in this case, an overburden mass is placed at the top nodes, to simulate the inertia coming from an eventual upper floor.

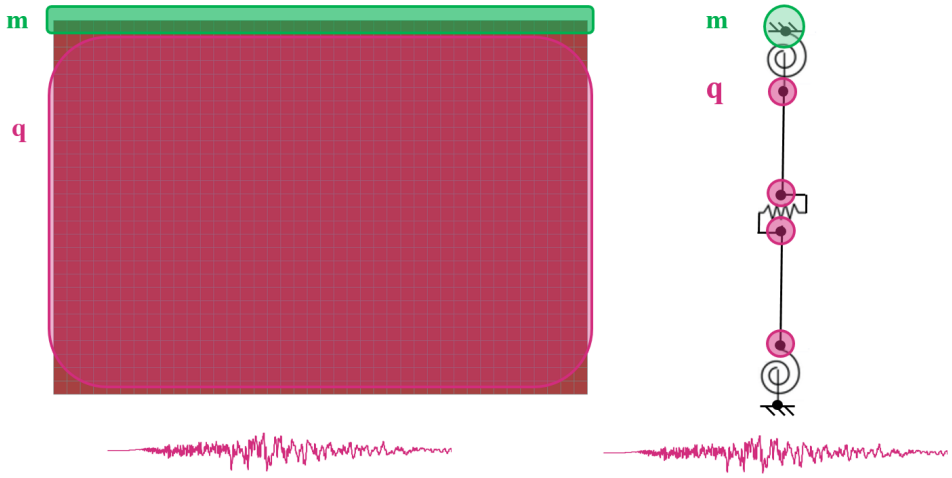

Figure 5.6: In-plane dynamic test of a squat wall

Table 5.3: Geometry of the system

	Dimension
Thickness	0.1 m
Height	2.7 m
Length	4.0 m
Boundary condition	Cantilever
Overburden mass	25 ton
Natural frequency	68.5 rad/s

The earthquake record was scaled with a factor corresponding to a PGA level of 0.5g.

5.2.1. Results

The outcomes in terms of failure mechanism, displacement and base shear force history are compared for the two modelling approaches. Diagonal cracking along head- and bed-joints is predicted by the LS-DYNA numerical simulation. The crack width at the end of the analysis is up to 3.0 mm. In the macro-element assembly, the shear spring deforms inelastically, while the rotational springs vibrate linearly

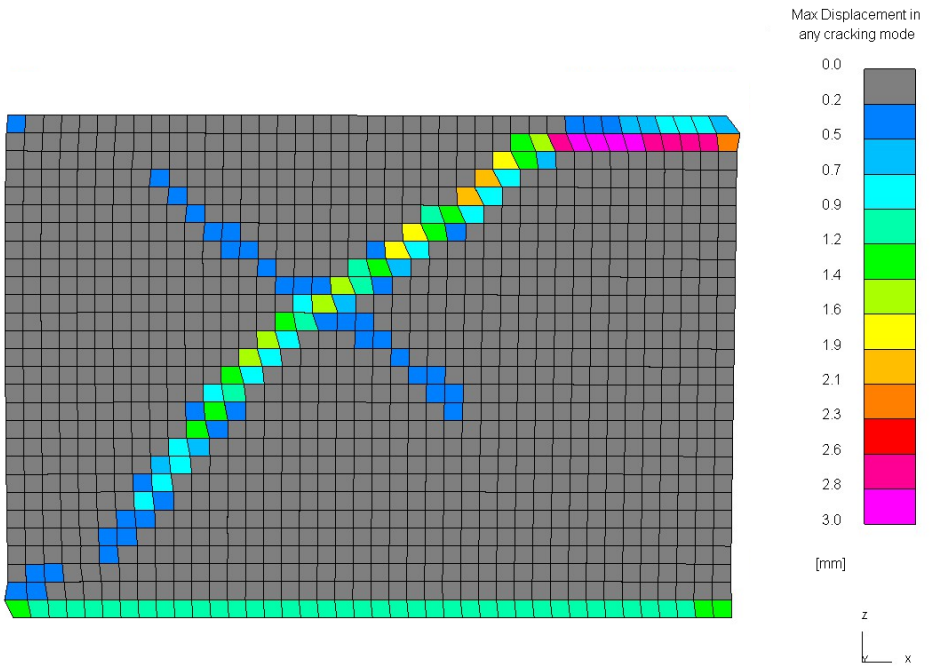

Figure 5.7: Failure mechanism - LS-DYNA - Squat component

The displacement history is presented in Figure 5.8. One may notice that the period of vibration of the two system is fairly close both in the linear and non-linear range. The absolute peak displacement match between the two, while the one in the positive direction is slightly underestimated by the macro-element. Finally, the residual displacement at the end of the analysis results in less than 1 mm difference between LS-DYNA and the macro-element, which is on the conservative side.

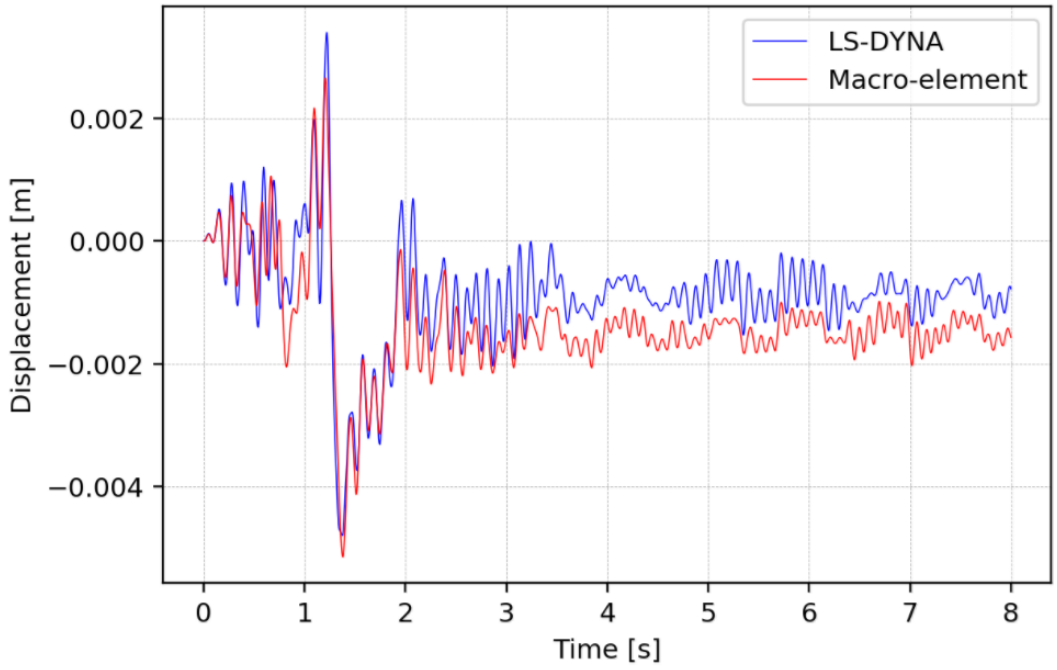

Figure 5.8: Displacement history

The base shear plot shows a good agreement in terms of capacity between the two models, a part from localised high-frequency spikes in the shell model output. This phenomenon is further described in Section 5.3.2.

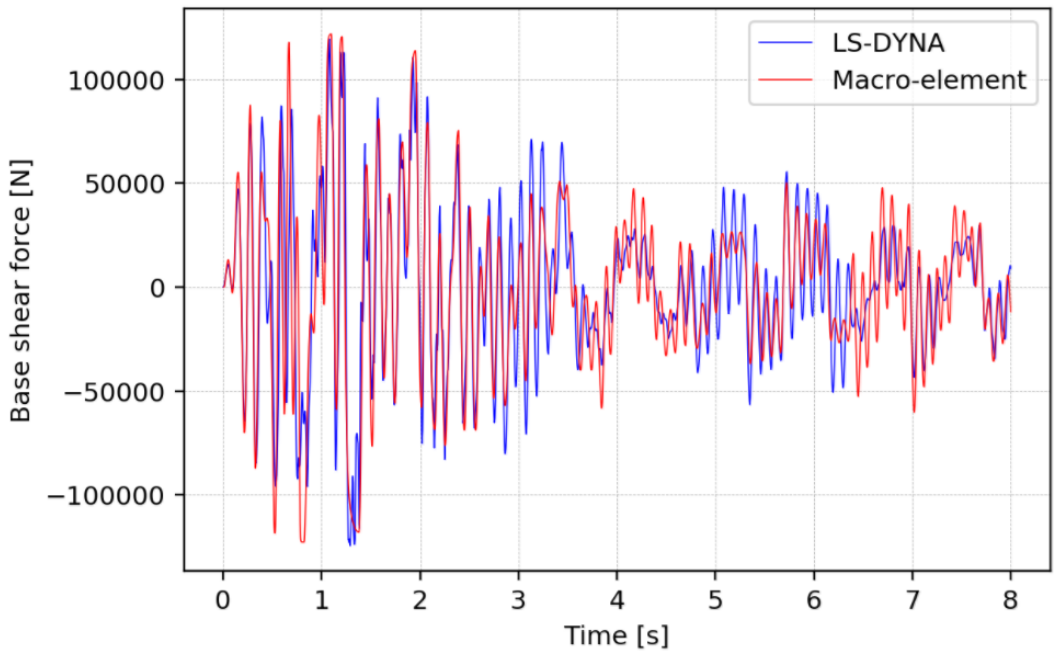

Figure 5.9: Shear history

5.2.2. Computational cost

It is worth to compare the computational cost of the two analyses. Clearly, the high-fidelity output achieved by the LS-DYNA (e.g. stress concentration, cracking pattern) cannot be reached with the lumped-plasticity model. However, the latter is more than 20 times computationally more efficient (notice also the different CPU number), this possibly allows different sensitivity studies for the same wall geometry, and proves its suitability in a fragility-curves development framework.

Table 5.4: Computational cost comparison for example presented in Section 5.2

	LS-DYNA	OpenSees
Elements	1120	5
DoF's	3444	8
CPU	10	1
Analysis time	447 s	20 s

5.3. Point cloud

It is clear that the time-history response of a non-linear system is very much dependent on characteristics of the excitation (intensity, duration, frequency content), the ground acceleration history in the present case. Hence, an essential way to assess the applicability of the simplified model is to apply different GM signals to cover the range of frequencies the system might experience and PGA measures. NLTH anlyses are performed using 10 different records, with PGA from $0.20g$ to $0.70g$, in steps of $0.02g$, with a total number of 250 runs. Analogously to the previous section, the macro-element model is validated for both a squat and a slender geometry.

5.3.1. Slender component

The wall description is presented in Table 5.2. Regarding LS-DYNA, the analyses are performed with massively parallel processing (MPP), which allows to run the solver over a cluster of machines. The macro-element approach analyses are instead run with a single CPU. The maximum drift for each GM vs the PGA level is plotted in the figure below. A drift limit value corresponding to the near collapse limit state is calculated with the expression given in Table 2.1, for elements governed by flexure.

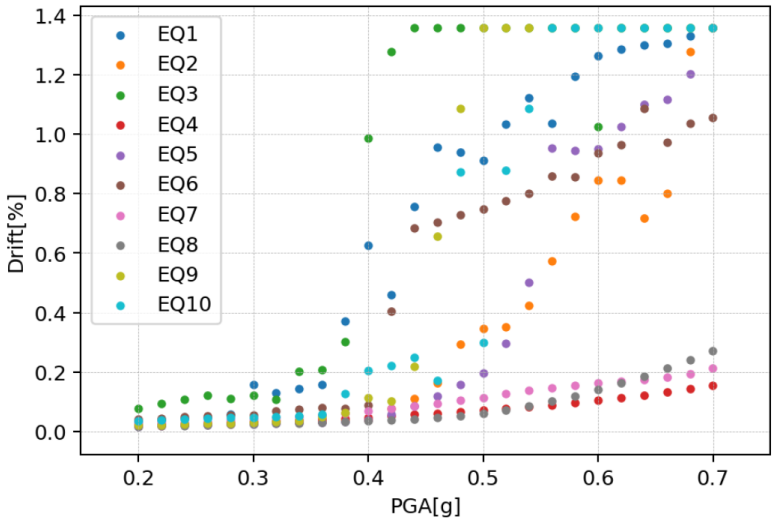

Figure 5.10: Pier drift vs PGA for the lumped plasticity model - Slender wall example

As expected, the response in terms of peak displacement is highly dependent on the shape of the variance spectrum of the input signal, and not only the amplitude of the largest absolute acceleration in the time domain record of the ground acceleration (PGA). In this case, the EQ3 is the governing one, for which the displacement capacity is exceeded at $0.44g$ PGA level. EQ4, EQ7 and EQ8 are not able to induce the non-linearity even at high levels of PGA. Indeed, it is essential to evaluate other earthquake intensity measures. In particular, the duration of the signal, the spectral acceleration estimated at the elastic period of the system, the Arias intensity and the Housner intensity are compared below.

The spectral acceleration SA is expressed as follows:

$$SA = SA(\zeta = 5\%, T = T_{el}) \tag{5.1}$$

The Arias intensity I_A is defined as the time-integral of the square of the ground acceleration:

$$I_A = \frac{\pi}{2g} \int_0^{T_d} a^2(\tau) d\tau \tag{5.2}$$

The Housner intensity I_S is defined as the integral of the pseudo-velocity spectrum within the period range 0.1-2.5 seconds. In the present work, the modified version proposed by [26] is used. For short period structures, such as masonry buildings, the range of periods is set between 0.1 and 0.5 seconds.

$$I_H = \int_{0.1}^{0.5} PSV(\zeta = 5\%, T) dT \tag{5.3}$$

In the graphs below, a comparison of these intensity measures is presented for the 10 records, at PGA level of $0.4g$.

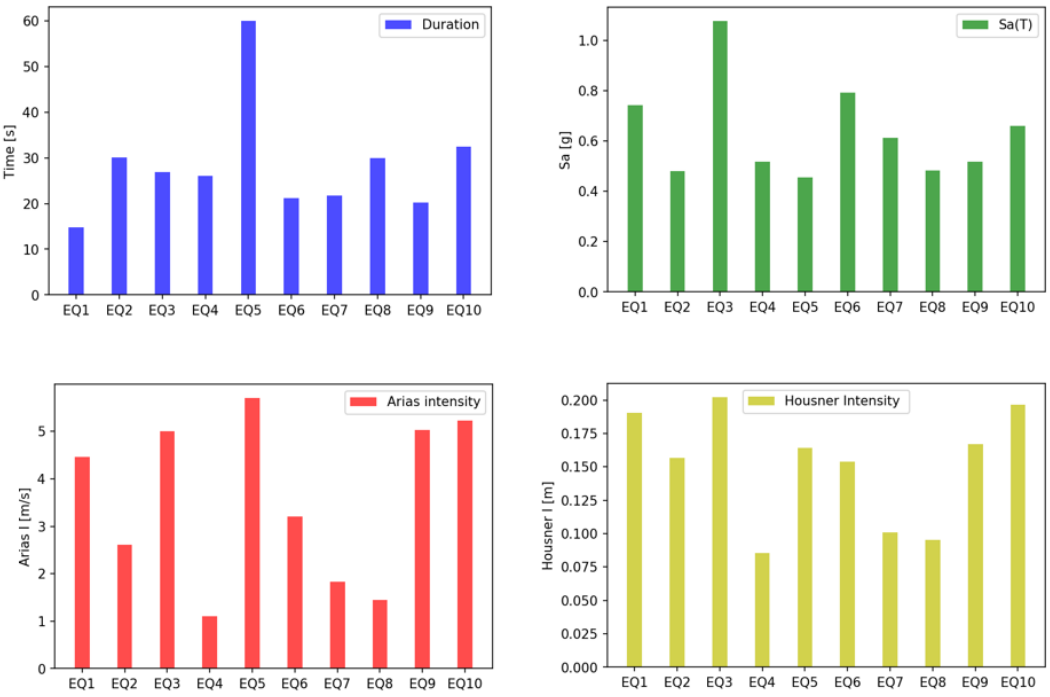

Figure 5.11: Input signal characterization at 0.4g PGA level - Slender component

It can be observed that the governing earthquake EQ3 is associated to the highest spectral acceleration and Hoursner intensity. In addition, the Arias intensity is also conspicuously high. It is important to notice the correlation between the duration of the signal, and its Arias intensity. EQ6 has the highest I_A, due to its very high duration, compared to the other signals. EQ4, EQ7, EQ8 are characterised by low Arias intensity, Housner intensity and relatively low SA. For such reasons, even for high PGA levels, the response of the systems is in the linear range of deformations.

In the graph below, the comparison with LS-DYNA is presented. The 50th, 16th 84th percentiles of the point cloud data are highlighted. Assuming a normal distribution of the drifts for each PGA level, the graph represents the area within one standard deviation around the median.

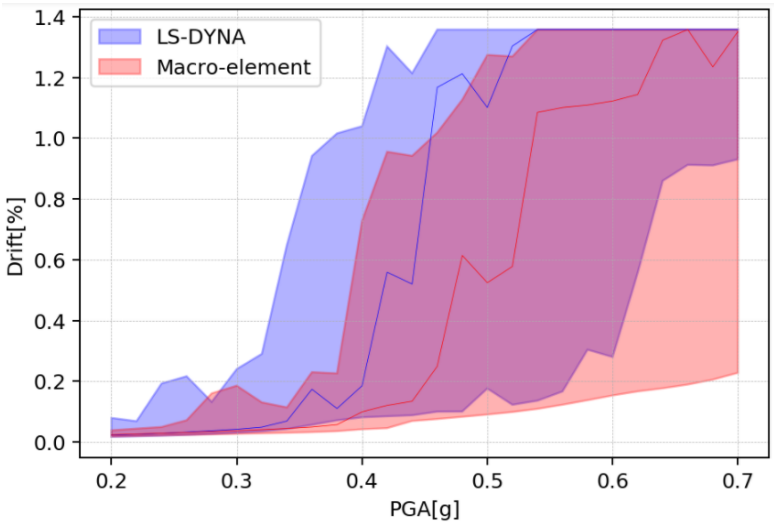

Figure 5.12: Pier drift vs PGA comparison - Slender component

The shell element model reaches failure for drift exceedance for a lower PGA level (0.38g), placing LS-

DYNA on the conservative side. This is likely to occur due to the aforementioned impact phenomenon observed in the shear component example. In fact, one of the conspicuous features of rocking wall seismic behaviour is the presence of gap opening and closing phenomenon, characterized by an interaction of wall base and foundation top. This phenomenon is assessed in Appendix D.

Priorly to the point cloud capacity curves assembly, a butter-worth filter is adopted to remove the high-frequency spikes of the base shear force time series. It is a second order digital butter-worth filter with cut-off angular frequency of 0.1 $\frac{\text{rad}}{\text{s}}$, in which the transfer function in the Z-domain is given by:

$$H(z) = \frac{B(z)}{A(z)} = \frac{b_0 + b_1 z^{-1} + b_2 z^{-2}}{1 + a_1 z^{-1} + a_2 z^{-2}} \tag{5.4}$$

For both the modelling approaches, the trend of the point cloud is identified with a tenth order polynomial fitting.

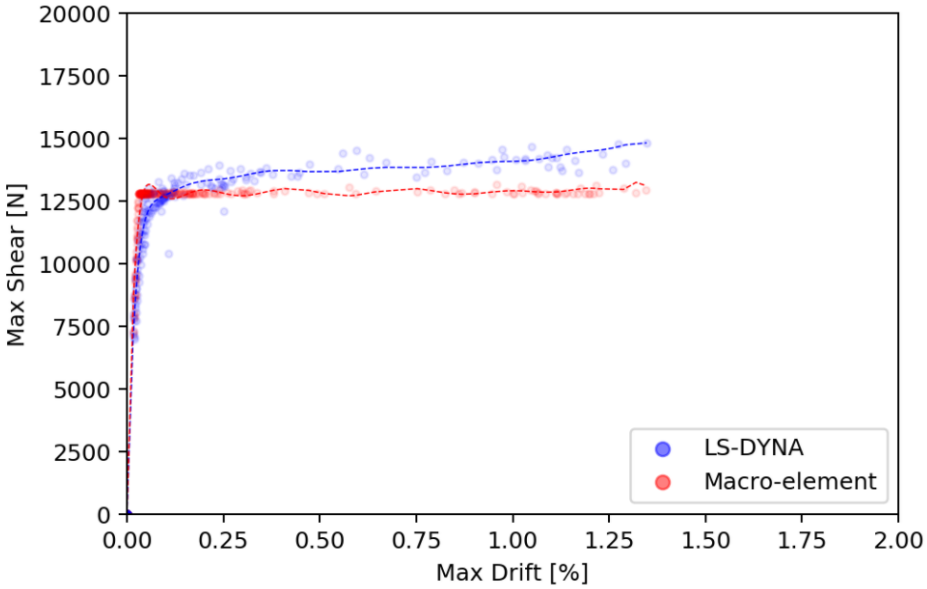

Figure 5.13: Capacity curve comparison - Slender component

The initial stiffness is in good agreement, and the macro-element results in the conservative side in terms of maximum capacity. The very sharp transition between initial-and post yielding is due to the flag shape law adopted.

In addition, the hysteretic energy is compared for the two approaches. As mentioned in the previous sections, the hysteric energy, absorbed by the structural system during a seismic event has been recognized to be useful seismic performance indicator. In the picture below, the hysteretic energy for the 10 GM's is presented at 0.40g of PGA level.

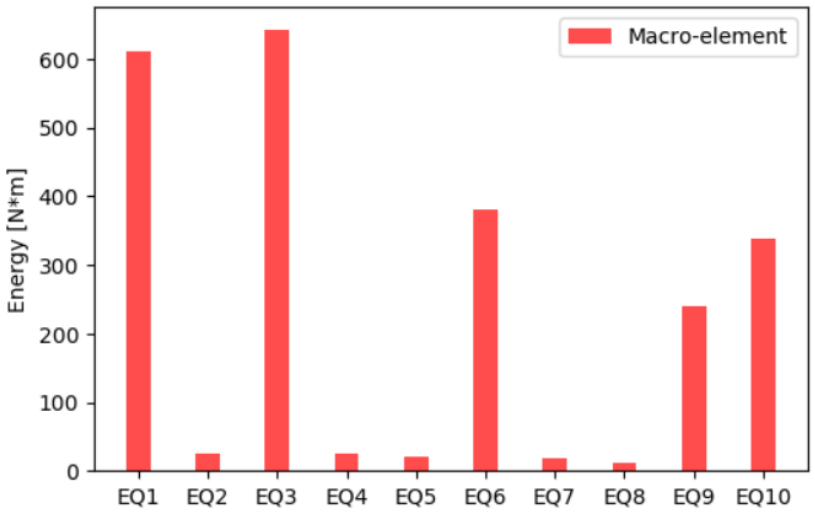

Figure 5.14: Energy dissipation for the 10 records at 0.40g PGA - Slender component

It can be noticed that at the same PGA level, the shape of the input signal does very much influence the response of the specimen and leads to a considerably different seismic demand. The discrepancy between each GM reflects the input signal characterisation presented in Figure 5.11. It is worth mentioning also that amount of energy that the rocking system can dissipate is significantly less from the shear driven specime presented in Figure 5.22.

In the graph below, a comparison between the macro-element approach and the LS-DYNA model is presented in terms of internal energy.

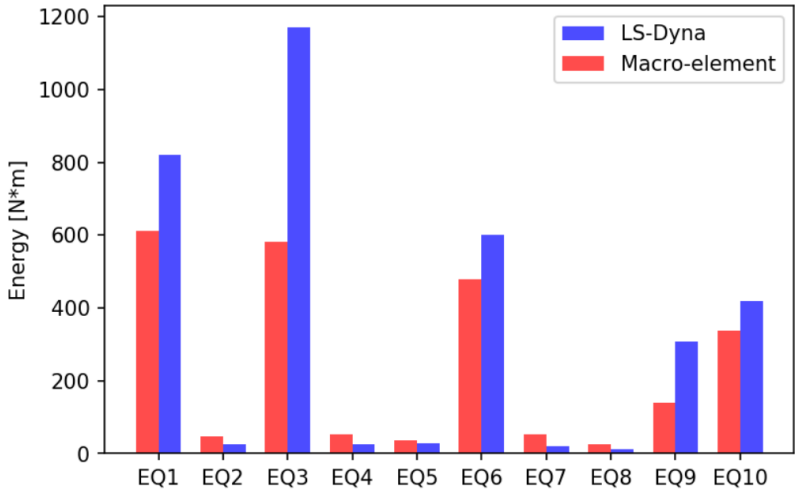

Figure 5.15: Energy dissipation comparison for the 10 records at 0.40g PGA - Slender component

The output of the two model is significantly different, and it can be ascribed to two reasons. Firstly, regarding the GM's which induce the system lightly in the inelastic range, the discrepancy comes from the flag shape hysteretic model adopted. In the 2D shell element model, the smooth curvature of the transition between initial- and post-yielding stiffness is such that the energy dissipation starts already at low level of inelastic strains. Instead, the sharp change of stiffness in the rotational springs of the macro-element entails that the system enters in the yielding domain at a later stage. This has been observe already in Section 3.4.2. In particular the internal energy plot shows that for low displacement level, the LS-DYNA model energy is always higher (Figure 5.16). This effects vanishes as the drift level increases. This can be observed for GM 1, 4, 5, 7, 8, for which the discrepancy is more than 50%. One should notice that in this regard the macro-element model is on the conservative side.

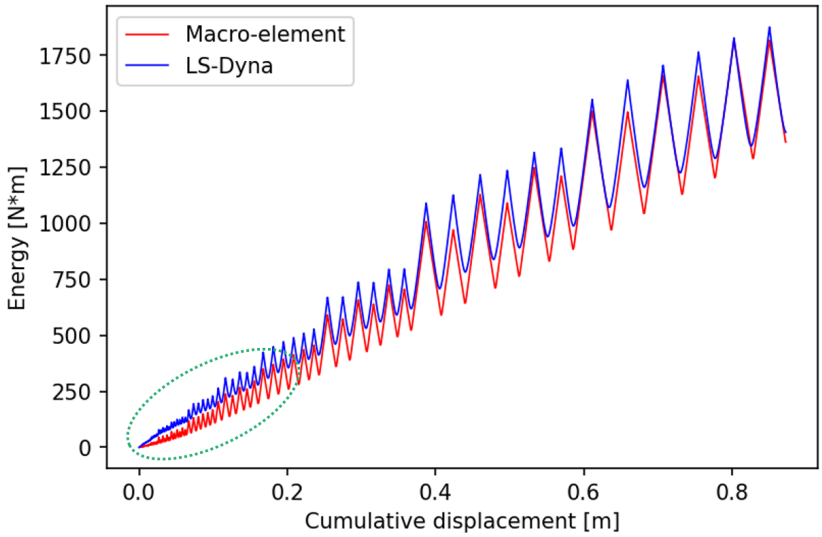

Figure 5.16: Energy dissipation comparison at low drif levels during quasi-static test

For high level of drifts, such are those related to GM 1, 3, and 6, another phenomenon characterised conspicuously the 2D shell element models. It is the gap opening and closing phenomenon (Appendix D). This entrails a discrepancy of 30% in average.

5.3.2. Shear component

The same test is carried about out on a squat wall component. The geometry is described in Table 5.3. With the software LS-DYNA, the analysis are performed with MPP. The macro-element approach analyses are instead run with a single CPU. A comparison in terms of computational cost is given in Table 5.5. Despite the lower CPU number, the lumped plasticity approach is computationally more efficient by two orders of magnitude. It is assumed that using parallel processing, the macro-element could reduce the computational time by at least one order of magnitude [57].

Table 5.5: Computational cost comparison for the point cloud analysis

	LS-DYNA	Macro-element
Elements	1120	5
DoF's	3444	8
CPU	20	1
n. of GM	10	10
PGA range	$0.20 \div 0.70g$	$0.20 \div 0.70g$
n. of runs	250	250
Analysis time	2400 min	20 min

The pier drift vs the PGA per ground motion record is presented for the proposed model in Figure 5.17. As described in Section 2.2, the upper-bound for the drift capacity of the shear component is set to 0.53%.

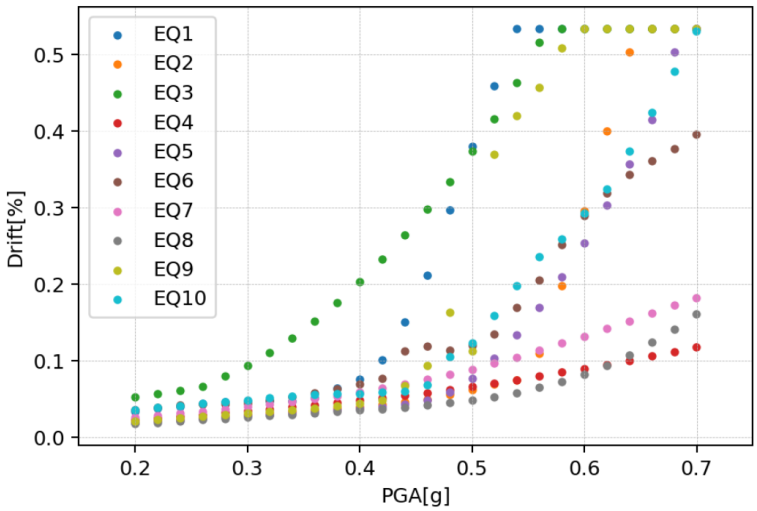

Figure 5.17: Pier drift vs PGA for the lumped plasticity model - Squat wall example

The governing GM's spotted by the model are EQ1 and EQ3, exceeding the displacement capacity at a PGA level between $0.54g$ and $0.56g$. EQ4, EQ7 and EQ8 are the ones leading to the lowest drifts. As observed for the rocking behaviour, a large scattering characterises the response. This can be explained comparing the intensity measures introduced in the previous section. Hence, in the graphs below, the input signals are compared in terms of spectral acceleration at the elastic period, arias intensity, Housney intensity and duration. A reference PGA level of $0.5g$ has been selected for the comparison.

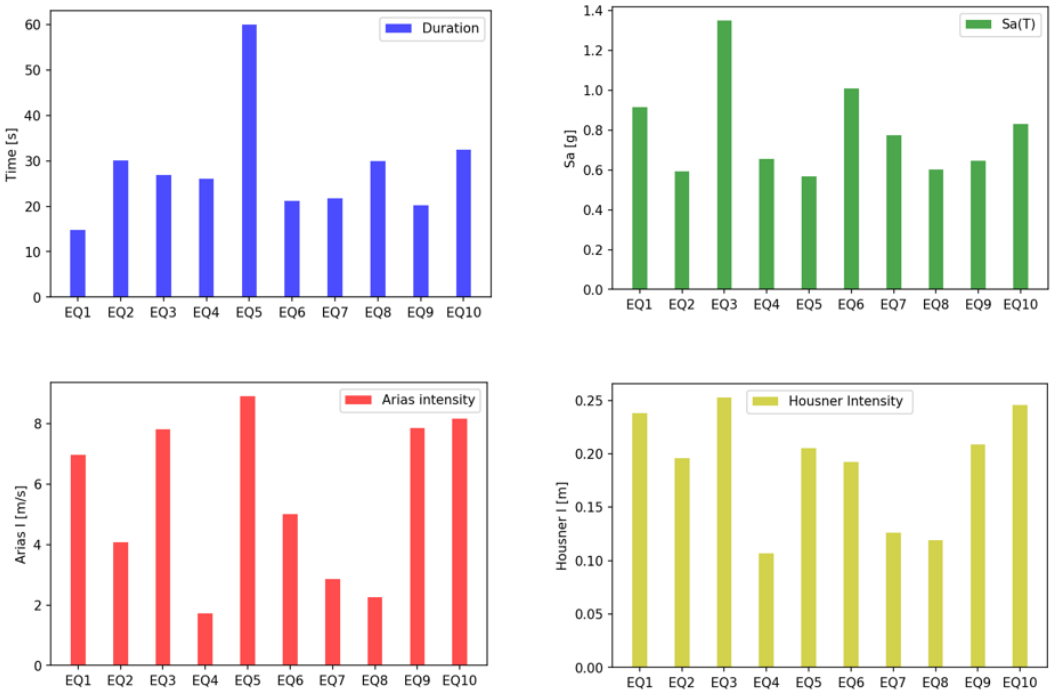

Figure 5.18: Input signal characterization at $0.5g$ PGA level - Squat component

Analogously to case of the slander component, it can be observed that the governing earthquakes EQ3 and EQ1 are associated to the highest spectral acceleration and Hoursner intensity. In addition, the Arias intensity is also conspicuously high. EQ4, EQ7, EQ8 are characterised by low Arias intensity, Housner intensity and relatively low SA. For such reasons, even for high PGA levels, the response of the systems is in the low inelastic range of deformations.

In the graph below, the macro-element and the 2D shell element model are compared in terms of drift vs PGA level. The area bounded by one standard deviation around the median is highlighted. The governing GM's spotted by the 2 models are the same, EQ1 and EQ3, exceeding the displacement capacity at a PGA level between 0.54g and 0.56g . Large scattering for PGA level is observed also in the LS-DYNA trend.

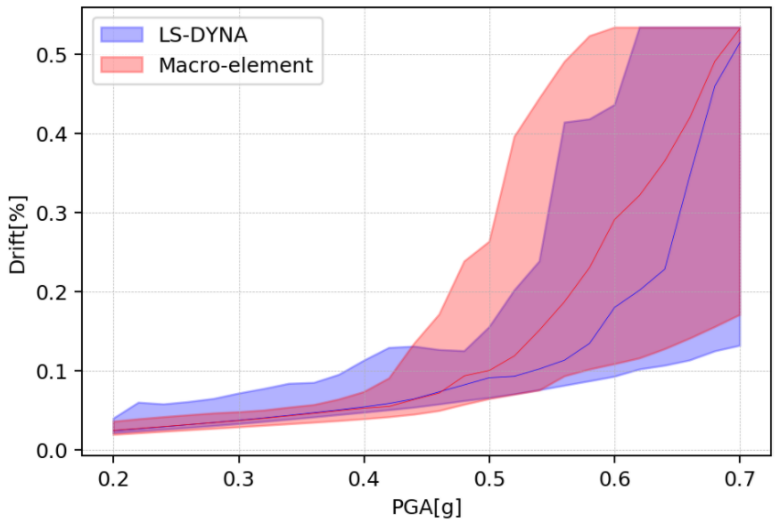

Figure 5.19: Pier drift vs PGA - Comparison between LS-Dyna and macro-element model - Squat component

Finally, the point cloud backbone is built for the two systems. The trend is identified with a tenth order polynomial fitting (Figure 5.20).

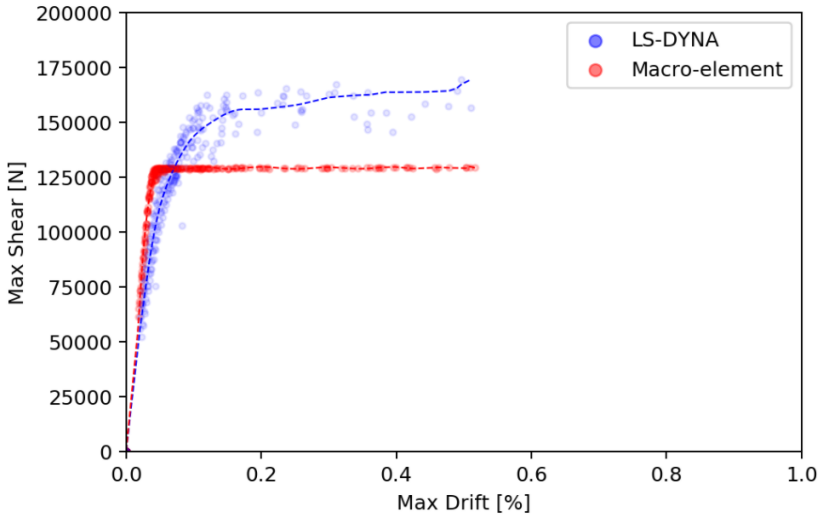

Figure 5.20: Capacity curves comparison - Squat component

At low levels of drift the macro-element matches well the LS-DYNA response. The capacity described by the lumped plasticity approach seems to be in the conservative side. Very localised spikes of maximum shear force (observed also in Section 5.2) at high PGA levels in LS-DYNA are likely to originate from an impact phenomenon. It is the effect of short-duration large-amplitude gap opening and closing along the horizontal mortar joints (left of Figure 5.21), superimposed to the purely translational diagonal mode (right of Figure 5.21). This behaviour is described in Appendix D.1.

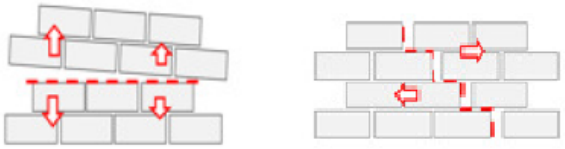

Figure 5.21: High-frequency bed-joint opening (left), superimposed to the translational diagonal mode (right)

In addition, the hysteretic energy for the 10 signals at 0.50g PGA level is compared in the graph below.

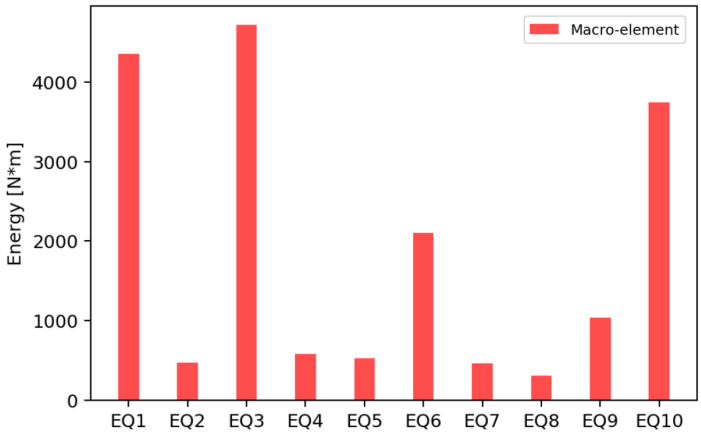

Figure 5.22: Energy dissipation comparison at 0.50g PGA - Squat component

It is clear that the shape and the duration of the input signal, not only the maximum acceleration influence the response of inelastic systems. The very different seismic demand reflects the results presented in Figure 5.18. The large scattering of the response proves that it is essential to perform the analyses with several input records. Only in this way, one is sure to cover a reasonably large number of scenarios. The hysteretic energy of the macro-element model is compared to the smeared plasticity model results.

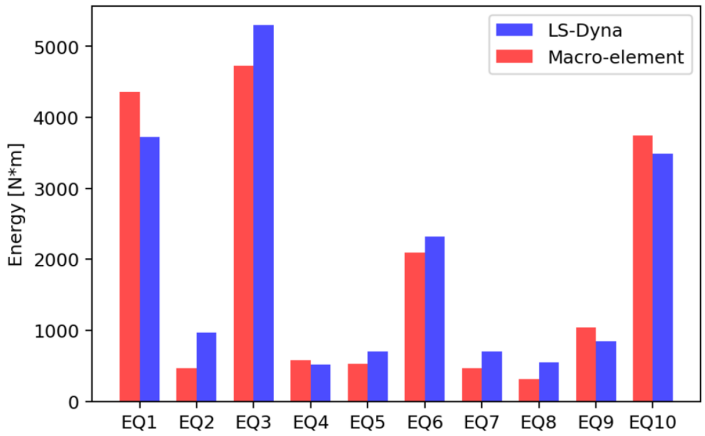

Figure 5.23: Energy dissipation comparison for the 10 records at 0.50g PGA - Squat component

There is a good agreement between LS-DYNA and the macro-element model, proving that the elasto-plastic law proposed is suitable for the prediction of shear driven wall components. Less than 10% discrepancy is observed for all signals.

6

Benchmark building

In this chapter, the macro-element developed is assemble into an equivalent frame structure, a two-storey prototype composed of calcium silicate masonry walls and concrete floors. The scope is to perform a validation test of the lumped plasticity approach. The assembled structure is representative of a typical terraced house built in the period between 1960 and 1980 in the Groningen area. The benchmark quasi-static results consist on the quasi-static laboratory test and the LS-DYNA displacement-controlled analysis. Regarding the dynamic response, the benchmark results are produced with the LS-DYNA NLTH analyses.

6.1. Description of the assembled structure

The assembled structure represents the inner bearing leaf of a terraced house, which was typically built in 1960-1980 in the Netherlands.

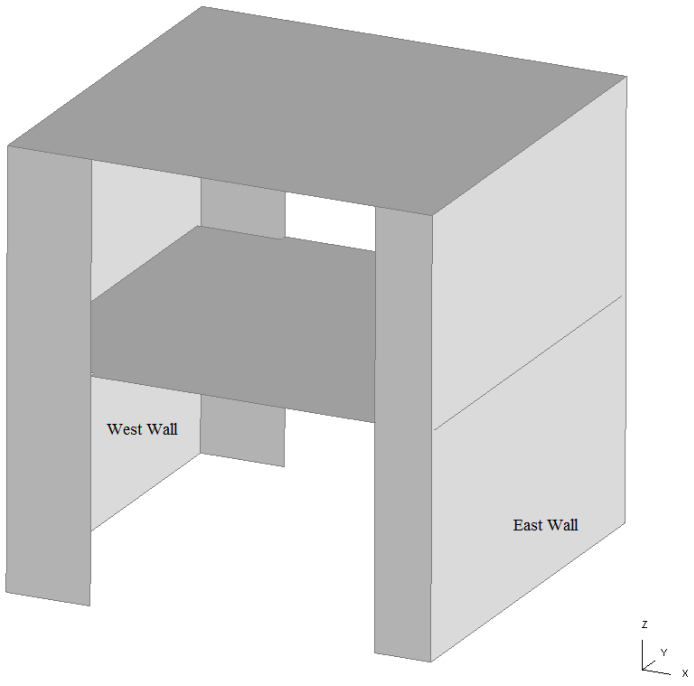

Figure 6.1: 3D view of the assembled structure

The replicated masonry adopted in the tested assemblage is composed of calcium silicate bricks and general purpose mortar.

Table 6.1: TUD-BUILD-1 material properties

	Measure Properties
Young's Modulus	3.5E3 MPa
Compressive strength	7.0 MPa
Poisson's ratio	0.2
Bed-joint shear strength	0.25 MPa
Diagonal-tension strength	0.1 MPa

The structure consists of two loadbering walls on the west and east side, and two facaded composed on two piers with width of 660 mm and 1100 mm. The floors consisted of two prefabricated concrete slabs spanning between the loadbearing walls. The two concrete slabs were in-situ connected by reinforced concrete dowels. At fist floor level, the floor was connected horizontally to the piers by anchors of 6 mm diameter. At second floor level, the floor was laid on both the loadbering walls and the piers. However, during construction, the floor was laid on the loadbearing walls and subsequently the joint between the piers and floor was filled with mortar. As a consequence, the load is carried out only by the loadbering walls.

The geometry of the assemblage has been designed to investigate the influence of the following building characteristics:

- Presence of slender piers, due to the presence of large openings in the facades
- Presence of long transversal walls that are connected to the facades by the running bond
- Limited connection between concrete floor and masonry wall

The assembled structure has been tested under quasi-static cyclic pushover load and at different stages a dynamic identification test has been performed [48]. The objective of pushover test is to determine the structural response of the structure under cyclic loading in terms of load-displacement relationship, which provides information on the capacity and ductility of the structure, and to investigate the crack propagation during the test. The objective of the dynamic identification test is to determine the eigen-frequencies of the structure at different damage states.

6.2. Modelling approach

In this section , the modelling approach of the macro-element assembly is presented, with particular attention on the mass lumping and the non-linear springs behaviour. A brief overview on the LS-DYNA modelling approach is included.

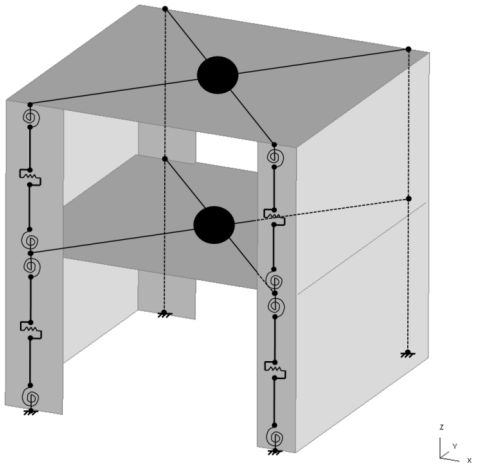

Figure 6.2: Macro-element approach - TUD-BUILD-1

Following the equivalent frame approach mentioned in Section 3.2, each of the four pier is assembled by using two macro-elements on top of each other. This is implemented due to the necessity of having a

mid-heigh node where to connect the first floor mass. Consequently, the rotation at the mid-height node is constrained to be equal for the two rotational springs, since the construction detailing is such that the elements present structural continuity from the base to the second floor level. The floors are modelled with rigid beams, both in axial and bending behaviour, in such a way to enforce a fix-fix boundary condition for the piers.

As presented in the introduction, the macro-element approach relies on the assumption that the dynamic behaviour in the horizontal and vertical direction is uncoupled. Hence, the mass of the floors, flanges and piers in the vertical direction is used for the calculation of the spring yielding moments, which are supposed not to change during the analysis. The vertical forces acting on the structure are presented in Figure 6.4.

In the horizontal direction, the masses are assembled in the mass matrix of the translational equation of motion. Regarding the first floor, the total mass given by the the mass of the concrete floor and the portion of the transversal wall from mid-heigh of the first floor to mid-heigh to the second floor. Analogously, for the second floor, the total mass consists on the mass of the concrete floor and the half heigh portion of the transversal wall.

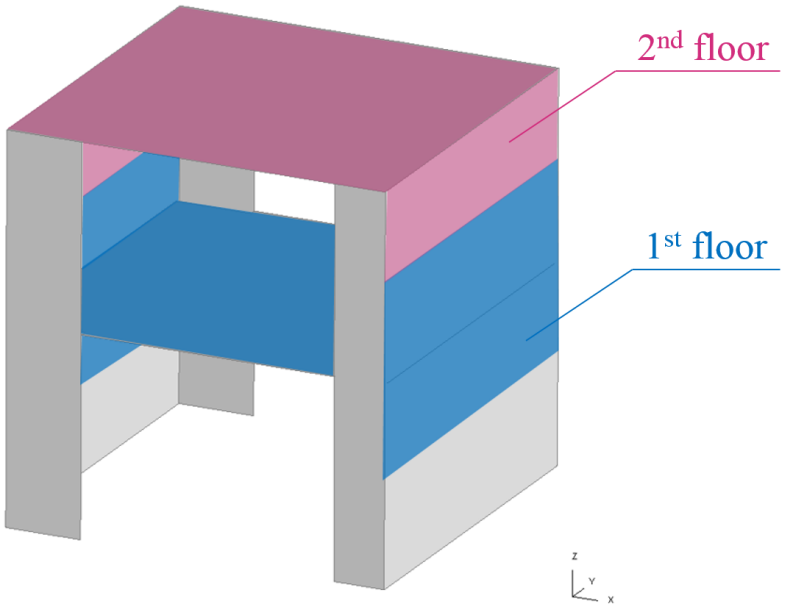

Figure 6.3: Mass lumping at floor level

In the vertical direction, the mass of floors, piers and transversal walls is used for the estimation of the yielding moment. The following assumption are made in order to carry out the calculations.

- The entire weight of the floor is equally transferred to the four piers.
- Independently on the loading direction both piers are active and can take up lateral loading.
- The floor acts as a fully rigid restrain for the top of the piers.
- Part of the transversal wall (moving out-of-plane) moves together with the pier.

The assumptions translate into the force distribution presented in the figure below.

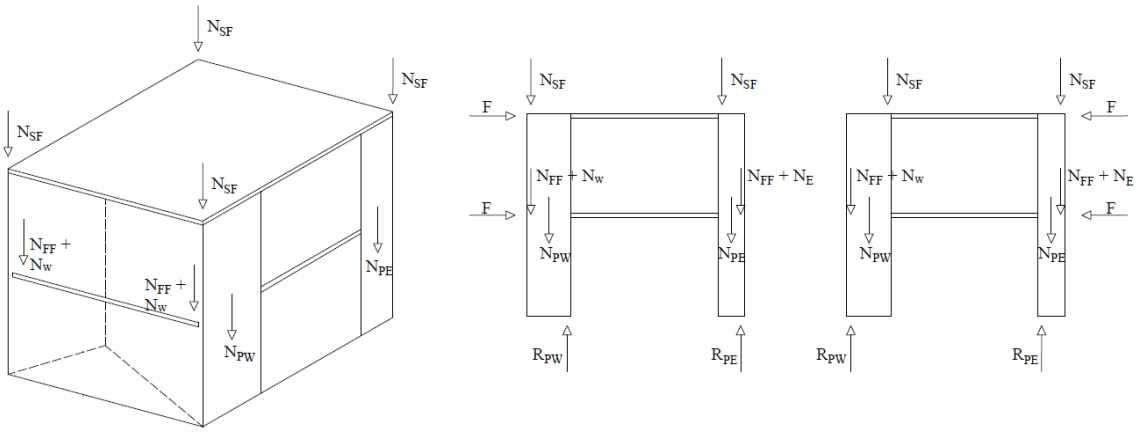

Figure 6.4: Assumption load distribution for rotational spring properties

A key aspect is related to the estimation of portion of the transversal wall, uplifted during the pier rotation. Following the approach proposed in [14] and considering the wall-to-pier connection as fully interlocked connection, a trapezoidal part of the transversal wall is assumed to cooperate with the piers.

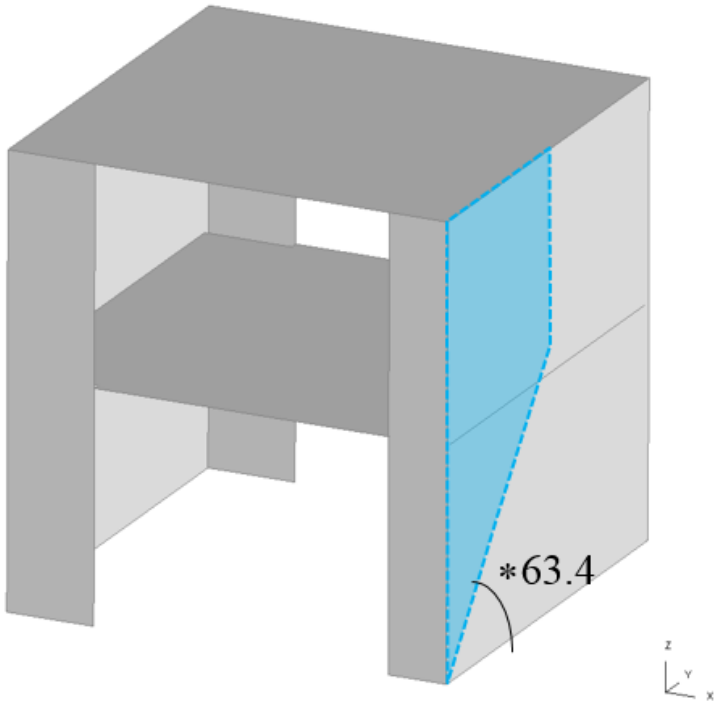

Figure 6.5: Portion of the transversal wall, assumed to contribute on the in-plane behaviour [14]

Therefore, the flag-shaped material model developed for the flange effect is assigned to the rotational springs providing the asymmetric hysteretic curves presented in the figure below.

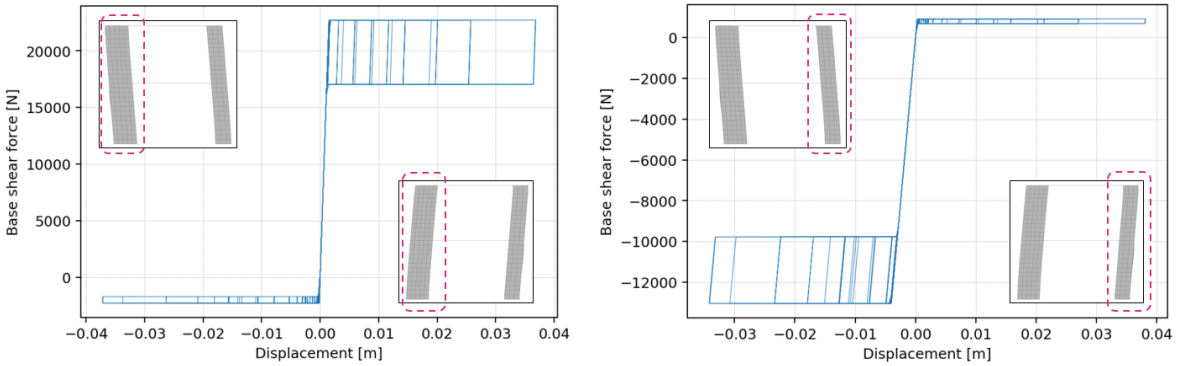

Figure 6.6: Cyclic behaviour of west pier (left) and east pier (right) - Macro-element - Active and passing pier effect due to flange participation

The flange effect contribution is indeed observed also in the smeared plasticity model.

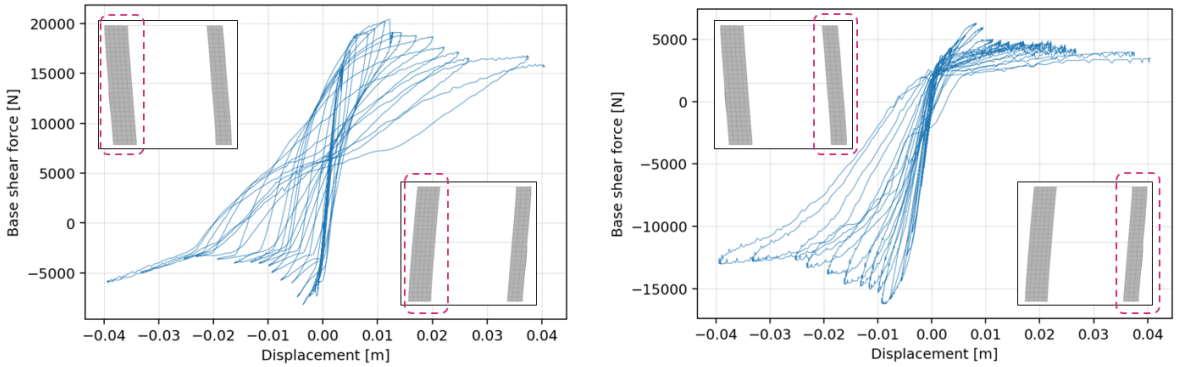

Figure 6.7: Cyclic behaviour of west pier (left) and east pier (right) - LS-DYNA model

With LS-DYNA, in order to evaluate the behaviour of masonry, homogenized shell masonry material (Section 3.3) model is used with fully integrated shell elements. Shell elements and beam elements are used to model the non-linear concrete floors and the anchors respectively.

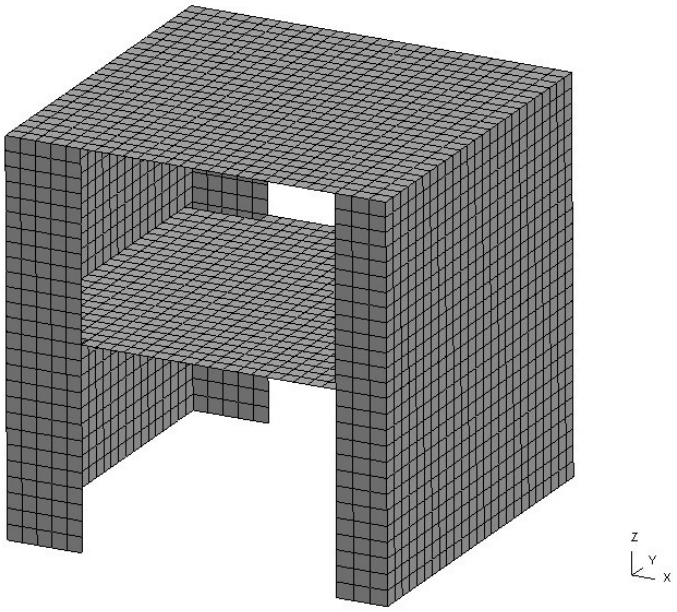

Figure 6.8: Shell element model - TUD-BUILD-1

6.3. Experiment results

In this section the main experimental results are presented. The pushover test was performed in three phases namely initial, pre-peak and post-peak phase. The global behaviour for the structure is presented in terms of capacity curve in the figure below.

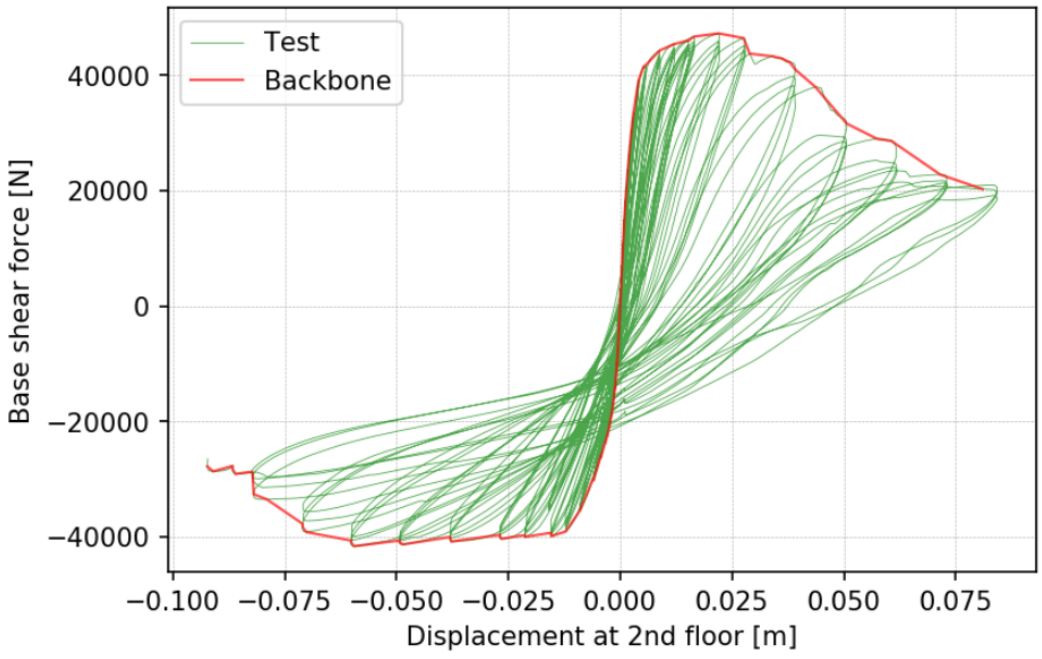

Figure 6.9: Response of the assembled structure: capacity curve and corresponding backbone curve

Due to the different pier width, the behaviour in capacity and ductility are asymmetric. The capacity asymmetry is directly related to the flange effect mentioned in the previous section. The ductility asymmetry is linked to the crack patter evolution during the test.

6.4. Dynamic identification test

The dynamic identification is based on the hammer impact method which is a non-destructive identification method. The structure can be excited globally provided that the connections between the various parts of the structure are monolithic (i.e. the connections are such that the energy flow between the various parts can be ensured). The hammer impact generates waves which are guided through the structure. The reflection of those waves at the various boundaries of the structure forms a standing wave pattern or the modal shapes of the system under investigation. The dynamic properties normally identified are the natural frequencies, the modal shapes and the modal damping; the focus in the present section is on the first and second elements only. For the data analysis, the choice was to focus only on the first global bending mode of the assembled structure along the X-direction.

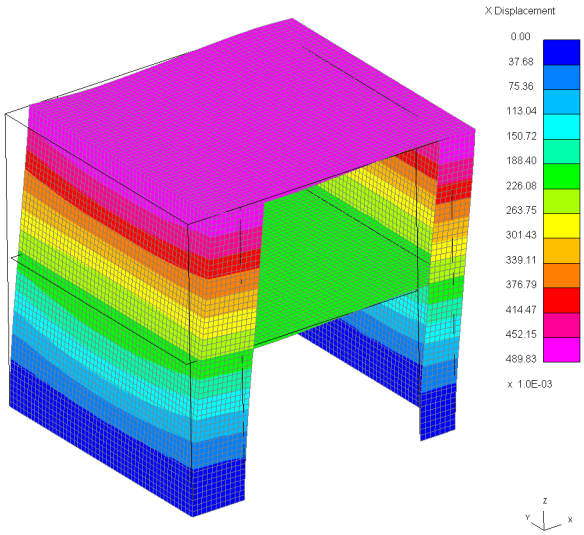

Figure 6.10: Dynamic test: First eigen-mode of the structure in X-direction

The impact tests were performed at the following moments of the pushover test:

- Test 1: Before the cyclic pushover test started. The assembled structure was undamaged.
- Test 2: At the end of the pre-peak phase, at which a reduction of the stiffness was observed from the capacity curve and also significant cracking could be visually observed.
- Test 3: At the end of the pre-peak phase, at which a reduction of the stiffness was observed from the capacity curve and also significant cracking could be visually observed.

The laboratory results in terms of mode shape and eigenvalue at the un-damaged state (test 1) are compared with the shell-element model and the lumped plasticity model. Given the high non-linearities of the masonry material model even at small strains, the eigenvalue analysis is not the favourable approach for the identification of the first mode of the structure. Alternatively, the dynamic identification test is performed numerically with software LS-DYNA. A displacement of the magnitude of 1 mm is applied at the top floor and the structure is left freely to vibrate. The acceleration history of a representatives node belonging to the top part of the structure is recorder (nodal acceleration vs time curve). By applying the Fourier transform of the time-based signal the function can be converted between the time and frequency domain [21].

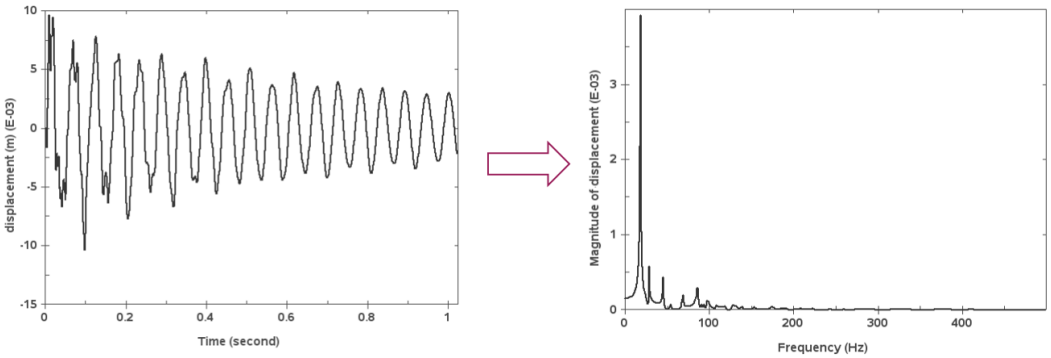

Figure 6.11: Fourier transform of the time-based signal to obtain the response in the frequency domain

$$H(\omega) = \int_{-\infty}^{\infty} h(t) e^{i\omega t} dt \tag{6.1}$$

In the present case, the $h(t)$ function is the nodal acceleration history. From the frequency domain excitation the first natural frequency corresponding to the first dominant mode can be estimated. The same procedure has been performed for the structure modelled with the proposed macro-element model. The results are presented in Table 6.2. Regarding the quasi-static test, the stiffness matrix K can be determined on the basis of the stiffness of the first and second floor as measured during the cyclic pushover. The stiffness of the assembled structure can be evaluated via linear regression of the capacity curves in terms of displacement at the second and first floor level [48].

Table 6.2: A comparison between the identified natural frequency by the dynamic tests, with the stiffness obtained in the push-over test, with LS-DYNA and the macro-element approach.

Type of test	Test 1
	[Hz]
Experimental results of the dynamic identification test	4.05
Calculated based on the stiffness obtained in the quasi-static pushover test	4.07
Dynamic identification on 2D shell model	4.35
Dynamic identification on macro-element assembly	4.38

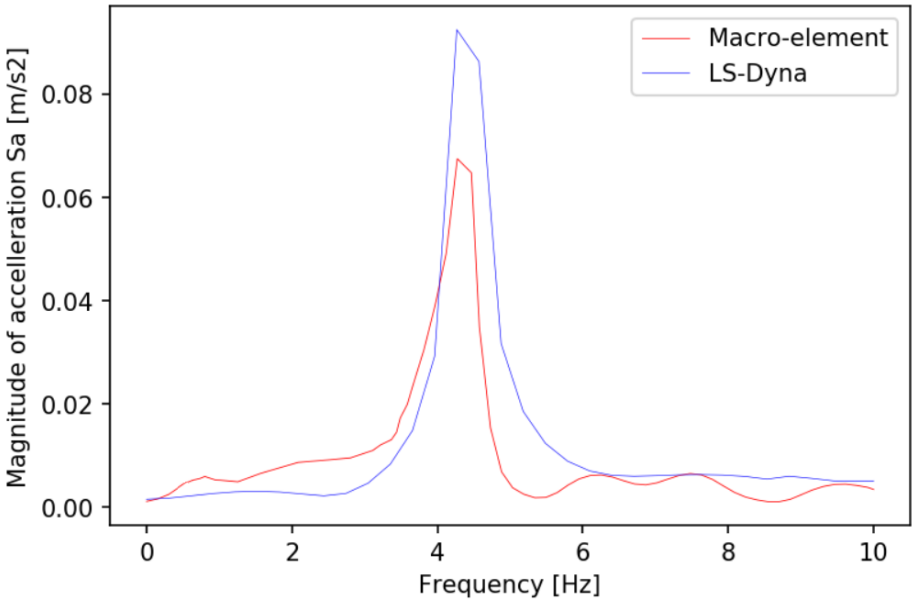

Figure 6.12: Acceleration spectrum for the determination of the first eigenvalue of the structure, for the shell element model and the macro-element model

Both LS-DYNA and the macro-element model seem stiffer than the prototype. This is to be expected, given that intrinsic scattering the material properties of the laboratory specimen. For instance, the numerical models adopt only a single value of the masonry Young's moduls, whilst in assembly is made of mortar and bricks, and hence different parameters could be measured at different locations.

6.5. Displacement-controlled test

A quasi-static blind test is performed with LS-DYNA and the macro-element model. It is a displacement controlled analysis prescribed at the second floor level, in the weak-direction of the structure (X-direction). The loading protocol is shown in Appendix B. The modelling approach is compared in terms of force-displacement curves and internal energy history, with respect to the laboratory tests results.

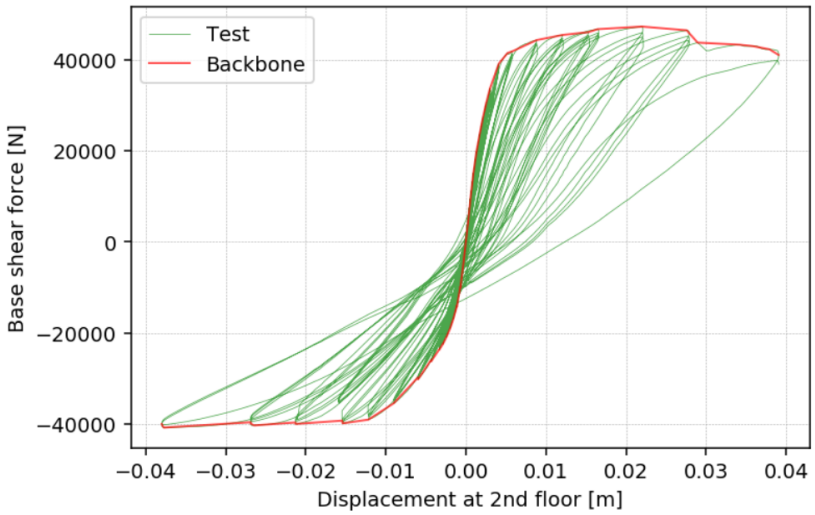

Figure 6.13: Laboratory test capacity curve and backbone up to 40 mm at top floor

It is of interested to compare the results up to 40 mm at the second floor in the both positive and negative direction. Up to this drift level, the maximum capacity has been reached and intensive damage is observed at

the ends of both the smaller and larger piers. Furthermore, in both the transversal walls, the nearly 45 degrees cracks are observed, proving the activation of the flange-effect for the in-plane piers. For displacement larger than 40 mm, the accumulated damage in the the positive direction leads to the formation of through-brick diagonal cracks in the wider piers. This induces strength degradation and large energy dissipation. The lumped plasticity model, based on elasto-plastic backbones is not able to predict the development of a different failure mode, once another has previously occurred (the first global rocking mode). Furthermore, as mentioned above, the typical short duration of the induced earthquakes is such that the structures usually oscillate inelastically only for few cycle, and do not absorb the amount of energy to develop a significant degradation of strength and stiffness. It is more likely the high drift level to suggest the identification of a near collapse limit state. This is indeed reflected in the NLTH analyses results of the next section: the results do not show high residual permanent deformation at the end of the test, and the structure fails for global overturning (see Figure 6.31).

Even though it is not observed at the component level, a low-intensity pinching phenomenon has been observed in the response of the assembled structure. Pinching is a sudden loss of stiffness caused by cracks opening and closing in cyclic loading. This phenomenon is taken into account in the rocking behaviour via an energy-based phenomenological flag-shaped rule.

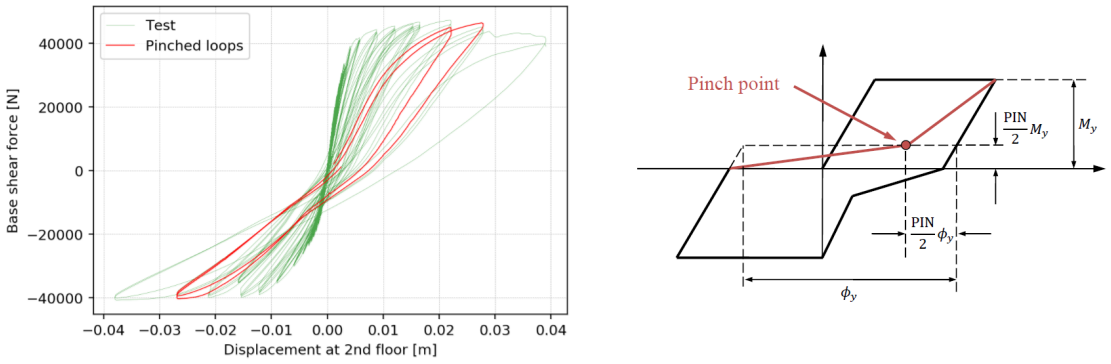

Figure 6.14: Pinching effect in the assembly response

The results in terms of force-displacement curves and energy dissipation history are presented in the figures below.

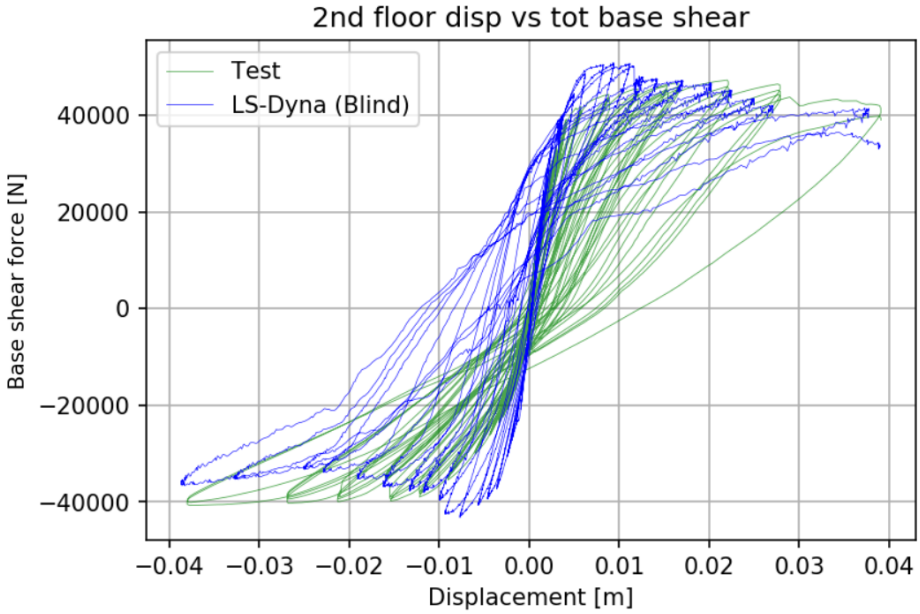

Figure 6.15: Force-displacement curves comparison between LS-DYNA and test results [2]

The capacity in the two loading directions predicted by the smeared plasticity model is in good agreement with the test results. Strength degradation is predicted already at small inelastic displacements, whilst is not the case for the laboratory specimen. One may notice that the small residual displacement at zero base shear force is predicted in the opposite direction (Figure 6.15).

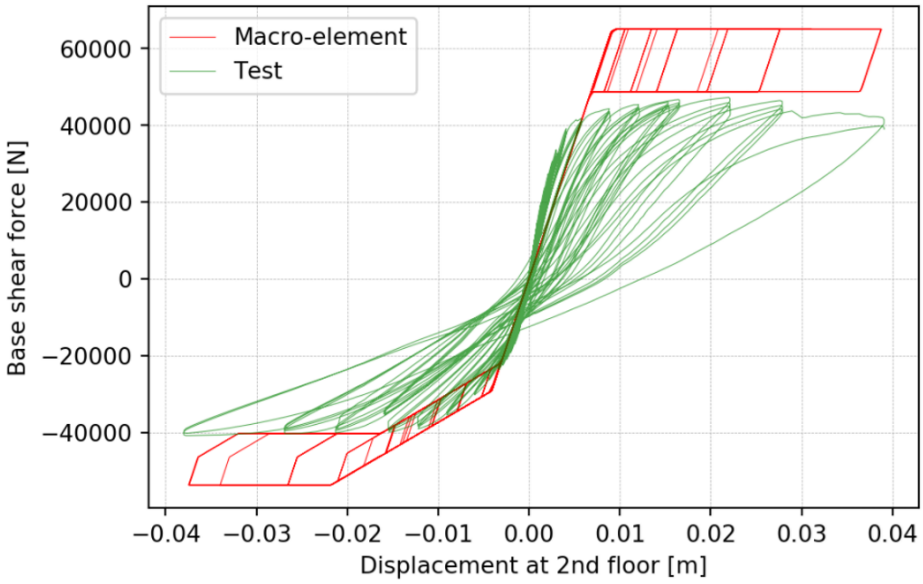

Figure 6.16: Force-displacement curves comparison between the macro-element model and test results

The macro-element predicts the asymmetric backbone due to the flange effect, and the gradual transition from the elastic and yielding branch in the negative displacements, compared to the positive displacements. This is related to the earlier formation of plastic hinges in the narrow piers, due to the different geometry. The capacity is however overestimated of about 20% in both the directions. The reasons lies behind three different aspect:

- The assumption of fully fixed boundary condition at the second floor level translates into an upper bound estimation of the capacity and, as mentioned in Section 2.1.1, is usually not present in actual buildings. One may expect a lower capacity if the diaphragm is left free to bend with a finite out-of-plane stiffness.
- The actual diaphragm deformability is likely to alter the vertical weigh transferred to each pier during the analysis (assumed to be constant and equal to one fourth of the floor weigh).
- The geometry of the trapezoidal area assumed to contribute as additional weigh (flange effect) for the piers relies on a rigid body assumption. The out of plane accumulated damage (see Figure 6.17) is likely to deviate the behaviour from such a simplified assumption.

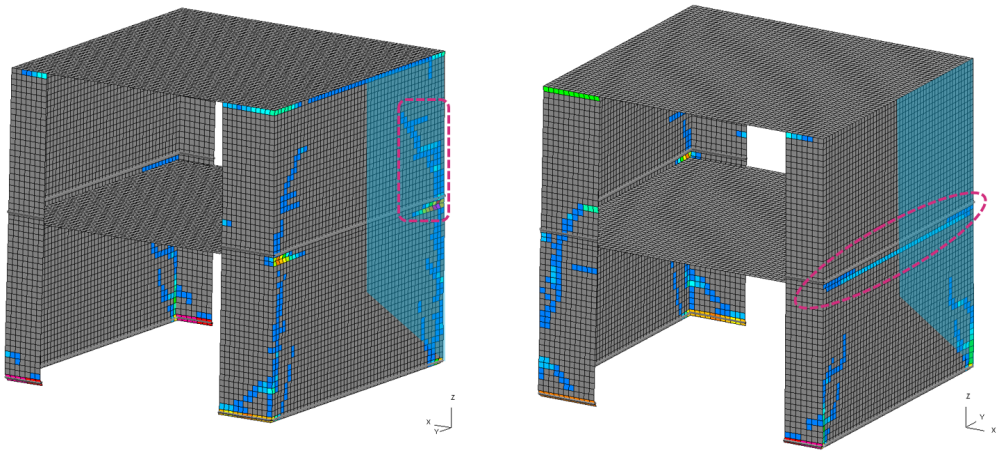

Figure 6.17: Out-of-plane damage of the traversal wall acting as a flange

In order to assess the dynamic behaviour of the building modelled with LS-DYNA and the macro-element approach, it is necessary to calibrate the capacity of latter to be in line with the LS-DYNA values. By applying a reduction factor of 0.75, the backbone behaviour of the equivalent frame is comparable with the shell element model and the laboratory results.

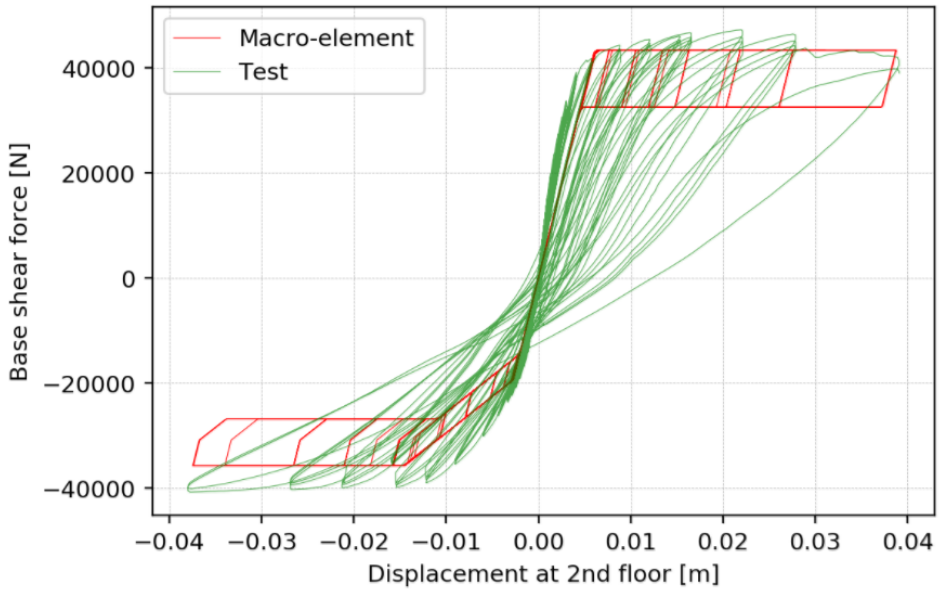

Figure 6.18: Force-displacement curves comparison after the macro-element capacity reduction - Laboratory test and macro-element

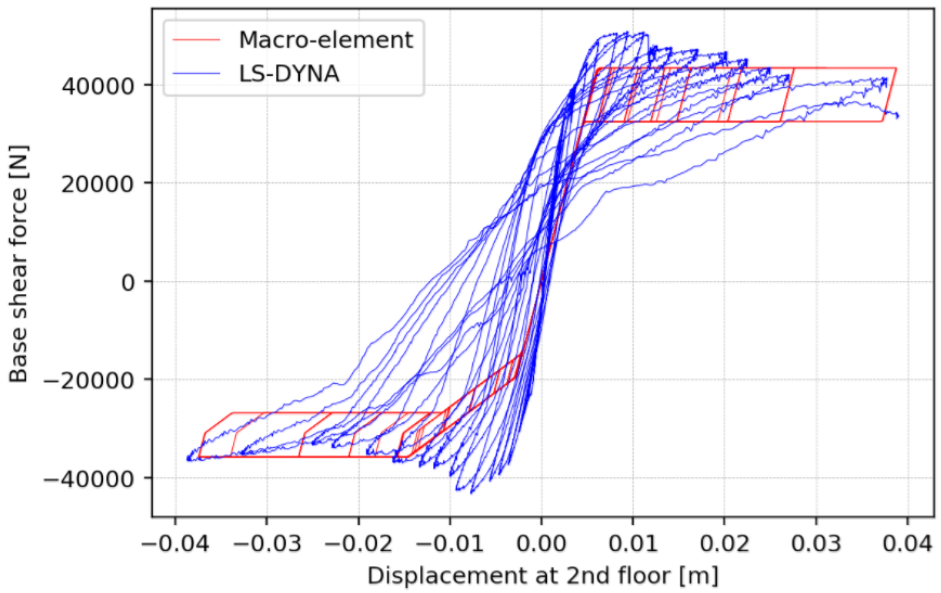

Figure 6.19: Force-displacement curves comparison after the macro-element capacity reduction - LS-DYNA and macro-element

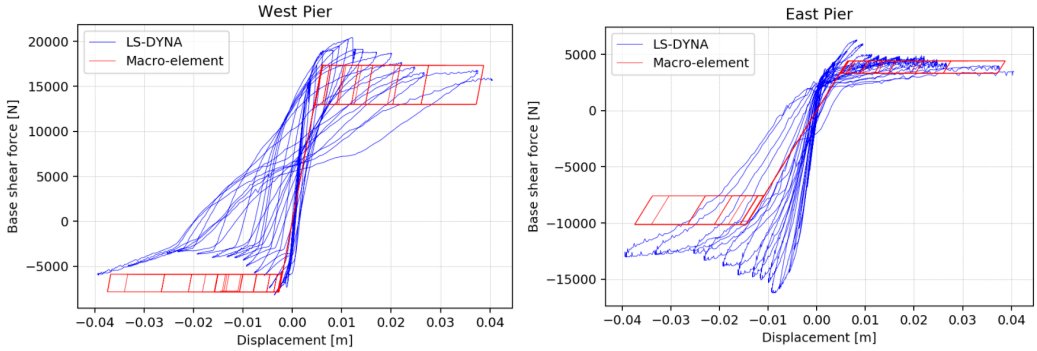

Figure 6.20: Pier hysteresis comparison

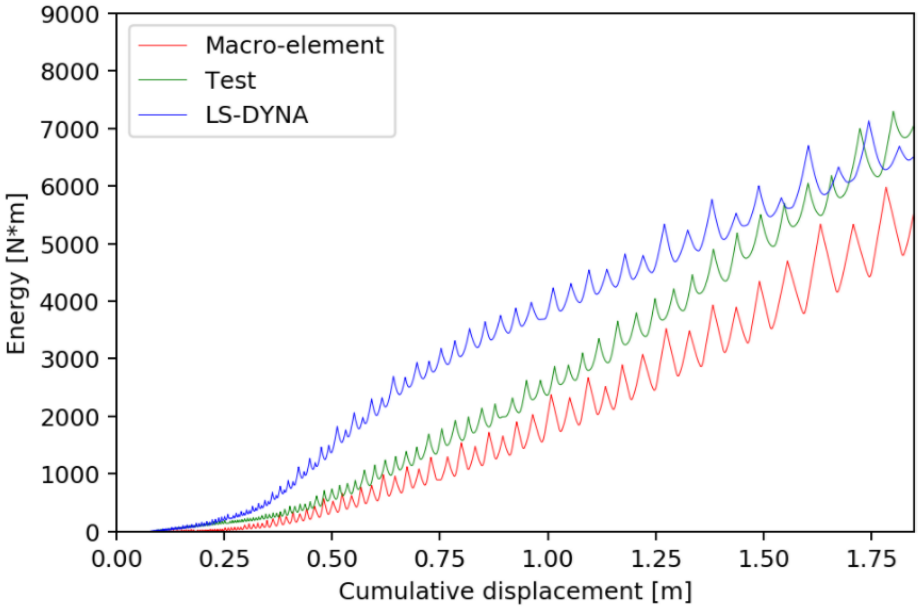

Figure 6.21: Internal energy comparison - LS-DYNA, macro-element and test results

Summarising, up to 40 mm, both the LS-DYNA and the macro-element model identify a rocking mode of the four piers. This is reflected in the (nearly) self-centering behaviour of the results. LS-DYNA and laboratory results display a pivot point which is not coincident with the origin, as it is for the macro-element. This is due to the permanent sliding deformation superimposed to the global rocking behaviour. In terms of energy dissipation, at the end of the protocol (up to 40 mm), the LS-DYNA model for low drift level initially displays high energy dissipation respect to the other two systems. In this regard, the macro-element model is on the conservative side.

6.6. NLTH analysis

Analogously to what presented in Section 5.3, a point cloud dynamic analysis is performed to assess the validity of the macro-element approach with respect to the smeared plasticity model. Hence, the dynamic response of the assembly is assessed using 7 input signals (see Appendix B) with increasing PGA levels, from $0.02g$ to $0.50g$, in steps of $0.02g$, with a total number of 168 runs. With the LS-DYNA, the analysis are performed with MPP, while the macro-element model analyses run on a single CPU. The excitation signal is applied only in the weak direction of the structure (X-direction in Figure 6.2). The Y-direction is regarded as the "strong" direction of the building, given the geometry of the two walls representing the resisting system. In the analysis, the vertical component of the ground motion is neglected (see Appendix C). A comparison in terms of computational cost is presented in Table 6.3.

Table 6.3: Computational cost comparison for the point cloud analysis of TUD-BUILD-1

	LS-DYNA	OpenSees
CPU	20	1
n. of GM	7	7
PGA range	$0.02 \div 0.50g$	$0.02 \div 0.50g$
n. of runs	168	168
Analysis time	100 hr	30 min

Analogously to the outcomes presented in Section 5.3, it is clear the very high computational demand of the smeared plasticity models. In a fragility curves development framework, which requires at least 4000 accelerograms [22], LS-DYNA leads to an extremely high computational time. The proposed approach acts as a suitable moderate-fidelity model for such a purpose. It requires only few characteristics of the building that can greatly simplify modelling of large number of buildings in the Groningen region. On the other hands, the

most computationally-efficient structural models using equivalent SDoF conversion are referred to as “low-fidelity models” [57].

In the figures below, the point cloud analyses results are presented, in terms of maximum drift achieved during the analysis at a certain PGA level. A drift limit value corresponding to the near collapse limit state is calculated with the expression given in Table 2.1, for elements governed by flexure.

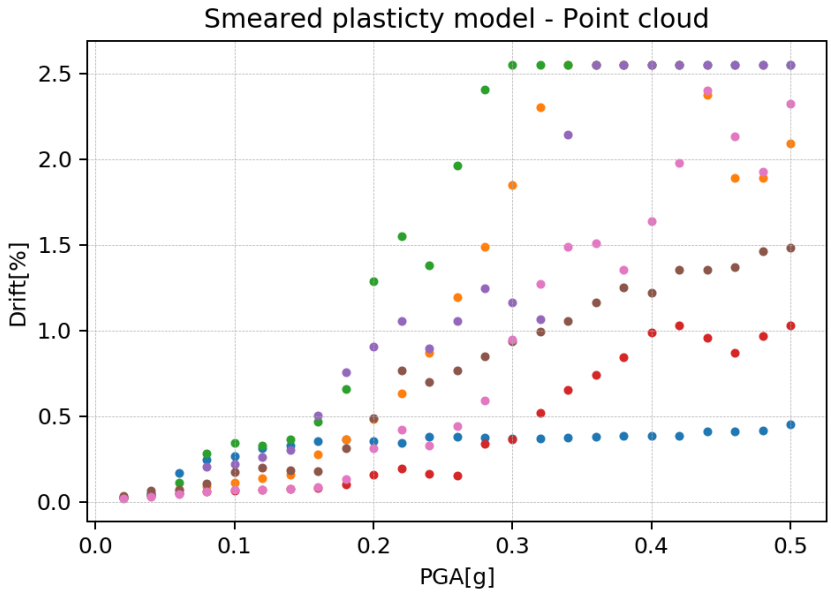

Figure 6.22: Drift vs PGA level - LS-DYNA

The LS-DYNA model reaches collapse with EQ3 at 0.30g PGA level, due to flexural drift limit exceedance.

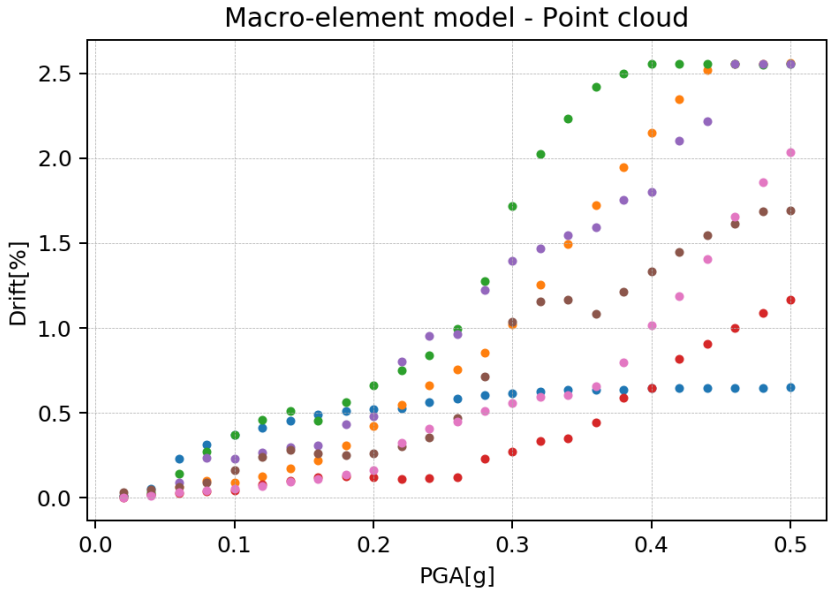

Figure 6.23: Drift vs PGA level - Macro-element model

The macro-element model reach collapse with EQ3 at 0.40g PGA level, due to flexural drift limit exceedance, placing the approach on the un-conservative side with respect to the smeared plasticity model.

However, considering EQ2, LS-DYNA predicts drifts lower than the limit close to 0.50g PGA level, whilst the macro-element model collapses earlier. This is again a clear example of the importance of utilizing a large number of input motions for the assessment of the dynamic behaviour of non-linear systems. In this regard, the proposed approach has the advantage of being computationally efficient and thus allows to perform NLTH analyses with a large number of accelerograms. Despite of the differences, the trends of the cloud show a good agreement between the two approaches.

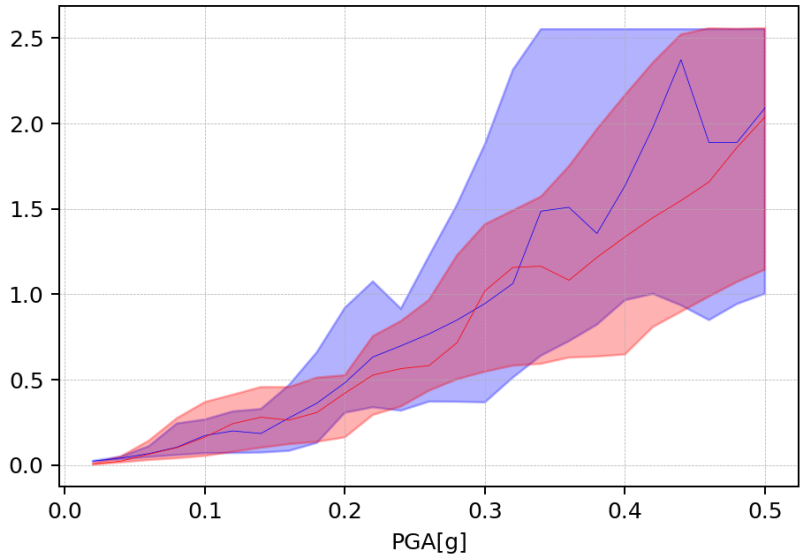

Figure 6.24: Drift vs PGA level - Modelling approach comparison

In the graphs below, the earthquake records are compared in terms of duration, Arias intensity, Housner intensity and spectral acceleration estimated at the initial elastic period (see Table 6.2), at PGA level of 0.3g.

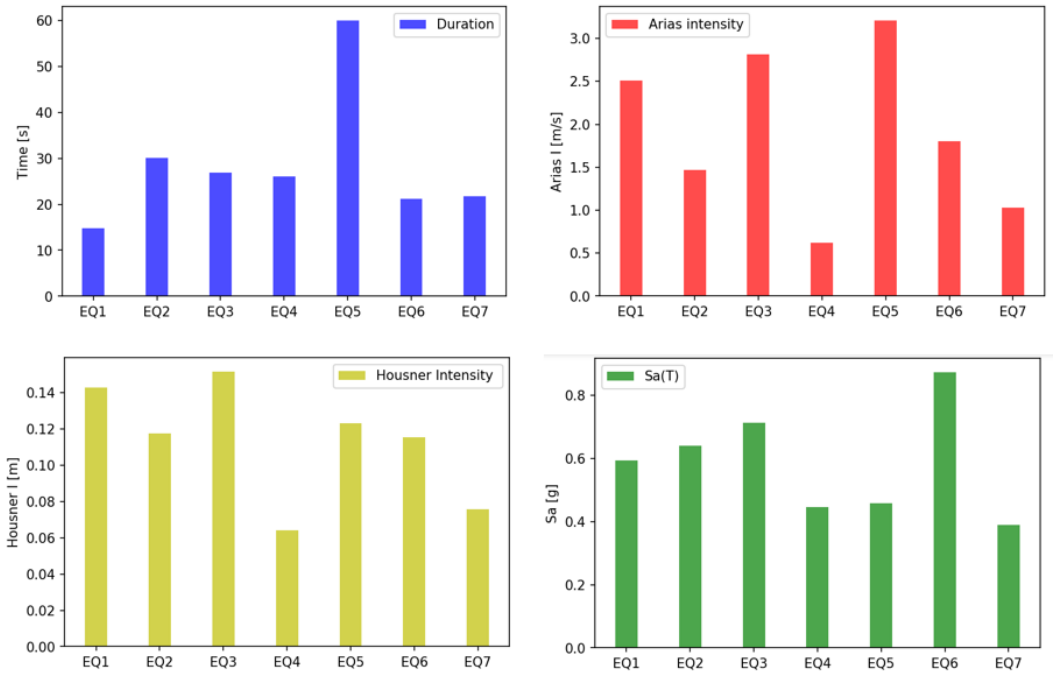

Figure 6.25: Input signal characterization at 0.3g PGA level- TUD-BUILD-1

It can be observed that the governing earthquake EQ3 is associated to an high spectral acceleration and the highest Hoursner intensity. In addition, the Arias intensity is also conspicuously high. EQ4 is characterised by low Arias intensity, Housner intensity and SA. For such reasons, even for high PGA levels, the system does not reach collapse for drift limit exceedance. One may notice that EQ1, even though characterised by high values of Arias intensity, Housner intensity and relatively high SA, is the signal leading to lowest drifts also for high PGA levels. However, for periods longer than 0.5 s (damaged state of the structure), EQ1 has the lowest acceleration spectrum and the pseudo-velocity spectrum. Indeed, the dynamic identification test at the end of the pre-peak phase of the hysteretic curve shows a 40% reduction of the natural frequency in the X-direction [48], corresponding a natural period of 0.4 s. For the post peak response, one may expect values of at least 0.5 s.

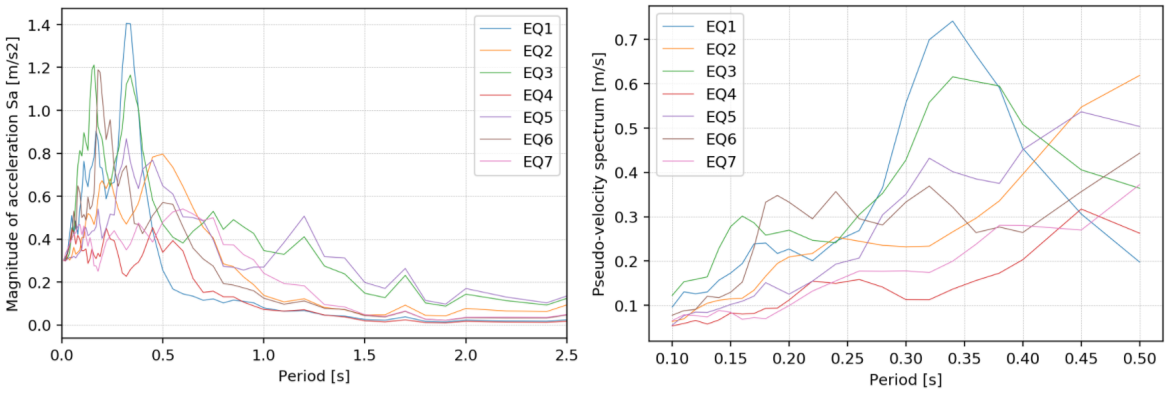

Figure 6.26: Acceleration spectra and pseudo-velocity spectra for the 7 earthquake records

In the figure below, the capacity curves of the two systems are compared. For both the modelling approaches, the trend of the point cloud is identified with a tenth order polynomial fitting.

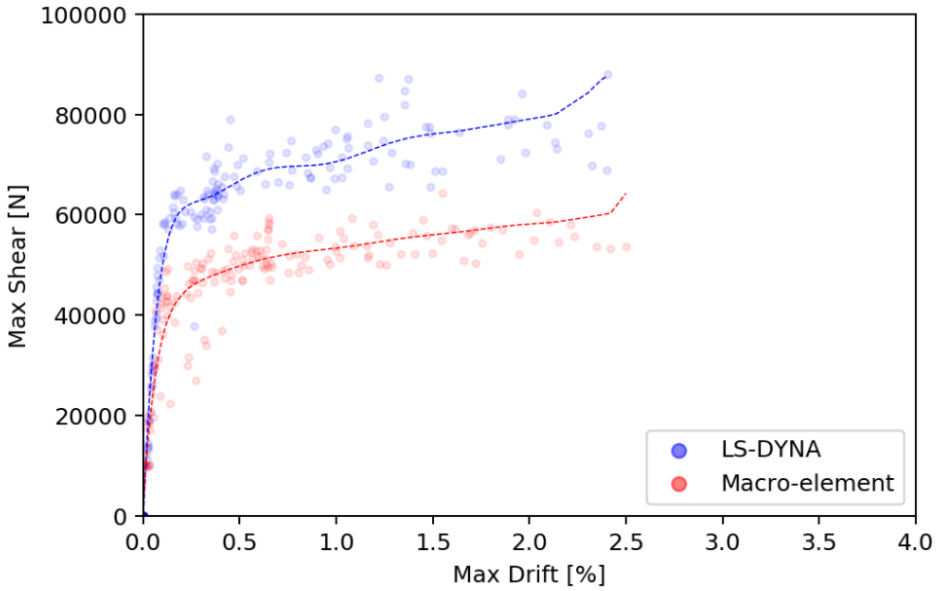

Figure 6.27: Point cloud backbone comparison - TUD-BUILD-1

The comparison shows that LS-DYNA capacity is always higher in average terms. The very initial stiffness is in good agreement (which was indeed spotted by the dynamic identification), whilst the macro-element reaches a first yielding point earlier than LS-DYNA, due to the sharp asymmetrical pier behaviour related to the flange-effect (see Figure 6.6). This is observed also in the quasi-static force-displacement curves comparison in Figure 6.21.

As an example of the dynamic behaviour predicted by the two modelling approach, the results in terms of displacement history, base shear force history and hysteretic behaviour are presented below. They refers to the excitation EQ1, with a PGA level of $0.40g$.

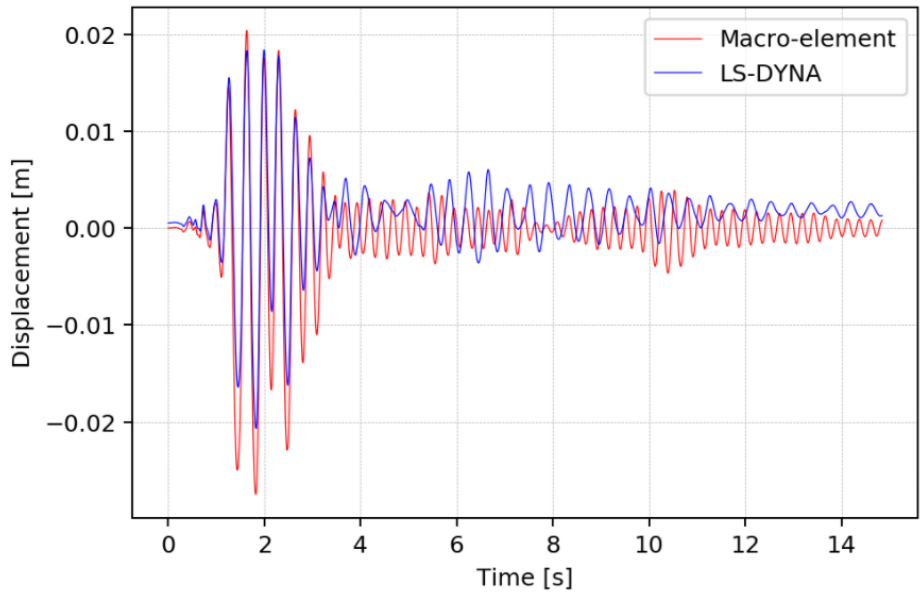

Figure 6.28: 2nd floor displacement history comparison - EQ1 - PGA 0.4g

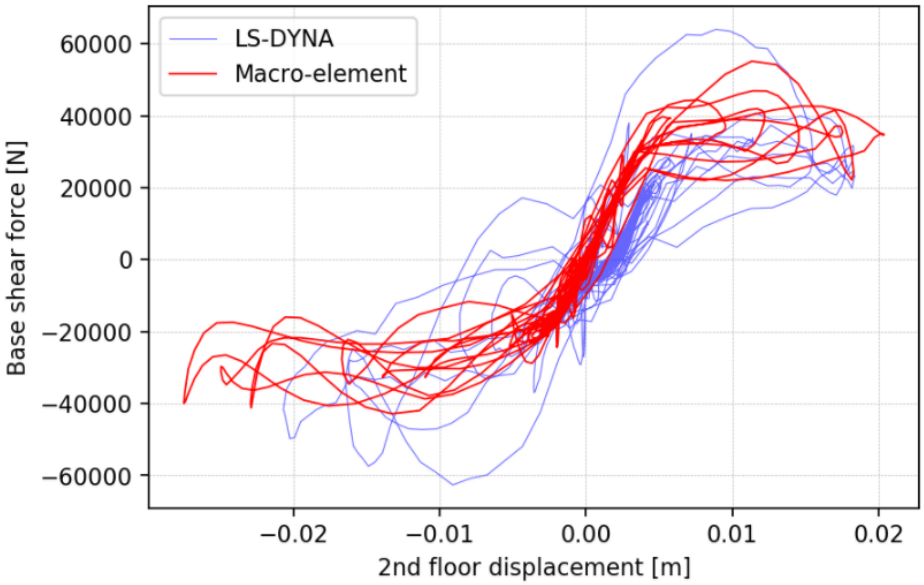

Figure 6.29: Hysteretic curves comparison - EQ1 - PGA 0.4g

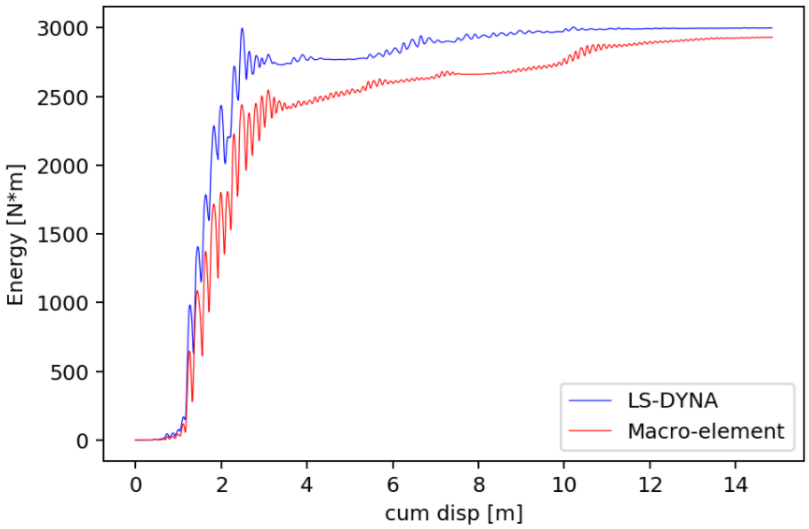

Figure 6.30: Energy dissipation - EQ1 - PGA 0.4g

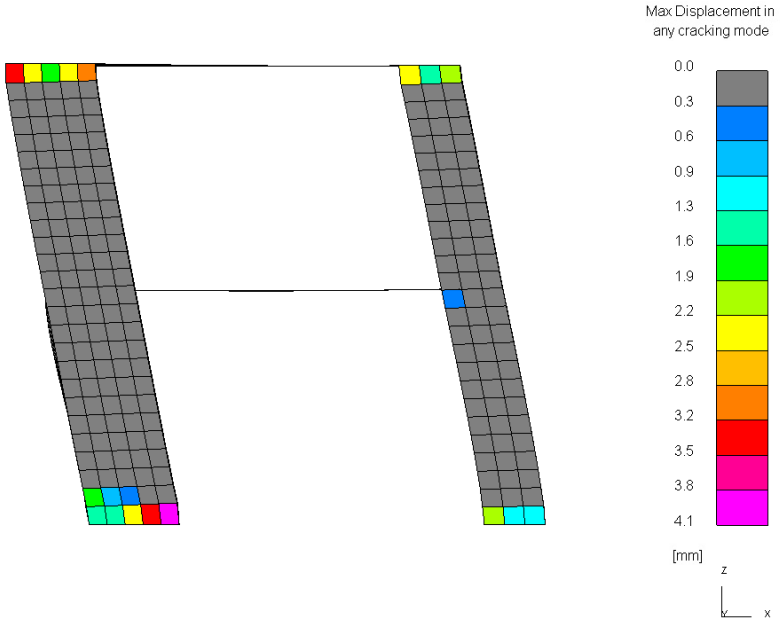

Figure 6.31: Damage state and magnified deformed shape at peak displacement - EQ1 - PGA 0.4g - Rocking mode of the four piers

As mentioned in Section 6.5, the short duration of the strong motion part of the input record is such that the structure deforms inelastically only for few cycles. Hence, the dominant rocking mode does not develop into a diagonal cracking mode with large residual deformations and conspicuous strength degradation. This can be observed from the self-centering hysteretic behaviour and the deformed shape in correspondence of the peak displacement. The macro-element displacement history in the linear range and strong motion part of the earthquake are in line with LS-DYNA. However, one may notice in the post peak displacement history, the accumulated damage leads to a much longer period of vibration respect to the macro-element model.

Another relevant example is related to EQ2, with a PGA level of $0.32g$. In this case, the high compression stresses recorded at the integration points in the pier corners exceed the compression strength of the masonry and leads to element erosion of the related shells (see element erosion in Section 3.3). In this way, the initial length of the pier, which appears on the capacity estimation in Equation 2.3 is reduced and changes significantly the response both during the strong motion part and during the post-peak response of the earth-

quake.

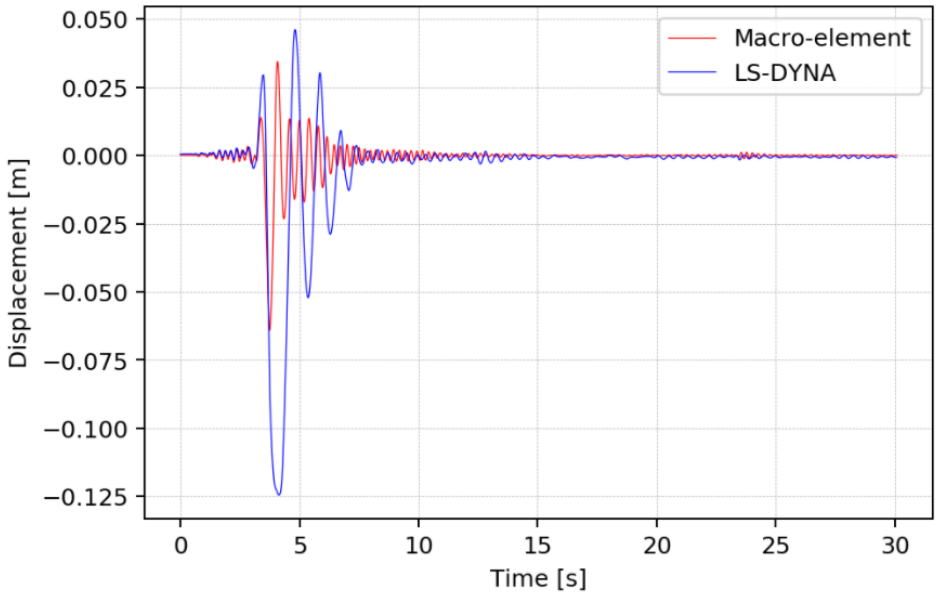

Figure 6.32: 2nd floor displacement history comparison - EQ2 - PGA 0.32g

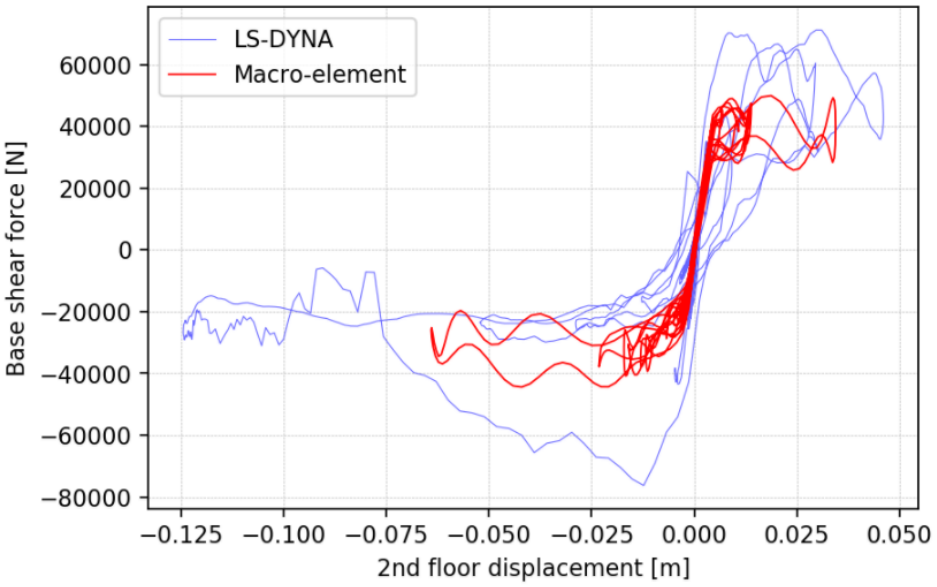

Figure 6.33: Hysteretic curves comparison - EQ2 - PGA 0.32g

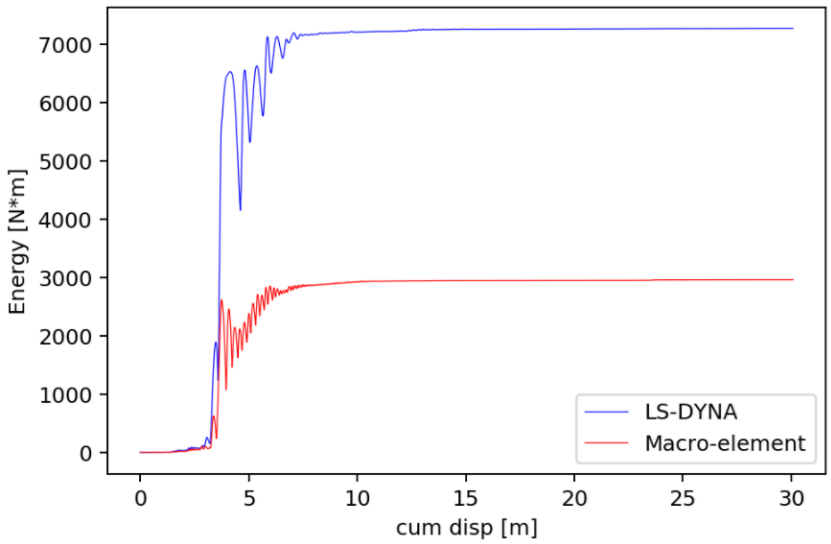

Figure 6.34: Energy dissipation - EQ2 - PGA 0.32g

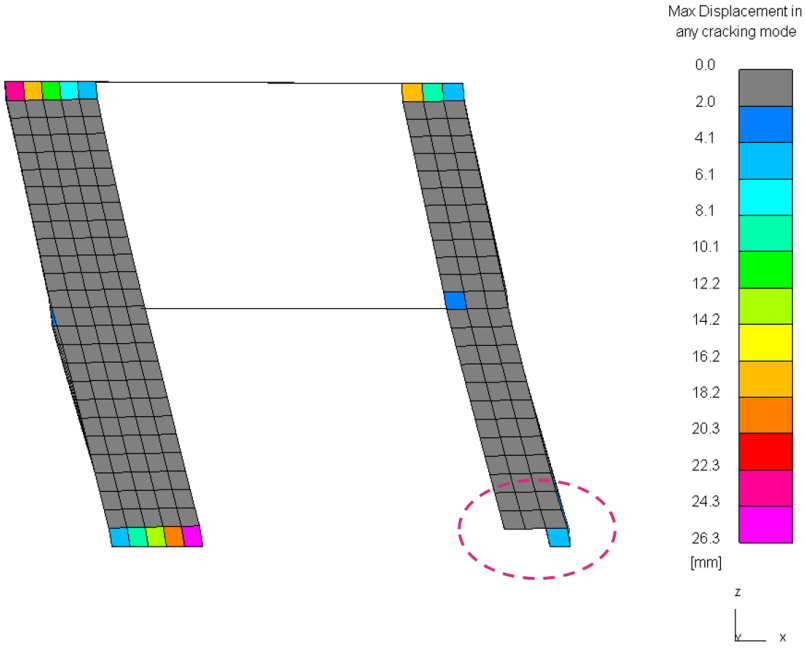

Figure 6.35: Damage state and magnified deformed shape at peak displacement - EQ2 - PGA 0.32g - Element erosion at pier corners due to toe-crushing

Conclusions and Recommendations

In this chapter, the proposed methodology and the numerical results are critically evaluated based on the initial assumptions. Next, recommendations for further improvements and future research are discussed.

Conclusions

Calibration

- The analytical formulations for the estimation of static stiffness and failure mechanism capacities are in line with the smeared plasticity numerical simulation and laboratory test results. For the considered slender component, the discrepancy with respect to LS-DYNA is within 10% for the two quantities. For the considered squat component, the discrepancy is within 5%.
- Quasi-static cyclic simulations on rocking components with LS-DYNA show a large underestimation (more than 100% discrepancy) of the internal energy history compared to laboratory tests. This is related to the different masonry hysteretic behaviour in compression. Since the dynamic validation tests are performed with LS-DYNA, it is favourable to calibrate the rocking hysteretic behaviour against the smeared plasticity force-displacement curves. The LS-DYNA cyclic response of squat component is instead in line with the laboratory tests.
- The genetic algorithm adopted acts as a reliable tool for the definition of an energy-based phenomenological description of the un-loading constitutive law of the rotational springs.
- The flag-shaped rule and elasto-plastic rule respectively for rocking and shear driven components produce results in line with LS-DYNA, during quasi-static cyclic loading, in terms of static stiffness, peak strength and energy dissipation.
- The asymmetric backbone self-centering system developed is suitable for capturing the flange effect of slender wall components interlocked to large transversal walls. Numerical simulations on wall components show that the flange contribution can be neglected for squat piers.

Component Validation

- Dynamic tests on shear driven component show good agreement between LS-DYNA and the macro-element, reaching collapse for drift limit exceedance with the same governing earthquake at the same PGA level. Point cloud backbone curves and energy dissipation are also comparable.
- Regarding the slender component, the macro-element approach predicts the same governing earthquake but at higher PGA levels. An impact-related phenomenon has been observed during the rocking behaviour of the LS-DYNA simulations. This has not been noticed in the calibration phase, proving the limitation of a rate-independent rotational spring model, calibrated with quasi-static loading protocols. This phenomenon is the reason of the dissipated energy discrepancy (up to 30%) for high drift levels. The sharp transition between elastic and post-yielding branch in the rotational springs is likely to cause the high discrepancy (up to 50%) for low inelastic drifts.

Benchmark building

- At large displacements, the laboratory prototype damage pattern turns into a diagonal cracking at the bottom portion of the large piers. This sequence of actions cannot be predicted by the lumped plasticity model for which, once the non-linearity is induced, the failure mechanism is stable.
- The capacity predicted by the macro-element is about 20% higher than the test results. The reason lies behind three different phenomena:

  - the assumption of fully fixed boundary condition at the second floor level translates into an upper bound estimation of the capacity;
  - the actual diaphragm deformability is likely to alter the vertical weight transferred to each pier during the analysis (assumed to be constant and equal to one fourth of the floor weight);
  - the out-of-plane accumulated damage is likely to deviate the behaviour from the simplified rigid body assumption that considers a the trapezoidal area with a fixed angle.

- NLTH LS-DYNA simulations show a self-centering behaviour, without the large residual deformation predicted by the quasi-static laboratory test. The typical short duration of the induced earthquakes is such that the structures usually oscillate inelastically only for few cycle, and do not absorb the amount of energy to develop a significant degradation of strength and stiffness.

- Even though in terms of first collapse occurrence the macro-element is less-conservative, the trend of the drift point cloud displays a good agreement between the two systems. The same governing earthquake is predicted by the two systems and collapse is reached for limit drift exceedance due to a rocking mechanism of the four piers.

- Due to the high compression stresses in the pier toe during tilting, crushing of masonry is observed in LS-DYNA simulations. This induces element erosion of pier shell elements, which significantly affects the response of the building in terms of period of vibration. In general, progressive damage in the smeared plasticity model produces evident discrepancy compared to the macro-element for high levels of drift.

- Analogously to the component tests, a large scattering is observed for the same PGA level. Housner intensity, spectral acceleration and arias intercity reflect the scattering, with the exception of the record EQ1. Even though linked to a severe spectral acceleration, it leads to the lowest drifts among all the records. This shows that the spectral acceleration at the elastic period is not fully reliable as an hazard parameter for high non-linear systems.

- In conclusion, the macro-element is able to predict the in-plane dynamic behaviour of URM wall components with reasonable accuracy, in terms of drift, capacity and energy dissipation. In the equivalent frame model, the response is qualitatively in line with the actual building results, in terms of failure mode and hysteretic shape.

Seismic hazard parameters

- A large scattering is observed in the maximum drift vs PGA trend for non-linear dynamic analyses. Three different physical intensity measures are considered for the investigation: Arias intensity, modified Housner intensity and spectral acceleration estimated at the elastic natural period. The outcomes clearly indicate the differences of the GM, at the same PGA level. The governing earthquake is the one characterised by the high values of the three physical intensity parameters. This is also reflected in the scattering of the energy dissipated by the components at the same PGA intensity.

Computational demand

- High-fidelity smeared plasticity models have proven to achieve accurate results in the blind-prediction tests performed in the laboratories of TU Delft and EUCentre. However, due to their high computational demand, they do not seem suitable for large-scale calculations, like the fragility curves development framework. The analyses performed with the proposed macro-element approach turned out to be faster by two orders of magnitude compared to the smeared plasticity models.

Recommendations

Hysteretic rules

- Given the outcomes of the dynamic analysis performed on slender components and the prototype building, it is recommended to include new parameters in the flag-shaped hysteretic rule proposed for rocking systems, to control the transition from elastic to plastic branches. In this way, one may expect the inelastic response at low inelastic drifts to be significantly improved. In addition, the convergence of the numerical algorithms may benefit as well.
- Even though it is not observed at the component level, a low-intensity pinching phenomenon has been observed in the response of the assembled structure. It is recommended to investigate the response of the macro-element including pinching parameters both in the rocking and the shear hysteretic material models.
- The genetic algorithm presented in Appendix A may be used for the calibration of damaged related parameters. In particular, although not directly observed in most of the component laboratory tests, strength degradation might be adopted to simulate the element erosion techniques of the smeared plasticity software.
- In the present work, a drift-based limit state assessment has been adopted. In the case of a strength-deteriorating model, it is recommended to investigate a limit state associated with a certain loss of capacity under repetitive loading.

Soil-structure-interaction

- Given the computational efficiency of the approach, further research may focus on the soil-structure-interaction under dynamic loading. Additional degrees-of-freedom may be calibrated to capture the non-linear soil behaviour at the building foundation level. The natural period is likely to elongate and the building response may change significantly when subjected to given a free-field ground motion in the unbounded domain.

Capacity calibration

- Further research is necessary to achieve a more accurate calibration of the non-linear spring capacities. The simplified trapezoidal rigid body assumption leads to an overestimation of the building strength. An extensive numerical study may be performed to identify the set of parameters that influence the actual additional weight provided by the flange effect.
- Alternatively, machine learning techniques may be adopted, using the existing analyses database as a learning set to train the algorithm. This may also contribute to a less deterministic definition of the flange effect in building codes. In this framework, the learning dataset may be used also to train the algorithm for a more sophisticated estimation of the β parameter in the flag-shaped hysteretic rule, based on the actual wall properties: geometry, boundary conditions and mechanical parameters.

Equivalent-frame approach

- It is recommended to further improve the equivalent-frame model by introducing an axial DoF for the piers. This may be dynamically coupled to the horizontal DoF's and hence, extends the applicability of the approach to structures sensitive to the vertical component of the ground motion.

A

Appendix

A.1. Multi-objective Genetic Algorithm

Being phenomenological rather than based on mechanics principles, all these models rely on some parameters that make behaviour experimentally observed, but whose physical meaning is not immediately recognisable. An important phase prior to the seismic analysis is thus the calibration of the non-linear elements modelling critical components.

Calibration is generally carried out by looking for the set of model parameters that, inserted in the model, fit the response measured in experimental tests as close as possible. Often the calibrations tests are quasi-static cyclic tests following specific loading protocol, developed to give a reliable estimate of the cyclic deformation demand of the considered structural system.

For this purpose, an automatic multi-objective calibration algorithm [18] has been adopted. Calibration or parameter identification of a numerical model means finding the set of parameters $\widetilde{p}$ such that the computed response given by a simulation of a test $y_c(p)$ is as close as possible to the experimental response y_{exp}. When N_T calibration tests are performed, this implies solving the optimization problem:

$$\widetilde{p} = arg\min_{p \in P} \{\omega_1(p), ..., \omega_{N_T}(p)\} \tag{A.1}$$

where $\omega_1(p) = \frac{||y_{exp,i} - y_{c,i}(p)||}{||y_{exp}||}$ is the discrepancy function measuring the inconsistency between the experimental and computed quantities for the i-th test, and P the set of all possible parameters combinations. The minimization of ω_i may be accomplished by using different optimization methods. In the present case, the solution of Equation A.1 is obtained by means of the non-dominated Sorting Genetic Algorithms II, NSGA-II, coupled to Linear Ranking based on domination and crowding distance, and Blend-α crossover.

In the context of multi-objective optimization, the concept of Pareto optimality replaces the usual notion of optimality. A solution is referred to as Pareto optimal if it is not dominated by any other solution. The ensemble of all Pareto optimal solutions is said Pareto Front PF, and it represents the general solution of Equation A.1. At the end of the analysis, a unique compromise solution p_{compr} may be extracted from the Pareto Front, according to the rule:

$$p_{compr} = arg\min_{p \in PF} ||\omega(p) - \omega_{utopia}|| \tag{A.2}$$

where $\omega(p) = \left[\omega_1(p), ..., \omega_{N_T}(p)\right]^T$ and ω_{utopia} is the vector of the minimum discrepancy.

A.2. Calibration of the flag-shaped hysteretic model

In this appendix, the outcomes of the optimization algorithm used for the calibration of the β coefficient of the flag-shaped rule are presented. The material mode relies on 4 parameters: My, $K1$, $K2$, and β. While first

3 are fixed, since computed based on the mechanics formulation of Chapter 2, the β parameter reflects the energy dissipation coming from the sliding at the joint

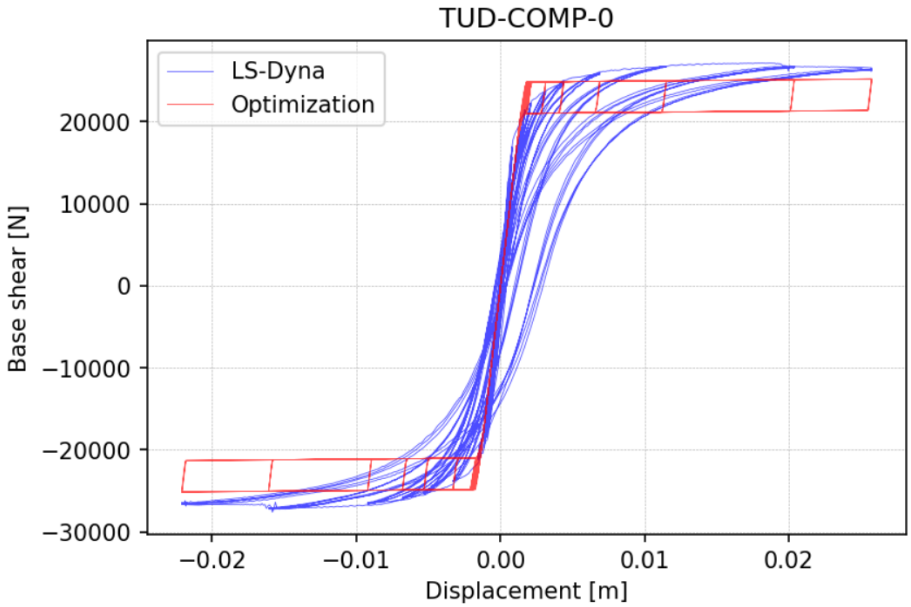

Figure A.1: Optimization compromise for TUD-COMP-0

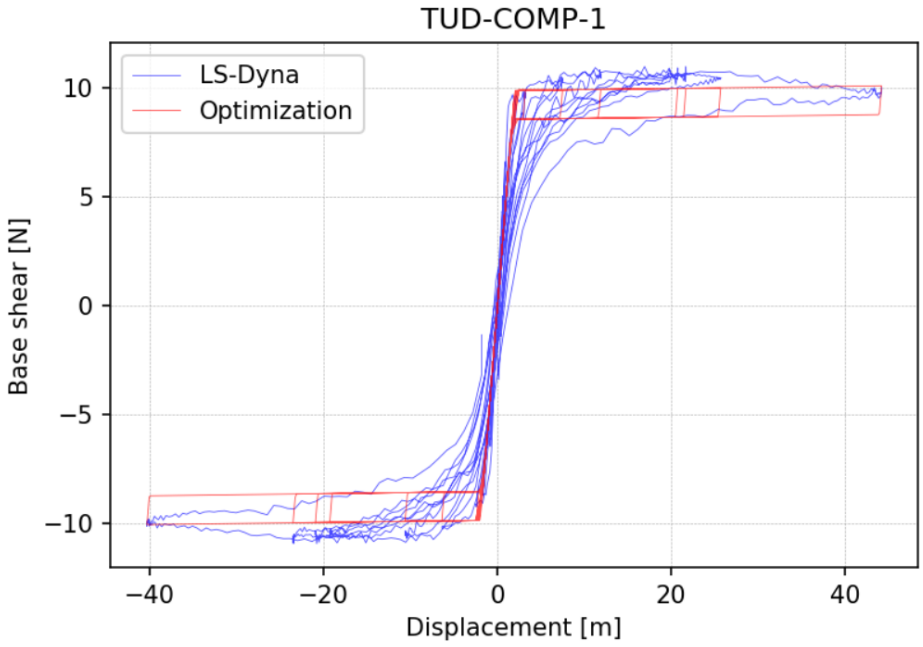

Figure A.2: Optimization compromise for TUD-COMP-1

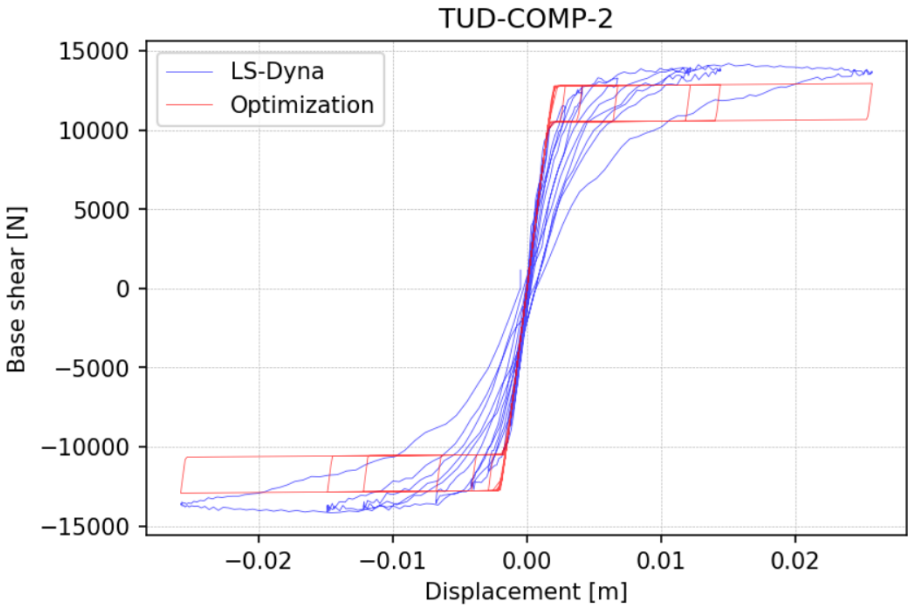

Figure A.3: Optimization compromise for TUD-COMP-2

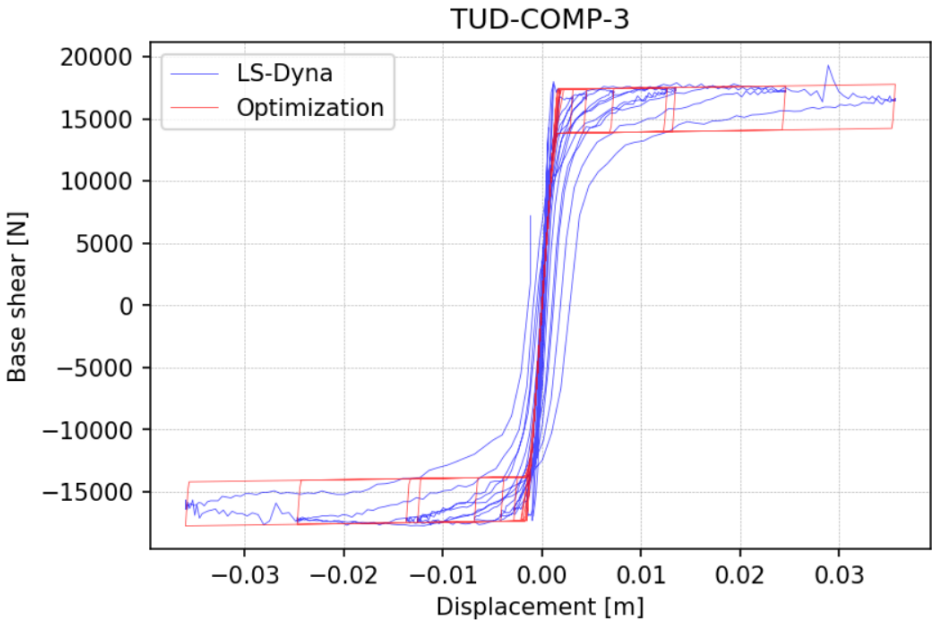

Figure A.4: Optimization compromise for TUD-COMP-3

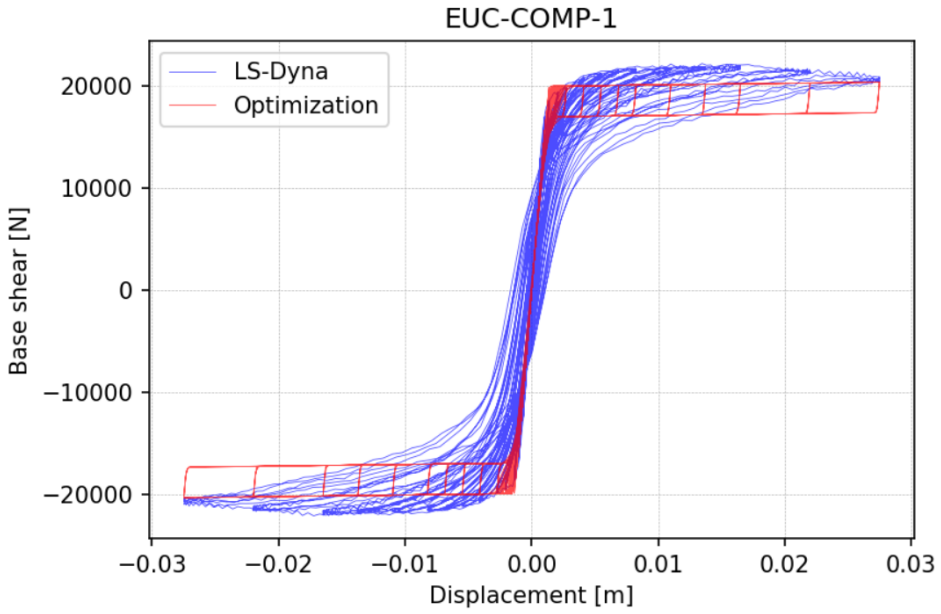

Figure A.5: Optimization compromise for EUC-COMP-1

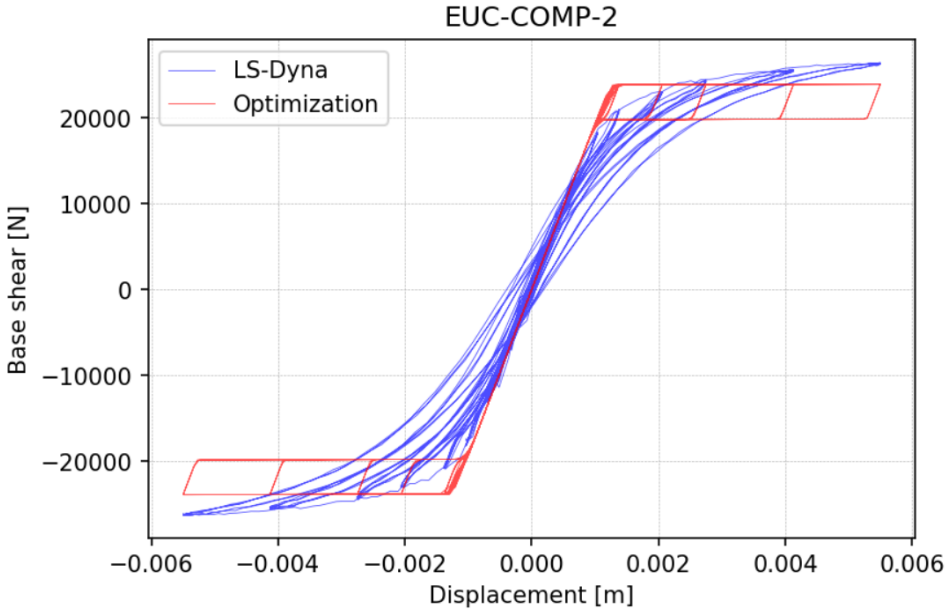

Figure A.6: Optimization compromise for EUC-COMP-2

B

Appendix

B.1. Earthquake records

The ground motion for the point cloud analyses are selected from a database of over 4000 accelerograms, which has been set up for the non-linear dynamic analyses, by combining recordings from the NGA1 [17], European and Groningen databases [8]. The moment magnitude, epicentral distance and 5-75% significant duration for each accelerogram has been obtained/calculated, and it has been ensured that they cover the range of these parameters used in the probabilistic risk assessment for the Groningen field. In particular, the magnitude range has been taken to be between 3.5 and 6.5, and epicentral distances up to 60 km have been used.

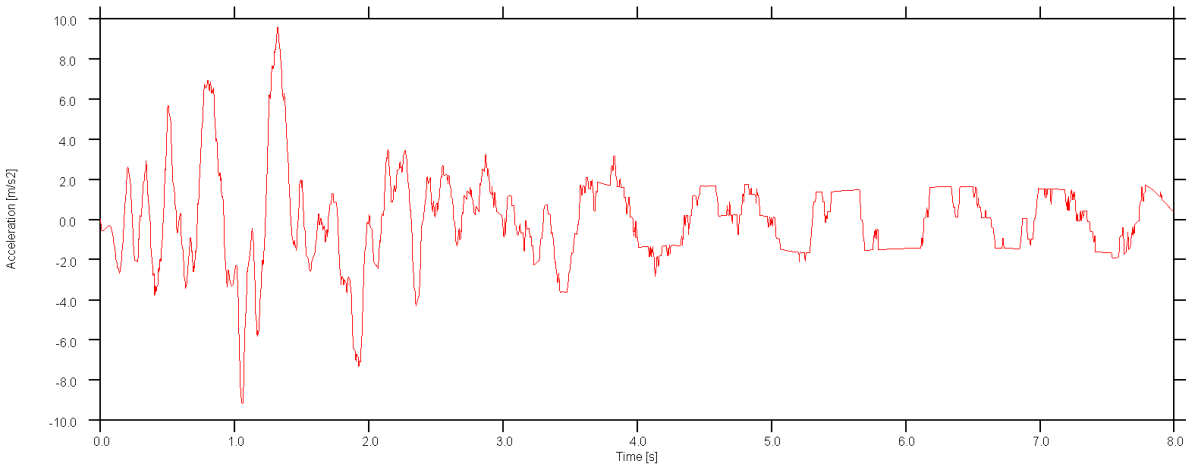

Figure B.1: Earthquake record 0

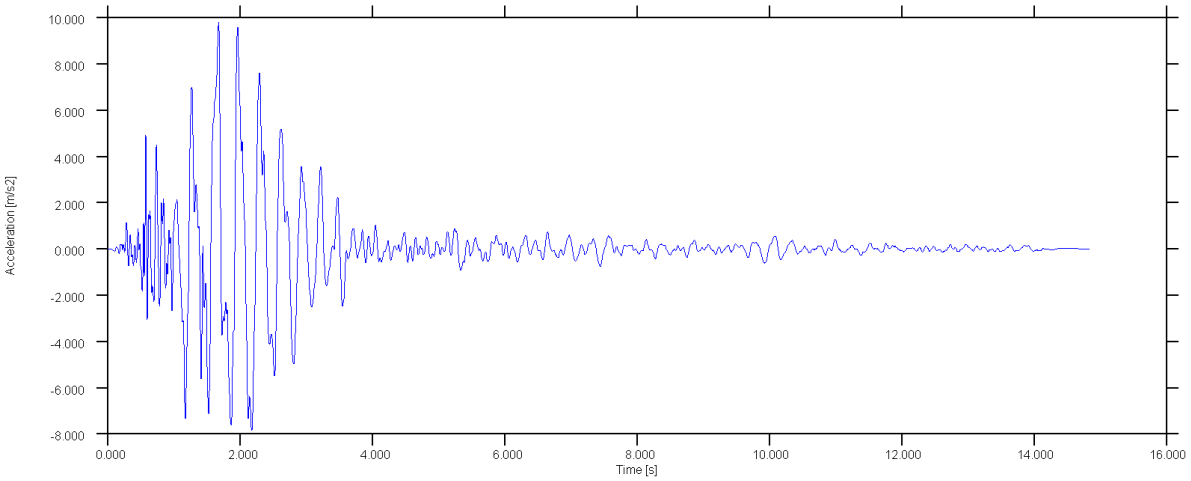

Figure B.2: Earthquake record 1

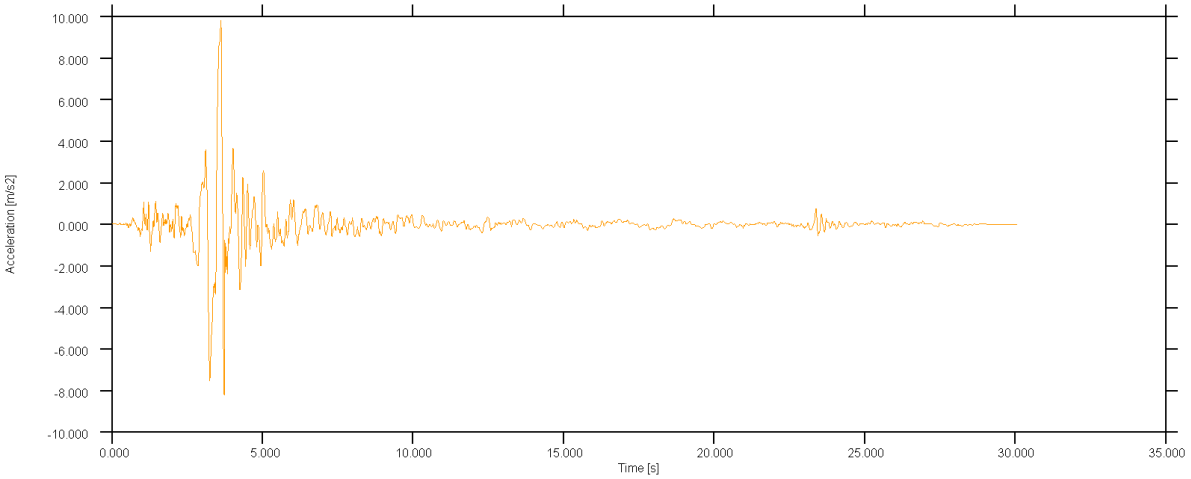

Figure B.3: Earthquake record 2

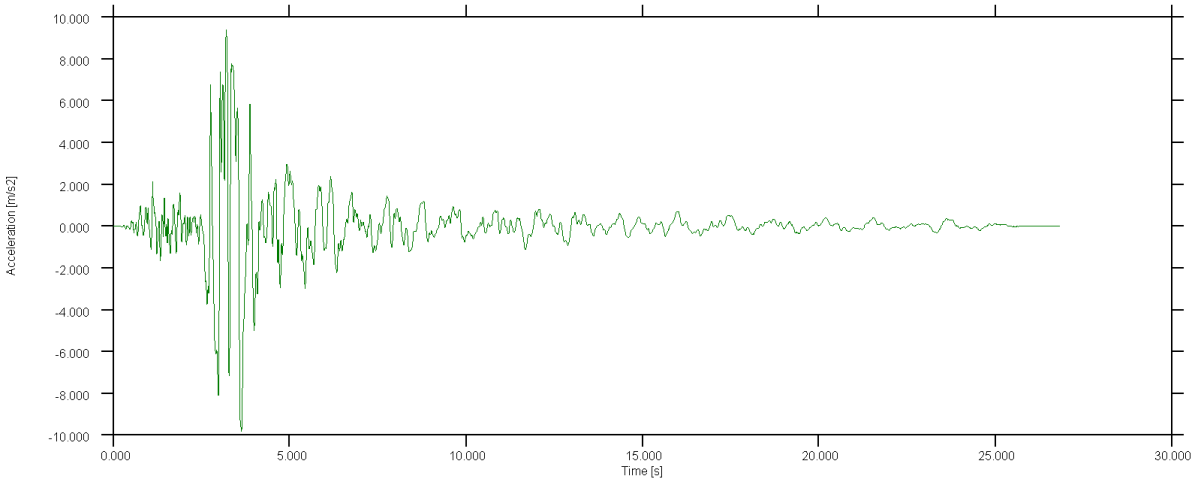

Figure B.4: Earthquake record 3

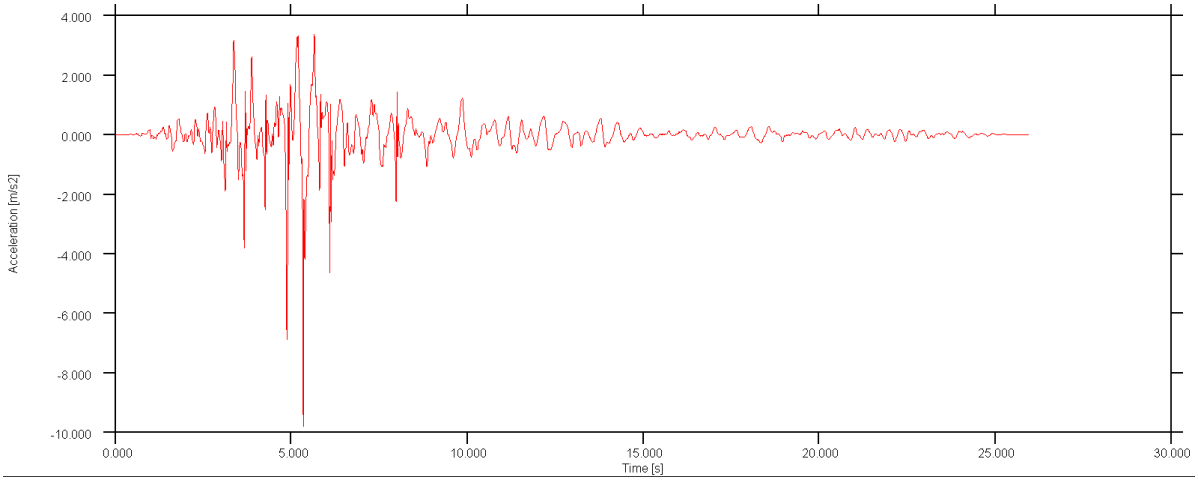

Figure B.5: Earthquake record 4

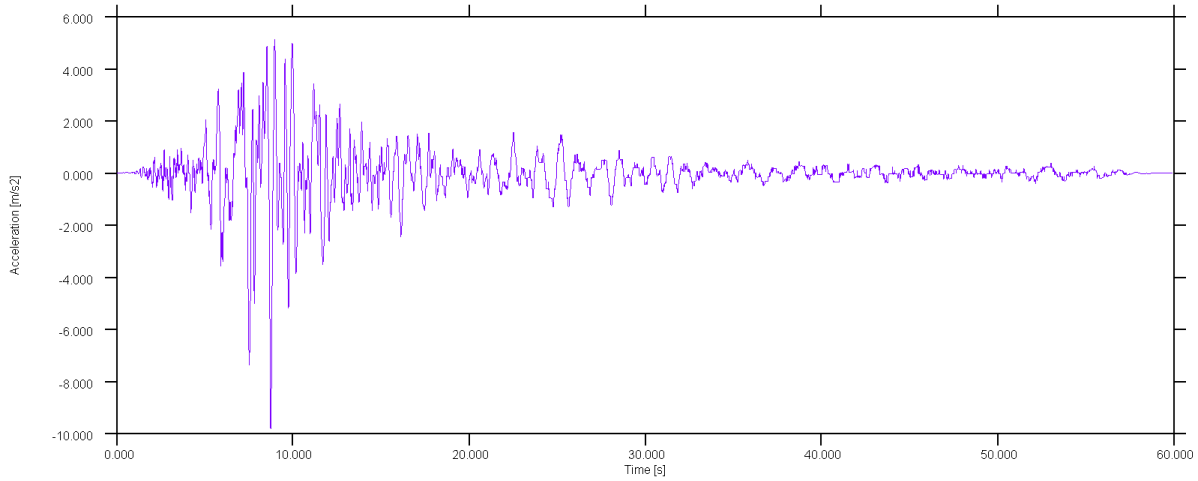

Figure B.6: Earthquake record 5

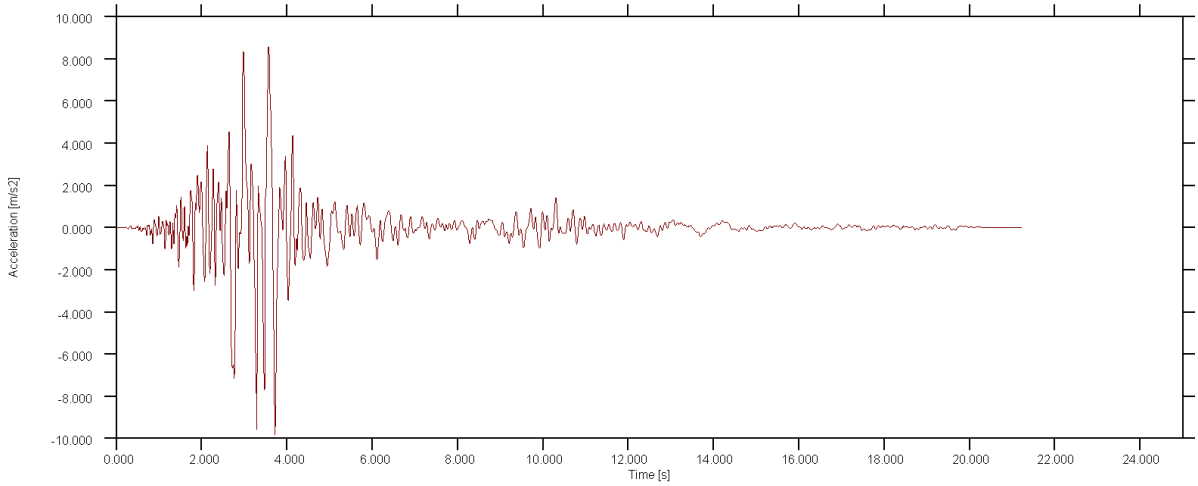

Figure B.7: Earthquake record 6

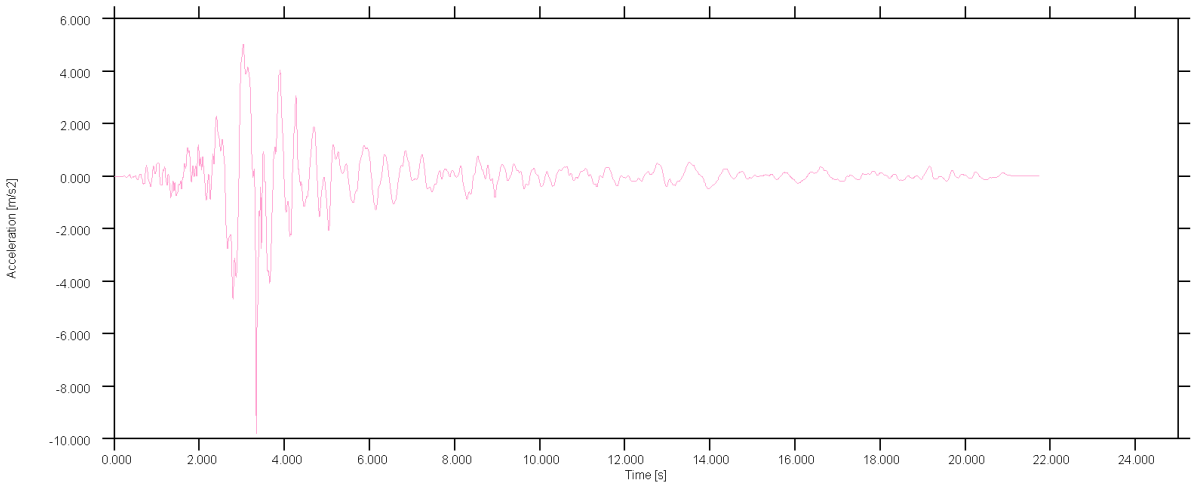

Figure B.8: Earthquake record 7

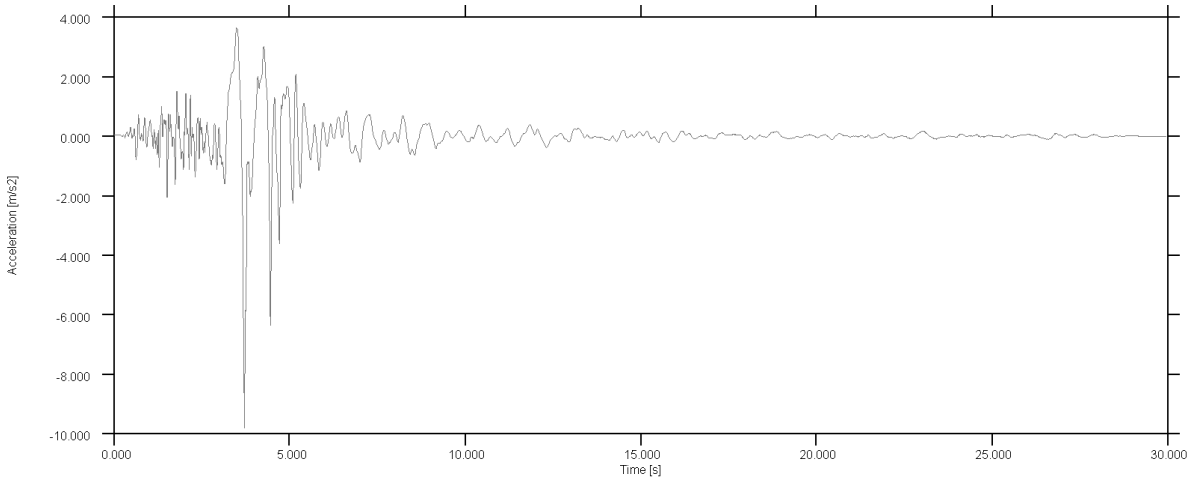

Figure B.9: Earthquake record 8

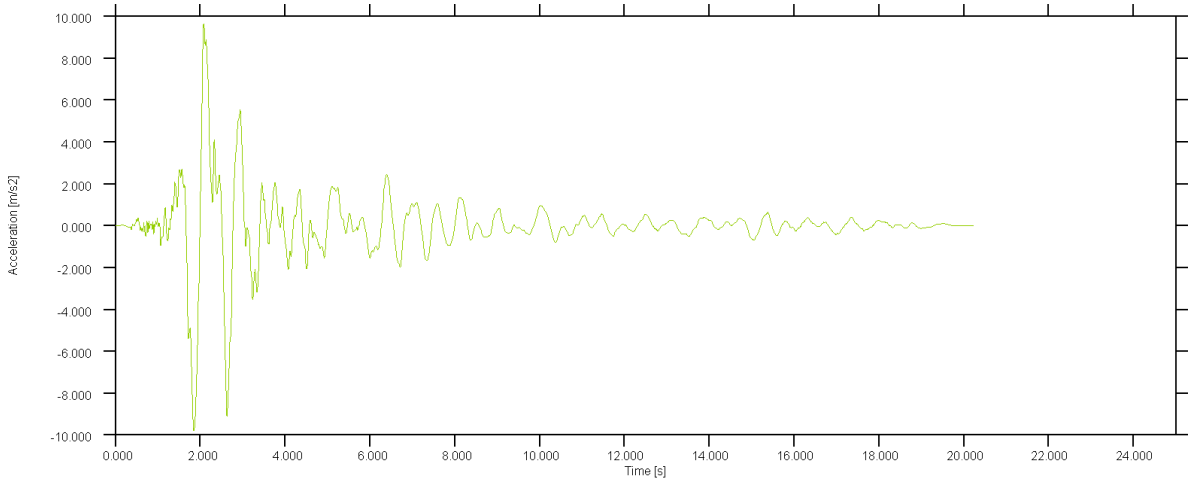

Figure B.10: Earthquake record 9

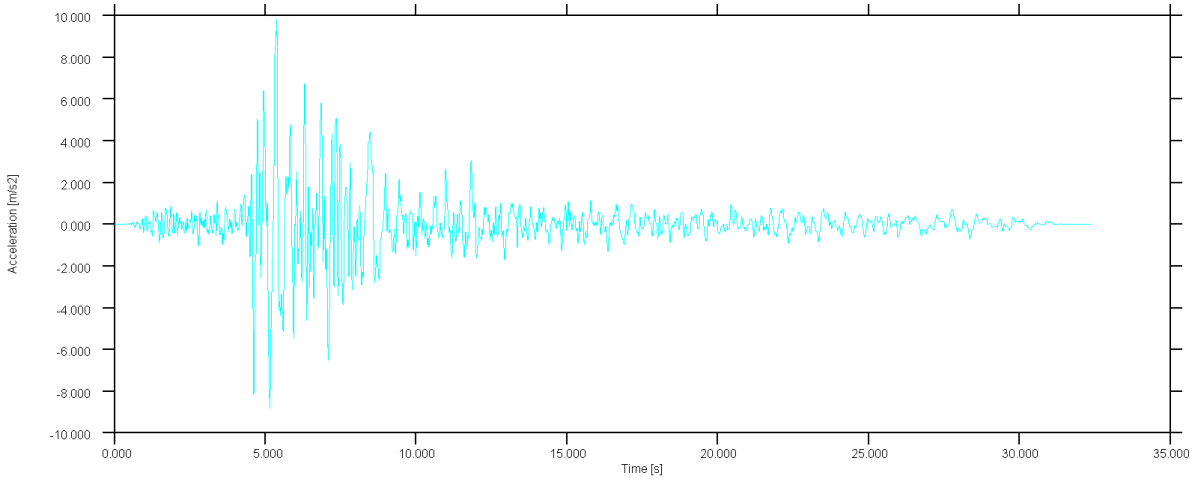

Figure B.11: Earthquake record 10

B.2. Quasi-static loading protocol

In the figure below, the reference loading protocol adopted for the quasi-static tests in the laboratory and numerical simulations is presented. For each test, the curve is scaled in the x-axis in order avoid the activation of inertia forces. Analogously, the curve is scaled in y-axis to ensure the deformation of the systems into the inelastic range.

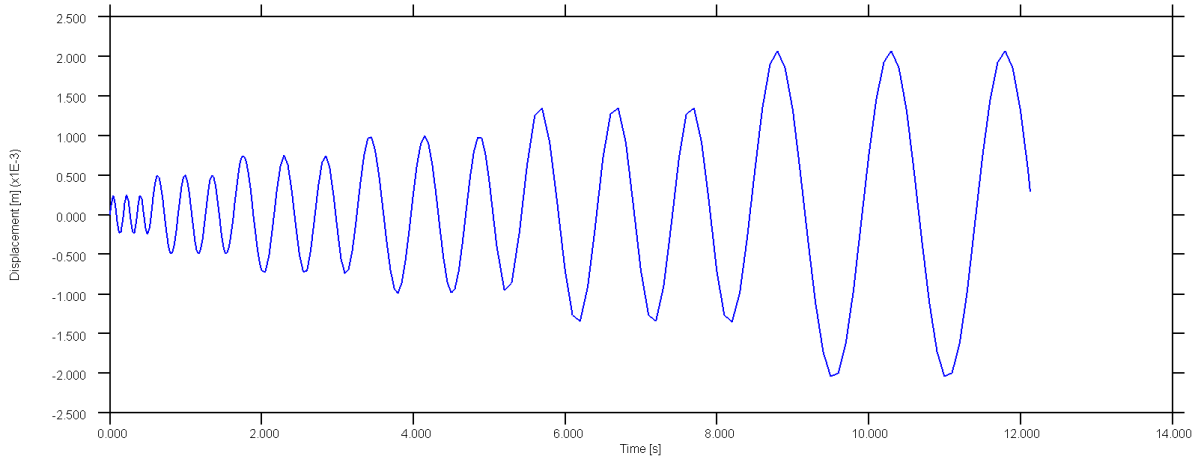

Figure B.12: Loading protocol for quasi-static analyses

C

Appendix

C.1. Impact of the vertical component of the ground motion

It is known that for shallow earthquakes, the ratio vertical to horizontal PGA of the ground motion is close to the unit, differently from the typical tectonic events, in which the S-waves predominate on the P-waves. This has been indeed observed in the signal recorder by the accelerometers located near Westeremden on the 16th of August, 2012 (Figure C.1).

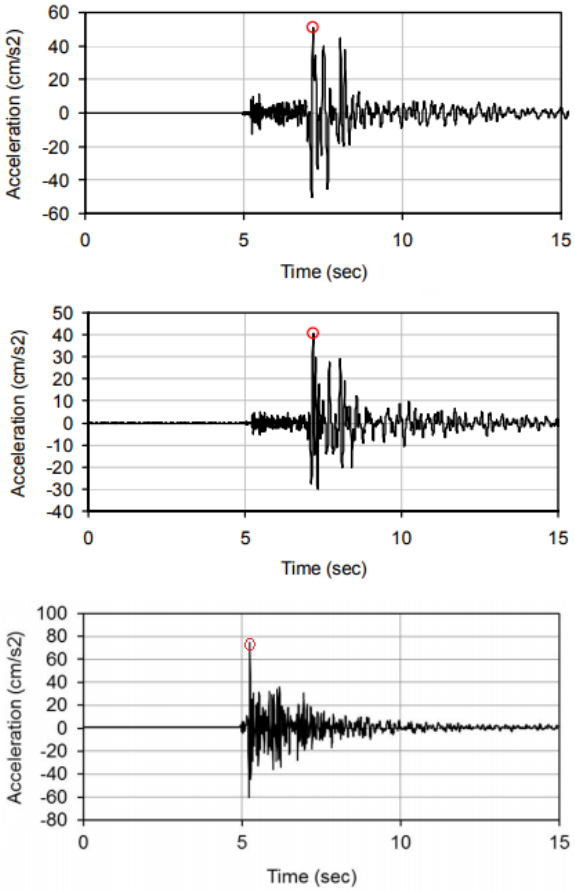

Figure C.1: Radial, transversal and vertical components recorded on 16th of August, 2012 near Westeremden [25]

However, for several reasons, the structural systems under consideration are not considered to be sensitive in the vertical direction:

- The buildings are designed to resisted the vertical gravity loads;
- The system does not include horizontal or nearly horizontal structural members spanning 20 m or more [15];
- The system does not include horizontal or nearly horizontal cantilever components longer than 5 m [15];

In addition, the URM structure could be potentially affected in case of lose floor to wall connections, unable to prevent the uplift of the diaphragm, or in case of a loose soil supporting the foundation system. However, as mentioned above, in the present work, connection failure, as well as soil structure interaction are not been investigated.

Despite of the reasons discussed here, it has been decided to carry out a sensitive study on the effect of vertical component of the ground motion on the response of an URM building prototype. It is the one presented in Chapter 6. First, the analysis is performed applying the acceleration history on in the weak direction of the buildings (i.e. only horizontal component). Then, the same analysis is performed, including also the vertical component of the accelerogram. The results are presented in Figure C.2.

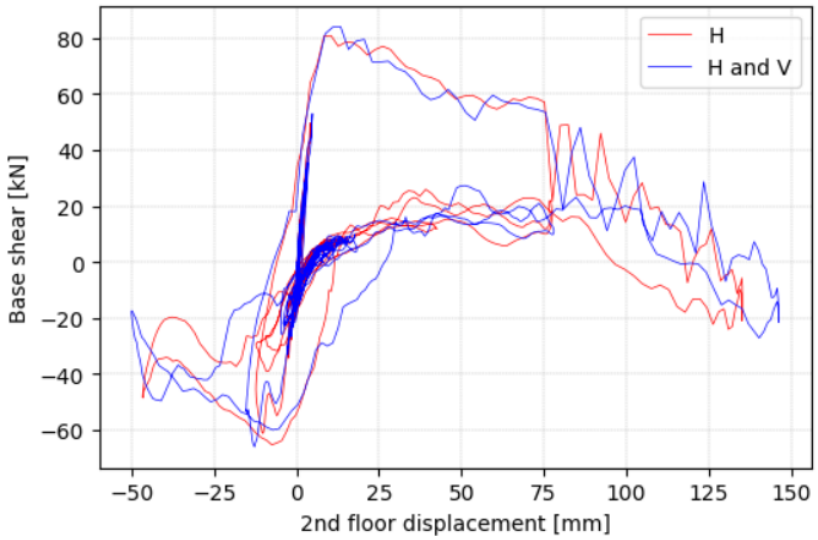

Figure C.2: Global hysteresis comparison: horizontal GM component of the only, and both horizontal and vertical GM components

It can be noticed that although the PGA level in the vertical direction is up to $3g$, and the ratio vertical to horizontal around $0.6g$, the response seems not to be affected by the introduction of the vertical motion. In particular, the same failure mechanism is induced (i.e. rocking mode - Figure C.3) and while the capacity and maximum drift achieved differ from less than 5% (Figure C.2).

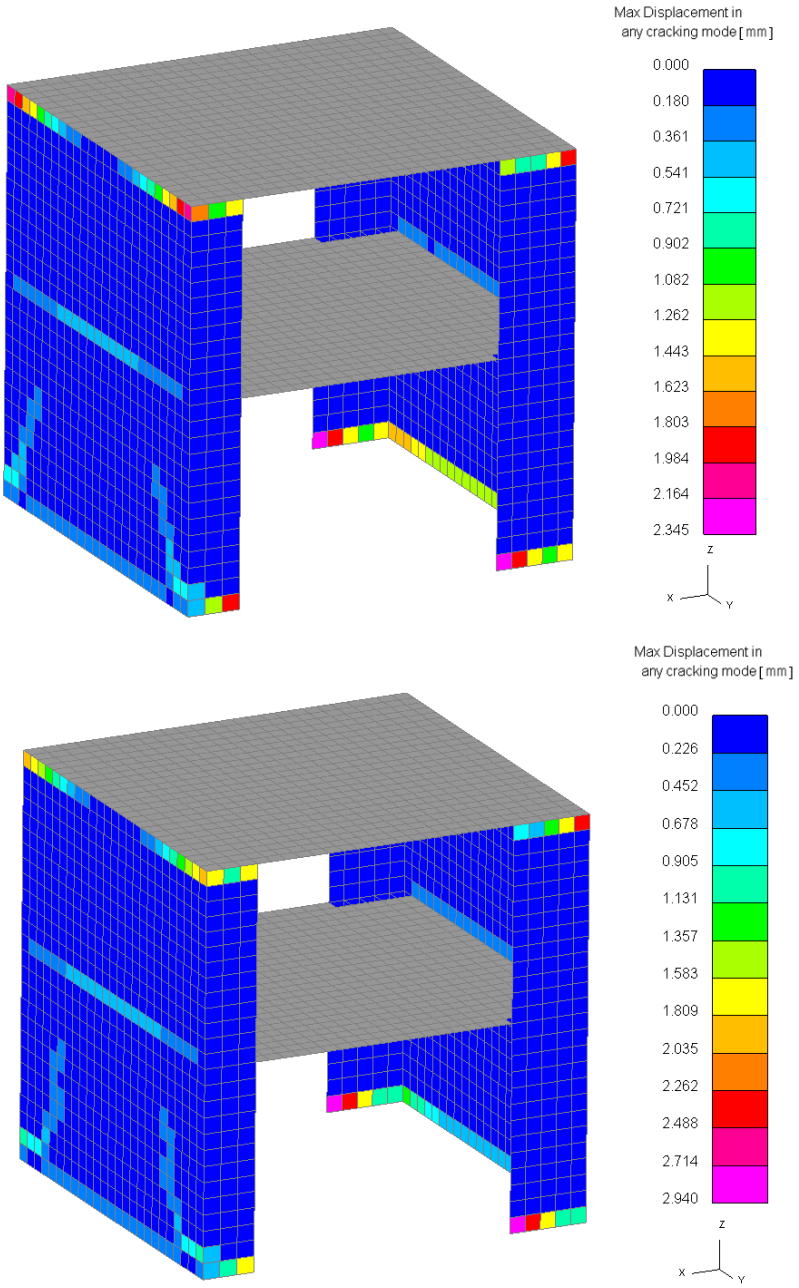

Figure C.3: Damage state at peak displacement due to pier rocking for H GM only (top) and for H and V (bottom)

D Appendix

D.1. Sinusoidal input motion

The slender pier specimen modelled with shell elements and lumped plasticity, described in Section 5.1 is subjected to a sinusoidal input acceleration signal order to assess the impact of the shock-effect observed in Section 5.3.1 and described in [46]. It is a short-duration, high-velocity contact in a dynamic domain able to induce short-duration large-amplitude accelerations, both in horizontal and vertical directions (horizontal acceleration spikes and vertical acceleration spikes).

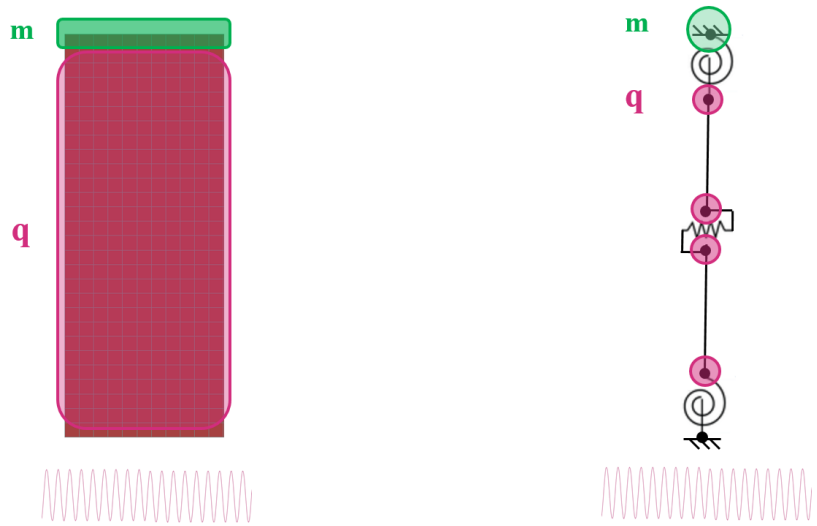

Figure D.1: Sinusoidal input motion test on a slender wall component

This has not been observed in the QS tests performed at EUCentre and Pavia [3]. Being the displacement applied with a very low rate, inertia effects are prevented.

Firstly, the specimen in subjected to a sinusoidal acceleration record, with a low amplitude, such that the response of the systems remain linear throughout the duration of the test. The output in terms of acceleration history recorded at the top node of the specimen is presented below.

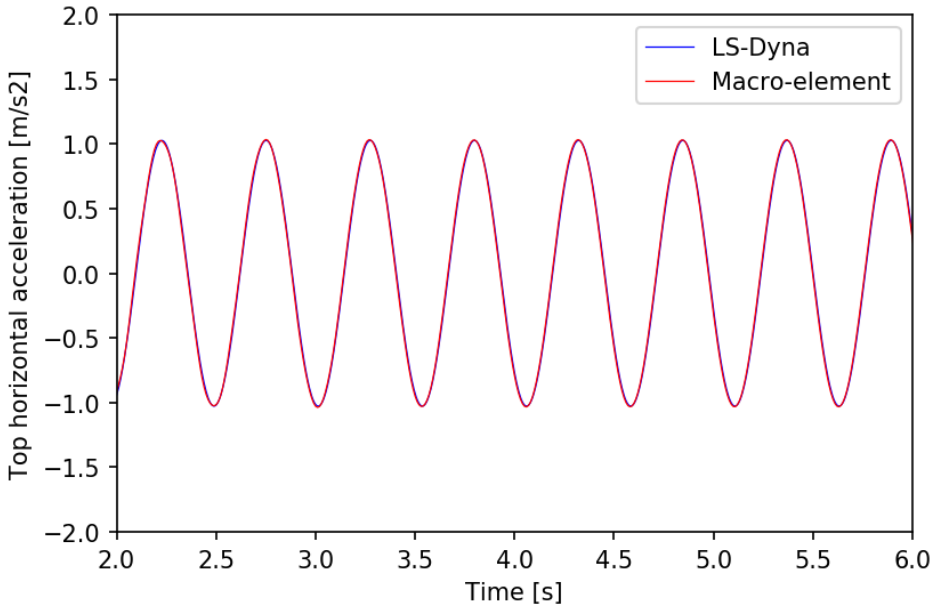

Figure D.2: Acceleration history comparison - Low intensity sinusoidal input motion

In the linear-range, the response of the two systems in really close. The rocking mode has not developed yet, therefore, no impact effects can arise at the bed-joint locations. In addition, the same signal is scaled up in such a way to induce the non-linearity in the system. The outputs in terms of displacement, base shear force, acceleration history and energy history are presented below.

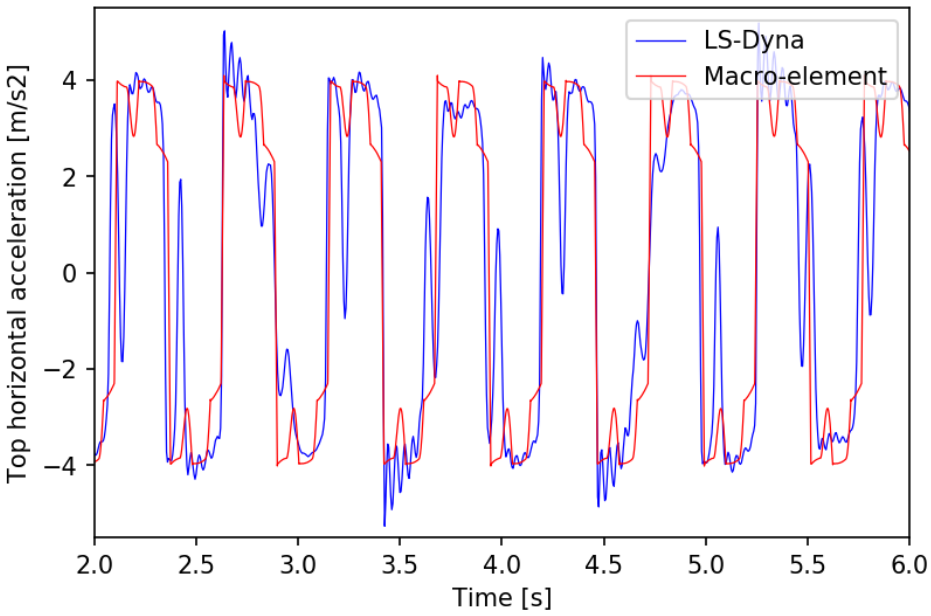

Figure D.3: Acceleration history - High intensity sinusoidal input motion

From the top node acceleration history of the LS-DYNA model, it is evident the presence of high frequency spikes of horizontal acceleration. These are due to the impact phenomenon at the mortar joint location, due to opening and closing of the gaps.

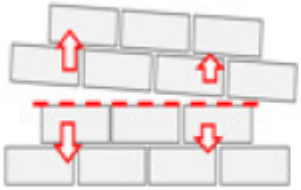

Figure D.4: High-frequency impact phenomenon due to bed-joint opening and closing

The same high frequency vibrations can be noticed in the vertical acceleration history recorded at the top of the shell element wall. Of course, these vibrations cannot be captured my the macro-element mode. The width of the pier is not explicitly introduced in the model. For such a purpose, one would need a multi-spring fiber model, with contact springs.

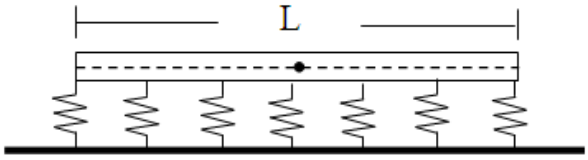

Figure D.5: Multi-spring fiber based model

However, one may realize that, with such a representation, the computational demand would increase significantly. In addition, the infinitely stiff boundary conditions enforced in the model are likely to overestimate this phenomenon. In a real system, neither the bottom, nor the top of the wall are fully fixed, due to the presence respectively of the soil and the upper floor.

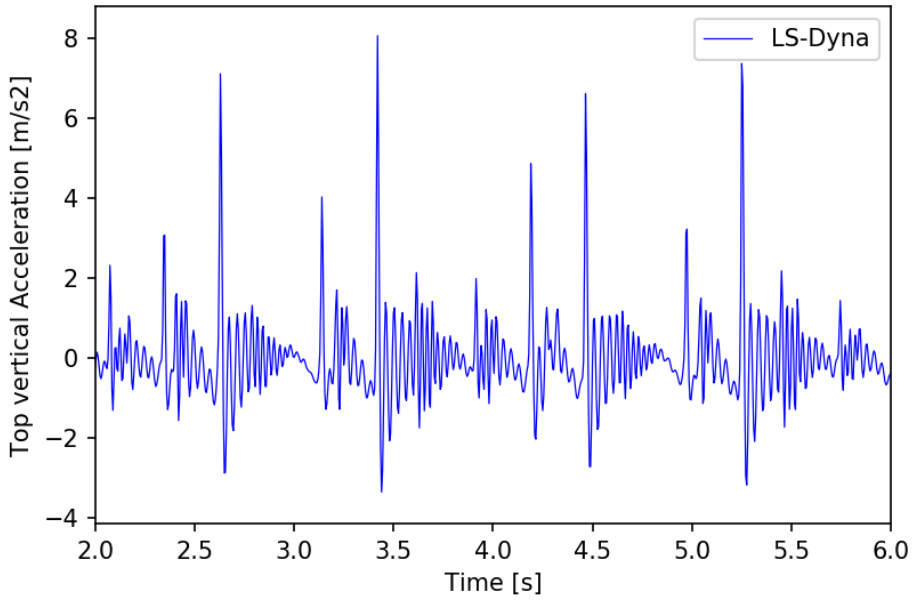

Figure D.6: Vertical acceleration spikes due to impact effect - High intensity sinusoidal input motion

Naturally, the base shear force history of the LS-DYNA model presents the same frequency content as the horizontal acceleration, leading to spurious capacity values.

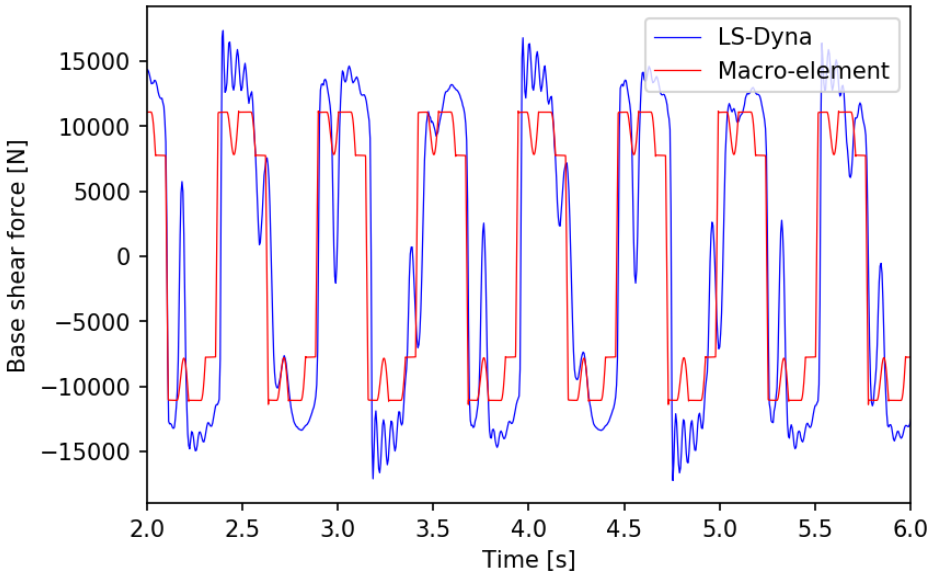

Figure D.7: Base shear history - High intensity sinusoidal input motion

In [46], the results of the full scale Knoxville laboratory test on a reinforced concrete wall are presented. It is an in-plane uni-axial dynamic test. From the top acceleration history displayed below, it is clear the gap contact phenomenon influences the response: a short duration mode is super-imposed to the dominant larger rocking mode.

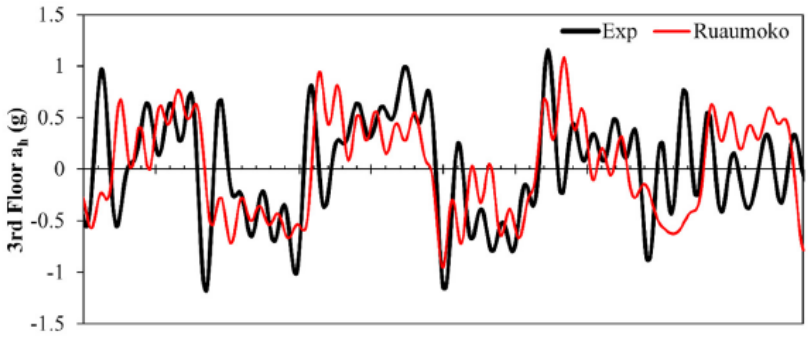

Figure D.8: Horizontal acceleration spikes observed for Knoxville dynamic test on RC rocking wall [46]

E

Appendix

In this appendix, the damage state comparison is presented, for pier components with and without flange.

E.1. Flange effect in slender component

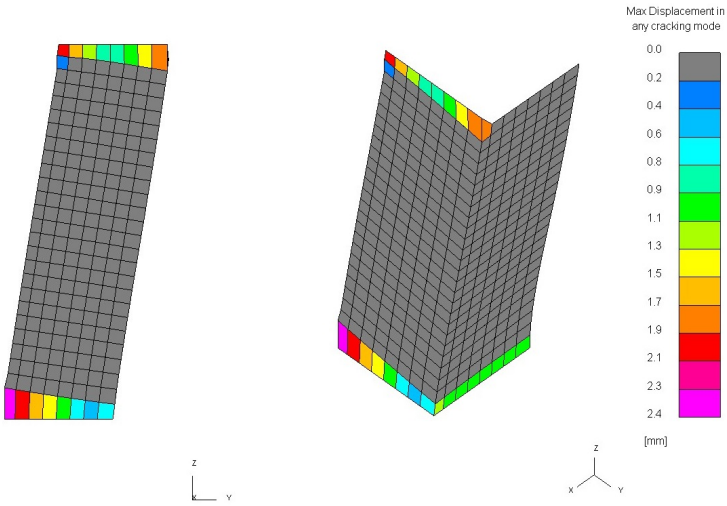

Figure E.1: Average acceleration method [19]

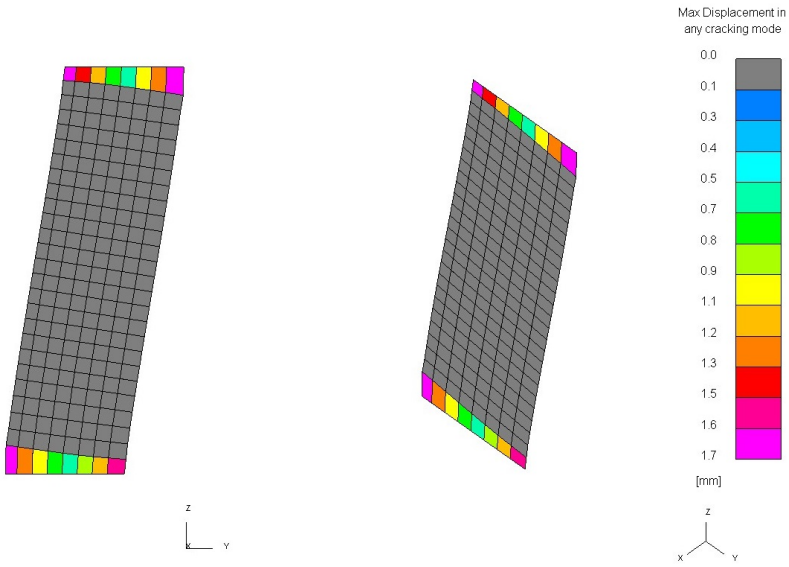

Figure E.2: Average acceleration method [19]

E.2. Flange effect in squat component

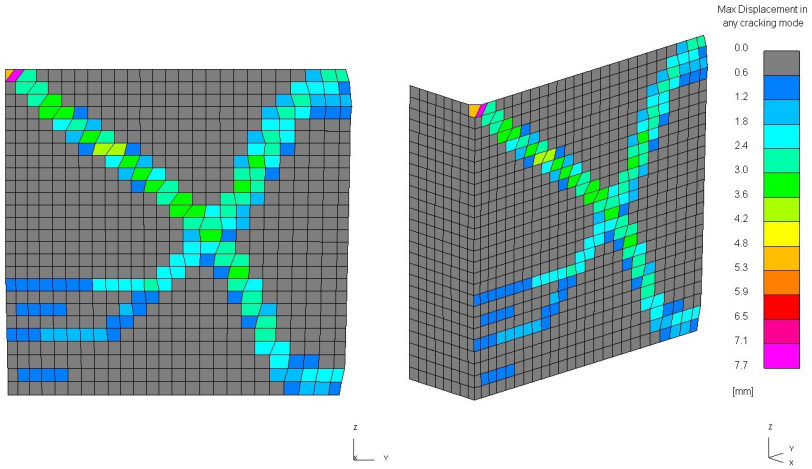

Figure E.3: Average acceleration method [19]

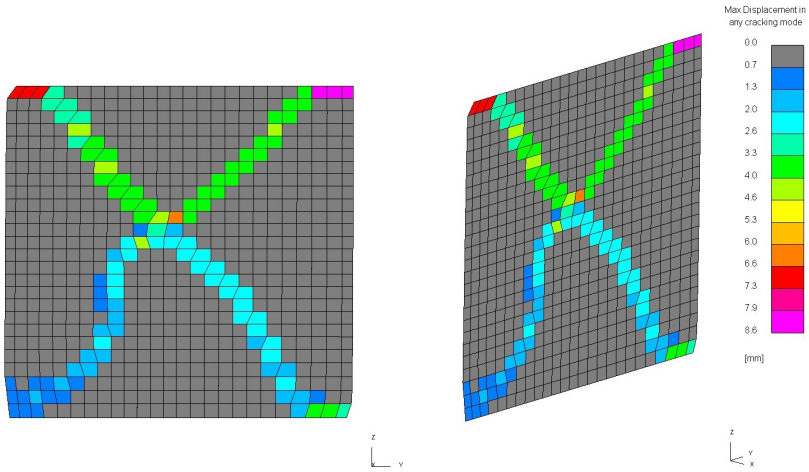

Figure E.4: Average acceleration method [19]

Bibliography

[1] Arup. *Handbook: 1. Structural Upgrading –Engineering Design Catalogue level 2-3 measures Assessment & Concept design.* Arup, Groningen, The Netherlands, 2014.

[2] Arup. Blind prediction modelling and analysis – tud build. Technical report, Arup, 12 2015.

[3] Arup. *Laboratory Component Testing: Modelling Post-Test Predictions and Analysis Cross Validation.* Arup, 2016.

[4] ASCE. *ASCE 41-13: Seismic evaluation and retrofit of existing buildings.* ASCE, Reston, Virginia, 2013.

[5] N. Augenti, F. Parisi, A. Prota, and G. Manfredi. In-plane lateral response of a full-scale masonry subassemblage with and without an inorganic matrix-grid strengthening system. *Journal of Composites for Construction*, pages 578–590, 2011.

[6] D. Bernal. Viscous damping in inelastic structural response. *ASCE Journal of Structural Engineering*, pages 1240–1254, 1994.

[7] E. Bojorquez, A. Teran-Gilmore, S.E. Ruiz, and A. Reyes-Salazar. Evaluation of structural reliability of steel frames: Interstory drift versus plastic hysteretic energy. *Earthquake Spectra. 2*, 27:3:661–682, 2011.

[8] J.J. Bommer, D. Dost, B. Edwards, A. Rodriguez-Marek, P.P. Kruiver, P. Meijers, M. Ntinalexis, and P.J. Stafford. Development of version 2 GMPEs for response spectral accelerations and significant durations from induced earthquakes in the groningen field. Technical report, NAM, 11 2015.

[9] S.J. Bourne, S.J. Oates, J. van Elk, and D. Doornhof. A seismological model for earthquakes induced by fluid extraction from a subsurface reservoir. *Journal of geophysical Research*, 2014.

[10] J.N. Breunese. *Induced seismicity of the Groningen gas field: History and recent developments.* Breunese, 2015.

[11] F. Cacovic and V. Turnsek. Some experimental results on the strength of brick masonry walls. 1970.

[12] S. Cattari and S. Lagomasino. A strength criterion for the flexural behaviour of spandrels in unreinforced masonry walls. *The 14th World Conference on Earthquake Engineering*, 2008.

[13] CEN. *Eurocode 6: Design of masonry structures—Part 1-1: General rules for buildings—Rules for reinforced and unreinforced masonry.* CEN, Brussels, Belgium, 2009.

[14] CEN. *NPR 9096-1-1.* CEN, Brussels, Belgium, 2012.

[15] CEN. *Eurocode 8: Design of structures for earthquake resistance—Part 1-1: General rules, seismic actions and rules for buildings.* CEN, Brussels, Belgium, 2013.

[16] S.Y. Chen, F.L. Moon, and T. Yi. A macroelement for the nonlinear analysis of in-plane unreinforced masonry piers. *Engineering Structure*, 30:2242–2252, 2008.

[17] B.S.J. Chiou and R.R. Youngs. NGA model for average horizontal component of peak ground motion and response spectra. Technical report, PEER, 11 2008.

[18] C. Chisari, A.B. Francavilla, M. Latour, V. Piluso, G. Rizzano, and C. Amadio. Critical issues in parameter calibration of cyclic models for steel members. *Engineering Structures*, pages 132:123–138, 2017.

[19] A. K. Chopra. *Dynamics of Structures - Theory and Application to Earthquake Engineering.* University of California, Berkeley, USA, 1995.

[20] A.K. Chopra and F. McKenna. Modelling viscous damping in nonlinear response history analysis of buildings for earthquake excitation. *Earthquake Engineering Structural Dynamics*, pages 45:193–211, 2016.

[21] R.W Clough. and J. Penzien. *Dynamics of Structures.* McGraw-Hill, Singapore, 1993.

[22] H. Crowley, R. Pinho, B. Polidoro, and P. Stafford. Development of v2 partial collapse fragility and consequence functions for the groningen field. Technical report, NAM, 11 2015.

[23] A. Dazio and K. Beyer. Seismic behaviour of different types of masonry spandrels. *14th European Conference Earthquake Engineering*, 2010.

[24] TU Delft, EUCentre, and Arup. Eucentre shaketable test of terraced house modelling predictions and analysis cross validation. Technical report, NAM, 10 2015.

[25] B. Dost and D. Kraaijpoel. The august 16, 2012 earthquake near Huizinge (Groningen). Technical report, KNMI, 1 2013.

[26] A. Penna A. Galasco F. Graziotti, G.Mageneses. Modello numerico semplificato ad un grado di libertà per l'interpretazione del comportamento dinamico di strutture in muratura. 2013.

[27] P. Fajfar. N2 – a method for non-linear seismic analysis of regular buildings. *Ninth Word Conference on Earthquake Engineering*, 1998.

[28] FEMA. *FEMA 306: Evaluation of earthquake damaged concrete and masonry wall buildings.* FEMA, Washington DC, 1998.

[29] S. Giovinazzi, S. Lagomarsino, and S. Resemini. Damping factors and equivalend sdof definition in the displacement based assessment of monumental masonry structures. *First European Conference on Earthquake Engineering and Seismology*, 2006.

[30] D. Grant and M.J.N. Priestley. Viscous damping in seismic design and analysis. *Journal of Earthquake Engineering*, 2004.

[31] L.F. Ibarra and H. Krawinkler. Global collapse of frame structures under seismic excitations. Technical report, PEER, 9 2005.

[32] C.L. Knox. *"Assessment of Perforated Unreinforced Masonry Walls Responding In Plane."*. PhD thesis, The University of Auckland, New Zealand, 1 2012.

[33] S. Lagomarsino, Penna A, A. Galasco, and S. Cattari. Tremuri program: An equivalent frame model for the nonlinear seismic analysis of masonry buildings. 2013.

[34] G. Magenes and G.M. Calvi. Cyclic behaviour of brick masonry walls. 1992.

[35] G. Magenes and G.M. Calvi. In-plane seismic response of brick masonry walls. *Earthquake Engineering and Structural Dynamics*, pages 1091–1112, 1997.

[36] G. Magenes, M. Rota, and A. Penna. A methodology for deriving analytical fragility curves for masonry buildings based on stochastic nonlinear analyses. *Engineering structures*, pages 1312–1323, 2010.

[37] F. McKenna, G.L. Fenves, and M.H. Scott. Open system for earthquake engineering simulation. *Pacific Earthquake Engineering Research Center*, 2000.

[38] G.M. Calvi M.J.N. Priestley and M. J. Kowalsky. *Displacement-based Seismic Design of Structures.* IUSS Press, Pavia, 2007.

[39] F.L. Moon. *Seismic strengthening of low-rise unreinforced masonry buildings.* PhD thesis, Georgia Institute of Technology, Atlanta, 2004.

[40] F.L. Moon, T. Yi, R.T. Leon, and L.F. Kahn. Analyses of a two-story unreinforced masonry building. *Journal of Structural Engineering*, pages 653–662, 2006.

[41] A. G. Muntedam-Bos and J.A. de Waal. *Reassesment of probability of higher magnitude eaarthquakes in the Groningen gas field.* 2013.

[42] NAM. *Winningsplan Groningen Gasveld.* NAM, Groningen, The Netherlands, 2016.

[43] NAM. Rapportage seismiciteit groningen - 1 nov 2017. Technical report, NAM, 11 2017.

[44] O. Ozcelik, S. Misir, C. Amaddeo, U. Yucel, and E. Durmazgezer. Modal identification results of quasi-statically tested rc frames at difference damage levels. 2015.

[45] M.J.N. Priestley. Seismic behaviour of unreinforced masonry walls. *Bulletin of the New Zealand Society for Earthquake Engineering*, 1985.

[46] I.M. Qureshi and P. Warnitchai. Computer modeling of dynamic behavior of rocking wall structures including the impact-related effects. *Advances in Structural Engineering 19(8)*, pages 1245–1261, 2016.

[47] A. Rahman and T. Ueda. In-plane shear performance of masonry walls after strengthening by two different frps. *Journal of Composites for Construction*, 2016.

[48] G. Ravenshorst, R. Esposito, F. Messali, A. Tsouvalas, E. Lourens, and J. Rots. Structural behaviour of a calcium silicate brick masonry assemblage: quasi-static cyclic pushover and dynamic identification test. Technical report, TU Delft, 10 2016.

[49] P. Roca, C. Molinis, and A.R. Mari. Strength capacity of masonry wall structures by the equivalent frame method. *Struct Eng ASCE*, pages 1601–10, 2005.

[50] J. Rots. *Structural Masonry. An experimental/Numerical Basis for Practical Design Rules.* August Aimé Balkema, Rotterdam, 1997.

[51] R. Sabatino and G. Rizzano. An equivalent frame model for the seismic analysis of masonry structures. *8º Congresso de Sismologia e Engenharia Sismica*, 2010.

[52] M.H. Scott and G.L. Fenves. A krylov subspace accelerated newton algorithm. *ASCE Structures Congress, Seattle, WA*, 2003.

[53] TNO. *Toestsing van de bodemdalingsprognoses en seismiche hazard ten gevolde van gaswinning van het Groningen veld.* 2013.

[54] TNO. *Response of induced seismicity to production changes in the Groningen field.* 2015.

[55] M. Tomazevic. *Earthquake-resistant design of masonry buildings.* Imperial College Press, London, UK, 1999.

[56] G. Vasconcelos and P.B. Lourenço. In-plane experimental behavior of stone masonry walls under cyclic loading. *Journal of Structural Engineering*, 2009.

[57] Z. Xu, X. Lu, and K.H. Law. A computational framework for regional seismic simulation of buildings with multiple fidelity models. *Advances in Engineering Software*, 2016.

[58] O.C. Zienkiewicz and R.L. Taylor. *The Finite Element Method, volume 2.* McGraw-Hill Book Company, Berkshire, 1991.